Stacked Disks Resonators and Micromachined Microphones: Design and Modeling

Christopher Grinde

September 7. 2010

Series of dissertations submitted to the
Faculty of Mathematics and Natural Sciences, University of Oslo
No. 987

ISSN 1501-7710

Cover: Inger Sandved Anfinsen.
Printed in Norway: AiT e-dit AS.

Produced in co-operation with Unipub.
The thesis is produced by Unipub merely in connection with the
thesis defence. Kindly direct all inquiries regarding the thesis to the copyright
holder or the unit which grants the doctorate.

Abstract

In this thesis, the design and modeling of two micromachined systems are presented. The two devices are a novel stacked disks resonator designed for radio frequency systems and a set of microphones with released membrane designs for photoacoustic gas sensing for CO_2 monitoring in demand controlled ventilation systems.

For the novel stacked disk resonator design, an analytical model for the frequency separation is derived and verified using finite element analysis. The model provides useful insight into the coupling mechanisms of two or more vertically stacked disks connected via a central stem. One unsuccessful and one incomplete fabrication trial is presented and analyzed. In addition, an analytical model for support losses adapted from a simple model for soil-structure interaction is investigated and found useful for estimating the support losses. The novelty of stacked disk resonator is vertical integration of devices previously only demonstrated integrated in-plane. Vertical integration allows smaller footprint. Although fabrication has yet proved unsuccessful, useful models have been developed and insight into the coupling mechanisms gained.

Two different designs of the miniaturized microphones have been designed, fabricated and characterized. Both designs feature released membranes, but of different thickness. They are designed for high sensitivity at low frequencies. Compared to a similar microphone published in the literature, the microphones presented here feature a doubling and thirty fold improvement in sensitivity for the frequency range of interest for the two designs.

Acknowledgments

I would like to express my gratitude to professors Tor A. Fjeldly at and Henrik Jakobsen for the opportunity, support and guidance throughout the duration of this scholarship. Without their help and support, this thesis would never have been. I am truly grateful to the contributions of Per Øhlckers, who with no formal affiliation to me as a student, has provided great advice, input, motivation and feedback. A special thanks to my colleagues Nils Høivik and Xuyuan Chen, who, along with Per Øhlckers, who have been interesting discussion partners through many hours of driving along those 100 km from Asker to Borre. Many of the researchers and staff at SINTEF MiNaLab have contributed to the work presented in this thesis. They are too many to be mentioned, but a particular acknowledgment is done to Jon Due Hansen who made a great effort in the fabrication trials of the stacked disk resonators. Last, but not least, I am in greatly thankful for the patience and support of my family, Beate, Henrik and Guro.

All fabrication done at SINTEF MiNaLab has been financed by The Research Council of Norway through project no 181712/I30:'Microtechnological research platform'. I also thank SensoNor for sponsoring access to their MPW service, MultiMEMS.

Contents

List of Tables

List of Figures

Nomenclature

$\bar{v}_{rr}$	radial coupling velocity averaged over stem radius
$\bar{v}_{zz}$	Disk thickness contraction rate at surface averaged over stem radius
$\Delta r_{bs}(z)$	bottom stem radial displacement profile
Δp	pressure difference over microphone membrane
$\Delta r_s(z)$	radial stem displacement profile
η	Fitting coefficient for stem deformation profiles
κ	Numerical frequency scalar
$[-]$	Unitless value
ν	Poisson's ratio
ω	radian frequency
ω_d	disk frequency
ω_{asym}	resonant frequency of dumbbell system with bottom stem and top-hat, anti-phase mode
ω_{dasym}	dumbell anti-phase resonant frequency
ω_{dsym}	dumbell in-phase resonant frequency
ω_{sym}	resonant frequency of dumbell system with bottom stem and top-hat, in-phase mode
ρ	material density
ρ_d	material density of disk
ε_0	Permittivity of vacuum
ε_r	Relative permittivity
ε_{zz}	disk thickness strain
${}_1F_2$	Hypergeometric function. Defined in (2.22)

A_d	disk perimeter complex amplitude
C_{eq}	equivalent beam compliance
E_y	Young's modulus
F_{rr}	force acting radially on disk perimeter
F_{zz}	reaction force acting on disk surface
H_0	Struve function of zeroth order
H_1	Struve function of first order
h_{bs}	height of bottom stem
h_s	height of inter-disk stem
h_{ts}	height of top hat stem stub
$I(x)$	second area moment of inertia
J_0	Bessel function of first kind, zeroth order
J_1	Bessel function of first kind, first order
k_{bsrr}	bottom stem equivalent stiffness for radial deformation
k_{bszz}	bottom stem equivalent stiffness for longitudinal loads
k_{diskrr}	equivalent stiffness for radial deformation at the perimeter of the disk
k_{drr}	disk equivalent stiffness at stem interface for radial deformation
k_{dzz}	disk equivalent stiffness at stem sinterface for deformation over half the disk thickness
k_{eq}	equivalent stiffness
k_{srr}	equivalent stiffness radial stem displacement at disk interface
k_{szz}	equivalent stiffness for stem subject to longitudinal deformation
KE	Kinetic energy
KE_{bs}	bottom stem kinetic energy
KE_{disk}	disk kinetic energy
KE_{stem}	stem kinitic energy
L_b	beam length
m_{bsrr}	bottom stem equivalent mass for radial deformation

m_{bszz}	bottom stem equivalent mass for longitudinal loads
m_{diskrr}	equivalent mass for radial deformation at the perimeter of the disk
m_{drr}	disk equivalent mass at stem interface for radial deformation
m_{dzz}	disk equivalent mass at stem interface
m_{eq}	equivalent mass
m_{srr}	equivalent mass radial stem displacement at disk interface
m_{szz}	equivalent mass for stem subject to longitudinal deformation
Q	quality factor
r	radial coordinate
R_d	disk radius
r_s	stem radius
r_{bs}	radius of bottom stem
t_b	beam thickness
t_d	disk thickness
$U(r)$	Radial displacement at r
u_{diskrr}	radial displacement at the perimeter
u_{rr}	instantaneous radial displacement at the disk perimeter
u_{zz}	disk deformation at disk surface relative to center of disk
$u_{zz}(r, z)$	thickness displacement at coordinate (r, z) relative to disk center
$v_{zz}(r, z)$	Disk thickness contraction rate at coordinate (r, z) relative to disk center
w_b	beam width
Pa	Pacal. Unit of pressure [N/m^2]

Acronyms and abbreviations

ADC Analogue to Digital converter 18
AR Aspect Ratio 39
ALD Atomic Layer Deposition 9
ALCVD Atomic Layer Chemical Vapor Deposition 9
BAR Bulk Acoustic Resonator 18
BMM Bulk MicroMachining 6
BOX Buried OXide layer 47
BSAC Berkeley Sensor and Actuator Center 47
BEM Boundary Element Method 54
CAD Computer Assisted Design 85
CAS Computer Algebra System 65
CMOS Complementary Metal Oxide Semiconductor 2
CVD Chemical Vapor Deposition 8
CBE Chemical Beam Epitaxy 9
DAC Digital to Analogue Converter 18
DAQ Data AcQuisition 82
DCV Demand Controlled Ventilation 3
DOF Degrees Of Freedom 10
DRIE Deep Reactive Ion Etching 8
DSOI Double layered Silicon On Insulator 44
DSP Digital Signal Processor 18
EPI EPItaxial 78
ECES Electro Chemical Etch Stop 7
EBR Edge Bead Removal 48
FEA Finite Element Analysis 2
HF HydroFluoric acid 7
HVAC Heating, Ventilation and Air Conditioning 3
LNA Low Noise Amplifier 18
LBR Longitudinal Bulk Resonator 19
LPCVD Low pressure Plasma assisted Chemical Vapor Deposition 46
MST Micro System Technologies 1
MEMS Micro Electro Mechanical Systems 1
MPW Multi Project Wafer 3

MOCVD Metal-Organic Chemical Vapor Deposition 8

NDIR Non-Dispersive InfraRed 71

nm nano meter 1

RF Radio Frequency 17

RIE Reactive Ion Etching 8

PA Power Amplifier 18

PAS Photo Acoustic Sensor 3

PML Perfectly Matched Layer 12

PCVD Plasma assisted Chemical Vapor Deposition 6

pSi poly-Silicon 9

PVD Physical Vapor Deposition 9

IC Integrated Circuit 1

IR Infra Red 72

ppm parts per million 92

KOH Potassium Hydroxide 7

Q-factor Quality factor 18

LIGA X-ray LIthography, Electroforming (German: Galvanoformung), and molding (German: Abformung) 6

LPCVD Low pressure Plasma assisted Chemical Vapor Deposition 46

SCS Single Crystal Silicon 6

SEM Scanning Electron Microscope 8

SMM Surface MicroMachining 6

SMD Spring-Mass-Dashpot 24

SOI Silicon On Insulator 49

SNR Signal to Noise Ratio 73

SINAD SIgnal to Noise And Distortion 82

SPICE Simulation Program with Integrated Circuit Emphasis

TMAH Tetra Methyl Ammonium Hydroxide 7

TPS Tire Pressure Sensor 74

UV Ultra-Violet

VCO Voltage Controlled Oscillator 17

Preface

The thesis is submitted in fulfillment of the requirements for the degree Philosophiae Doctor at the University of Oslo, Faculty of Mathematics and Natural Sciences, Department of Informatics. The work has mainly been carried out at Vestfold University College and UniK - University Graduate Center at Kjeller. Some of the work presented has also been carried out at University of California at Berkeley, Berkeley Sensors and Actuators Center.

Chapter 1

Introduction and background material

Microtechnology, which is the technology of microfabrication, can be said to start with the invention of the transistor by Bardeen, Shockley and Brattain in 1947. Soon, multiple transistors were integrated into the same slab of silicon, making the first Integrated Circuit (IC), an idea conceived by Jack. S. Kilby, patented in 1959 and awarded him the Nobel prize in physics in 2000[1]. IC technology has since then been developing at a pace commonly referred to as Moore's law: A doubling of processing capability every 18 months. Processors and memory modules for consumer products such as computers and mobile phones are currently fabricated with transistors gate lengths of less than 50 nano meter (nm) and expected to be 22 nm by 2011[8].

One of the fabrication techniques most critical for the success of the IC, is that of batch fabrication. Batch fabrication allows the fabrication of multiple devices in parallel and makes it possible to fabricate ICs for a few Euros each. Another key technology developed, is photolithography. It allows patterns with sub-micron features to be defined using a light sensitive emulsion called photoresist. The emulsion is first deployed in a thin layer over the substrate, before it is baked and exposed using a mask with defined transparent and opaque areas. Depending on the polarity of the photoresist, these patterns are either reproduced or inverted when the photoresist is developed after exposure. Hence the photoresist provides means of selective manipulation of the surface or near-surface regions of the substrate.

As a spin-off of the IC technology, adopting and adapting its techniques, micromachined electromechanical structures were starting to be explored at the beginning of the 1960's. Devices such as pressure sensors [9], the resonant gate transistor in 1967 [10] and accelerometers [11] were developed using the same fabrication techniques as for ICs. Combining moving compliant structures with electrical circuits in a single slab of material, this technology has later been termed Micro Electro Mechanical Systems (MEMS) in the US and Micro System Technologies (MST) in Europe.

While early devices typically were miniaturized versions of macroscopic systems, the reduction in size also enabled new and novel devices to be made. In this process, some effects that

[1] Robert Noyce is commonly also credited the invention of the IC, but died in 1990. Nobel prices are not given post-mortem.

were important in macroscopic systems became negligible while others that were previously negligible became significant. A typical example of this, is the development of numerous microfluidic devices [12, 13], where volume forces diminish and surface forces becomes important as dimensions are scaled down. The reduction in size also allows the utilization of electrokinetic phenomena using lower voltages, which simplifies interface circuitry. This allows e.g. manipulation of small volumes through the use of passive valves, increased mobility of charged particles or fast and accurate temperature cycling, all contained within one small system [13].

For more than three decades now, micromachined systems have been available commercially [14] and it has come to the point where they are no longer exclusive to high-end and high-cost applications, but common in consumer products such as mobile phones, compact music players, digital cameras, laptops and other low cost products. They provide new features or reduced fabrication cost for high volume products, increased reliability and reduced power consumption compared to the systems they replace.

Although dimensions in current microsystems typically are one order of magnitude greater than the current IC technology, there are many technical challenges with fabricating MEMS devices. Often, their mechanical nature results in increased topographical complexity on the wafer, complicating photolithographic processing with respect to both resist coverage and depth of focus issues. Sensors that need to interact with the surroundings, require packages with physical interfaces, e.g. microphones and humidity sensors, while other, e.g. inertia sensors, require hermetic packaging to maintain performance over time.

While many of the fabrication technologies used for MEMS are adopted from the IC industry, many have been developed solely for micromachining. Although well established, they are rather young. This means that stress management, material selectivity, process stability and many other challenges often must be addressed for even the simplest devices. In addition, it is highly desirable to establish these processes at low temperatures in order to enable direct integration with Complementary Metal Oxide Semiconductors (CMOSs) circuits, simplifying system level integration.

1.1 Outline of thesis

The work presented in this thesis address two of the challenges of MEMS: Integration with ICs and reducing cost and complexity of well established technologies, enabling new applications. The text is divided into two parts, each part representing independent pieces of work within the same field.

In Part I, a coupled mechanical resonator structure with potential for direct integration in ICs and reduced footprint is explored. Expressions useful for designing filters and multi-resonator systems from coupled stacked disk resonators, are derived and compared to results from Finite Element Analysis (FEA). Two process sequences are suggested and the corresponding fabrication attempts are reported. Although the process sequences explored were unsuccessful and

incomplete, respectively, a new design avoiding many of the problems experienced is suggested based upon what has been learned. The main achievement of this part is the model developed and the insight gained on coupling mechanisms of vertically stacked disk resonators.

In chapter 3, a simple model for estimating the important support losses in single disk resonators, is evaluated. The model is found to give reasonable accuracy and provides a simplification compared to similar models from the literature.

In Part II, two microphones for low cost Photo Acoustic Sensor (PAS) systems for Demand Controlled Ventilation (DCV) in Heating, Ventilation and Air Conditioning (HVAC) systems are developed and characterized. The microphones are fabricated using a low cost Multi Project Wafer (MPW) service. A thirty-fold improvement in sensitivity and resolution was achieved for one of the designs compared to a similar application specific microphone fabricated in the same MPW service. The main achievement of this part is the confirmation that the suggested designs provides means of making low cost, high-sensitivity microphones with sufficient resolution for DCV systems.

Both parts are extensions of papers recently accepted or submitted to leading journals in the field of microsystem technology, and roughly follow their form with introduction, methods, results, discussion and conclusion. The work presented in chapter 3 is yet unpublished. Some work presented on equivalent circuit models included in Part I is also unpublished.

1.2 Publications and contributions

Tables 1.1 and 1.2 list publications I have either written or contributed to. The publications listed in Table 1.1, are those relevant to the work presented in this thesis.
In [15] and [16] the design, modeling and characterization of the microphones presented in Part II is presented. Both articles contain errors with respect to the model used and the interpretation of the data collected. Their content has been corrected, extended and published in [17].
Articles [18] and [19], present the initial work done on the stacked disk resonators presented in Part I. [20] contains extended models from [19], and forms the main basis of this part.

For the publications listed in Table 1.2, my contributions have been FEA and design in [21, 22] and general design and modeling in [23, 24, 25, 4, 26]. Figure 1.1 shows a top view micrograph and a photograph of the accelerometer whose design and modeling was presented in [4, 26]. In [27, 28], which are articles on training efforts in an integrated project funded by the European Commission, I performed the majority of training and reporting on these activities, while [29] is an extension of work I did under Eskild Westby and Tor Fjeldly as a Cand. Scient student.

Table 1.1: List of publications 2003-2010 on microphones and double disk resonators.

Reference	
[18]	K. H. Nygaard, C. Grinde, and T. A. Fjeldly, "Stacked Coupled-Disk MEMS Resonators for RF Applications," in *Technical Proceedings of the 2008 NSTI Nanotechnology Conference and Trade Show*, vol. 3, pp. 478 – 480, 2008
[15]	C. Grinde, P. Ohlckers, M. Mielnik, G. U. Jensen, A. Ferber, and D. Wang, "A clover shaped silicon piezoresistive microphone for miniaturized photoacoustic gas sensors," in *Prodeedings from DTIP 2009*, pp. 256–260, EDA Publishing, 2009. ISBN:978-2-35500-009-6
[19]	C. Grinde, K. Nygaard, J. Due-Hansen, and T. A. Fjeldly, "Lumped modeling of a novel RF MEMS double-disk resonator system," in *Proceedings of DTIP 2009*, pp. 14–18, EDA Publishing, 2009. ISBN: 978-2-3550-0009-6
[16]	A. Sanginario, C. Grinde, and P. Ohlckers, "Characterization of two novel low frequency microphones for photoacustic gas sensors," in *Proceedings of Eurosensors XIII, 2009*, 2009
[17]	C. Grinde, A. Sanginario, P. A. Ohlckers, G. U. Jensen, and M. M. Mielnik, "Two clover-shaped piezoresistive silicon microphones for photoacoustic gas sensors," *Journal of Micromechanics and Microengineering*, vol. 20, no. 4, 2010
[20]	C. Grinde and T. Fjeldly, "Frequency separation in vertically stacked disk resonators," *Springer Microsystem Technolgy*, 2010. Submitted for review to Springer Microsystem Technology

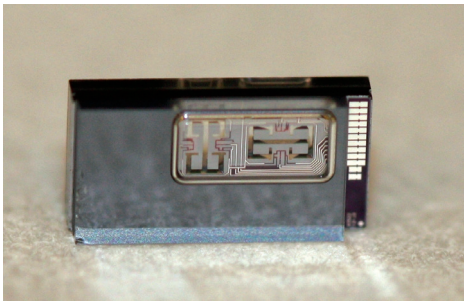

(a) Photograph of the 3×6 mm^2 die.

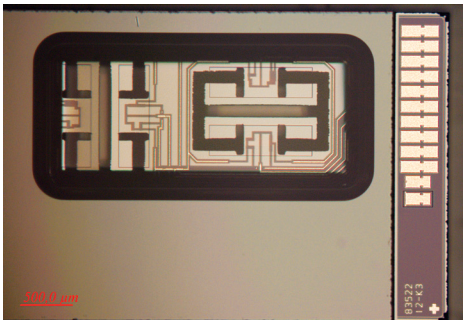

(b) Top view micrograph showing the internal structure of the triaxial piezoresistive accelerometer. Required area for sensor area is $2\times$ 4mm^2

Figure 1.1: The accelerometer whose design and modeling is presented [4]

Table 1.2: Other papers published 2003-2010

Reference	
[29]	C. Grinde and E. Westby, "A method for adding static external forcing to invariant manifolds," in *Technical Proceedings of the 2008 NSTI Nanotechnology Conference and Trade Show*, vol. 3, pp. 636 – 639, 2005
[23]	C. Lowrie, C. Grinde, M. Desmulliez, and L. Hoff, "Piezoresistive three-axis accelerometer for monitoring heart wall motions," *Proceedings of DTIP, 2005*, pp. 131–136, 2005. ISBN:2-84813-0357-1
[24]	C. Lowrie, C. Grinde, L. Hoff, M. Desmulliez, O. J. Elle, and E. Fosse, "Design of a three-axis accelerometer for heart motion studies," in *Proc. Of IMAPS Nordic Conference 2005*, 2005
[25]	C. Lowrie, C. Grinde, L. Hoff, M. Desmulliez, and O. J. Elle, "Design of a miniature three-axis accelerometer for the study of heart wall motion," in *Proceedings of Micro Structure Workshop, Vesterås, Sweden, 2006.*, 2006
[27]	C. Grinde, D. Dermarchi, P. Ohlckers, P. Civera, and S. Hansen, "An approach to seminar based MEMS training," in *Proceedings of EWME2008 - European Workshop on Microelectronics Education (Budapest) May 28-30*, EDA publishing, 2008. ISBN: 978-2-35500-007-2
[21]	C. Ferreira, P. Ventura, C. Grinde, R. Morais, A. Valente, C. Neves, and M. Reis, "A novel monolithic silicon sensor for measuring acceleration, pressure and temperature on a shock absorber," in *Proceedings of Eurosensors XIII, 2009*, pp. 88–91, 2009
[22]	C. Ferreira, P. Ventura, C. Grinde, R. Morais, A. Valente, C. Neves, and M. Reis, "A self-powered embedded system for shock absorber diagnosis during vehicle motion," in *Proceedings of FISITA 2010*, 2010
[4]	C. Grinde, C. Lowrie, and P. Ohlckers, "Fabrication of a MEMS triaxial accelerometer using novel post-processing of an MPW process," in *Proceedings of MME 2009*, vol. 1, p. 1, 2009
[28]	C. Grinde, D. Demarchi, P. Civera, and P. Ohlckers, "An approach to short-courses in a pan-European training program in microsystem technologies," *European Journal of Engineering Education*, 2010. Submitted for review to European Journal Of Engineering Education
[26]	P. Ohlckers, L. Petricca, and C. Grinde, "A three axis accelerometer," in *Proceedings of Micromechanics Europe 2010*, 2010. Accepted for pubclication at MME 2010
[30]	C. Ferreira, P. Ventura, C. Grinde, R. Morais, A. Valente, C. Nevesa, and M. Reis, "Characterization and testing of a shock absorber embedded sensor," in *Proceedings of Eurosensors 2010*, 2010. Accepted for publication at Eurosensors 2010

1.3 Micromachining techniques

Micromachining is as the name implies the craft of fabricating structures on the micrometer scale. Although high precision milling machines capable of machining structures down to a few microns in width does exist, the term is more commonly used for the structuring of planar surfaces through the selective addition and removal of materials. Traditionally, the field of micromachined devices has been divided into three main methods: Bulk MicroMachining (BMM), Surface MicroMachining (SMM) and X-ray LIthography, Electroforming (German: Galvanoformung), and molding (German: Abformung) (LIGA). However, as the range of micromachining techniques constantly increases with methods such as hot embossing and laser milling [31], the distinction becomes increasingly less clear. It is therefore more relevant to sort the techniques into additive and subtractive processes. This leaves some techniques left outside, e.g. hot embossing, but as none of these methods are of interest to the work presented in this thesis, the reader is referred to textbooks on micromachining such as [32] for more information.

Below, brief introductions to key techniques relevant for the work presented in both part I and II, are presented.

1.3.1 Substrates and materials

For several reasons MEMS has traditionally been based on Single Crystal Silicon (SCS) substrates in the form of circular wafers of less than 1 mm thickness. SCS was the material used by the IC industry. Hence, it was thoroughly characterized, its fabrication processes were highly tuned and numerous methods for manipulation and machining already existed when MEMS was starting to be explored. Another reason was that SCS has excellent mechanical properties [14], in particular the linearity with respect to strain. This property can be assigned to its single crystalline structure. On the other hand, the material is brittle and quite anisotropic in terms of the Young's modulus and the Poisson's ratio [1]. When certain micromachining techniques are used e.g. wet etching with alkali solutions, the crystal anisotropy gives rise to structures whose boundaries are governed by the crystal planes of the SCS.

Silicon can also be used in the polycrystalline form, both as thin films and substrates. This is the form of silicon that the majority of SMM devices are made from. The main difference to SCS with respect to material properties, is that the material can be considered to be isotropic on the device scale owing the the small size of the grains of SCS, typically in the range 60 to 140 nm [33]

Other materials commonly used are oxides, in particular silicon dioxide (SiO_2), which is a good dielectric material that can be thermally grown from silicon or deposited with Plasma assisted Chemical Vapor Deposition (PCVD). SiO_2 is commonly used as sacrificial material in SMM as chemicals and processes with high selectivity for SiO_2 over other common materials, is available. Another dielectric material commonly used, is silicon nitride (Si_3N_4). It is often used as a dielectric material or termination layer for etches. Common metals are aluminum, gold, and copper, which are mainly used for leads and bond pads.

A full list of relevant materials would be beyond the scope of this text. Readers are referred to textbooks on microfabrication such as [34, 32]

1.3.2 Photolithography

To enable fabrication of miniaturized structures with minimum dimensions in tenths of micrometers, layers of materials are added or removed from the substrates using techniques such as evaporation and etching. These techniques alone provide no means of geometric selectivity, and thereby no means of making multidimensional structures. Although methods such as shadow masking exist, by far the most common method for providing geometric selectivity is photolithography. Photolithography makes use of thin films of radiation sensitive polymers, referred to as photoresists. After exposure to radiation (e.g. UV-light or x-rays), they become either solvable or insolvable in certain chemicals. By masking the radiation with masks with opaque patterns, it is possible to reproduce or invert these patterns on the underlying substrate. The remaining photresist can then be used as masking material for whatever treatment the substrate is subjected to, providing means of selective micromachining.

No extensive introduction to photolithography will be included here, but can be found in textbooks such as [34, 32].

1.3.3 Subtractive techniques

In order to form in-plane geometries various forms of subtractive techniques exist. They are commonly divided into dry and wet etching processes. In addition, micro-cutting techniques [35], electro discharge micromachining [36, 37, 38, 39, 40] and other techniques are described in the literature. A full review is beyond the scope of this text, and only a general introduction of silicon micromachining techniques is included.

Wet etching

Both alkali and acid solutions are used for micromachining. In general, acids are used for isotropic etching, and are mainly used for glass, oxides, metals and thin films where the underetch is noncritical. Common acids used for micromachining are HydroFluoric acid (HF), sulfuric acid and acetic acid.

Alkaline solutions are most often used for anisotropic etching of single crystalline materials [41], e.g. SCS. Typical alkali solutions used are Potassium Hydroxide (KOH) and Tetra Methyl Ammonium Hydroxide (TMAH) [42]. The surfaces of the resulting structures are governed by the crystal planes of the substrate.

Wet etching has been used in both Part I and Part II to etch openings in oxide masks, pattern aluminum and specifically for fabricating membranes of high precision thickness using Electro Chemical Etch Stop (ECES) in Part II. ECES is a method for electrochemical passivation of silicon. During etching, the silicon is biased such that pn-junctions within the silicon are reverse

biased. Since alkali etching of silicon in itself is an electrochemical reaction in which electrons play a vital role, it can be passivated by applying an anodic potential relative to the etchant, controlling the recombination of the electrons and hence the resulting reactions [43]. The setup is described in [44] and a model explaining the reactions of the passivation can be found in [45].

Dry etching

Dry etching can be divided into two classes of methods: plasma based and non-plasma based [46].

In plasma based methods, ions are generated from gas in a high-frequency electric field or by inductive coupling. The ions diffuse towards the surface to be etched and react chemically with the surface atoms and form volatile species that are removed from the etch chamber. The result is an isotropic etch profile. By adding an additional electric field over the plasma, the ions can be directed towards the target and enhanced directional etching can be achieved. This technique is referred to as Reactive Ion Etching (RIE). For certain gases, the generated ions are chemically inert with respect to the target material and the removal of material is purely kinetic. This technique is called ion milling.

Among the plasma based techniques, an extended version of RIE, Deep Reactive Ion Etching (DRIE) is currently the method of choice for fabricating high aspect ratio structures. A sequence of directional etches and deposition of inert polymers are used to achieve narrow trenches with aspect ratios larger than 30:1 [47]. Figure 1.2 shows the Scanning Electron Microscope (SEM) micrograph of a cross section of a trench etched using DRIE. The sample shown, is a test wafer used for the development of the etching of the microphones presented in subsection 4.4.2. In the micrograph, one can see the scallops stemming from the sequential etching. A full introduction of the processes of DRIE can be found in textbooks such as [34]. An extensive review of state of the art and next generation processes can be found in [48].

Non-plasma based methods means that the etching is done by a vapor phase etchant. One common vapor phase process is using HF vapor to etch SiO_2. It is commonly used for etching sacrificial layers in SMM [49, 50] to avoid stiction, a problem caused by the surface tension of residual etchant or water if wet etching is used. In the work presented in Part I, it has been used to remove oxide in the narrow center holes of the stacked disks. The reader is referred to textbooks on semiconductor processing and microfabrication such as [34, 32] for further reading.

1.3.4 Additive techniques

A wide range of techniques for adding materials to substrates exists. In the work presented here, PCVD is of particular interest. Chemical Vapor Deposition (CVD) is the formation of thin solid films from a chemical reaction of vapor-phase precursors. There are many variations of CVD [51]: Thermal CVD, photo-assisted CVD, Metal-Organic Chemical Vapor Deposition

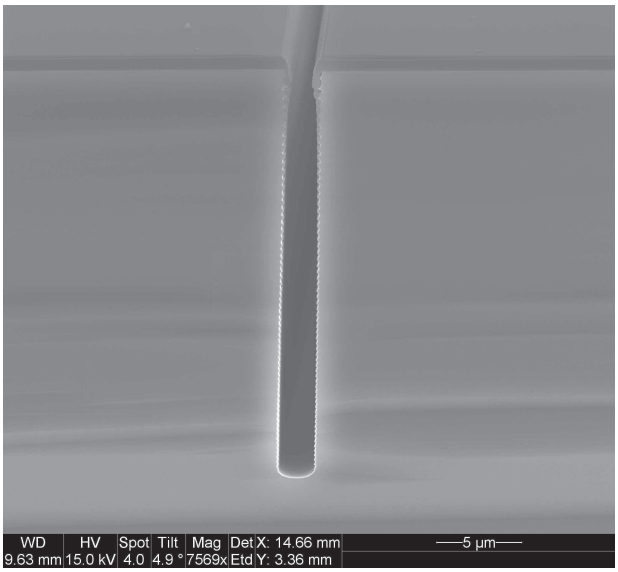

Figure 1.2: SEM micrograph of a trench etched using DRIE with photoresist as masking material. The shown sample is a test wafer used for the microphones presented in subsection 4.4.2. Image courtesy of Geir Uri Jensen, SINTEF ICT, MiNaLab.

(MOCVD), Atomic Layer Deposition (ALD), Atomic Layer Chemical Vapor Deposition (ALCVD), Chemical Beam Epitaxy (CBE) and numerous other variations. Their common denominator is the chemical reaction in the vapor, which forms solids on the substrate surface and/or in the vapor itself, which then deposit on the surface. In the work presented here, PCVD is used for forming the structural poly-Silicon (pSi) layers in the double disk resonator system in Part I. Other classes of additive methods are Physical Vapor Deposition (PVD), sputtering and evaporation. These methods are typically used for depositing metals on substrates. In the work presented here, sputtering has been used to deposit aluminum for metal leads in both projects. The reader is referred to textbooks on semiconductor processing and micromachining such as [34, 32] for further reading.

1.4 Modeling techniques

Since the initial costs of fabrication of microsystems are high, a great effort should be made on modeling to avoid costly design iterations. Since many microsystems are of great complexity with compliant mechanisms and multi-physical behavior, understanding their behavior and parameter dependencies is not necessarily straight forward. Further, to understand how the device interacts with its control electronics require system level modeling. This highlight the need to model microsystems on not only the device level, but also on the system level in order to fully understand what governs the performance of the microsystem.

Modeling at the device level takes the physical behavior of the device itself into account and typically also its interaction with the surroundings. This level of modeling typically involves multidomain simulations, and for sensors and actuators, also the transduction to and from the electrical domain. Once a model for the device has been established, a system level model is useful for investigating and optimizing the complete sensor including the interface electronics.

Several useful modeling techniques are commonly used for microsystems. In the work presented here, two complementary methods in particular, have been used for device level modeling: Lumped element modeling and FEA. While lumped modeling can be done using analytical expressions and numerical solvers, FEA is a purely numerical method. The benefit of analytical models is that the lumped element expression highlight geometric and material dependencies and hence provide simple design guidance. While simple systems can be modeled analytically, numerical solution schemes must be used to find solutions in an efficient manner if the level of complexity is high. While lumped element modeling of complete systems has obvious limitations with respect to accuracy, FEA is in principle only limited by the computational power available and the accuracy of the parameters and boundary conditions used.

In both Part I and Part II, lumped modeling has been used to increase the understanding of the devices investigated by providing simple expressions for the main behavior of the device. While very useful for simple systems, the complexity of large systems with many Degrees Of Freedom (DOF), e.g. as presented in Part I, complicates the development of simple and useful expressions. For such cases, FEA provides means of verification and an increased level of detail. However, FEA in itself requires a good understanding of the physical domains to be modeled, in order to be trusted for verification purposes. Therefore the two methods are complementary and acceptable verification can be achieved when the results from the two modeling methods are in agreement.

1.4.1 Lumped modeling

The term lumped modeling refers to a modeling technique where the physical objects, such as conductors, beams, thermal conductors, are small relative to the variation over the object. This enables the use of a lumped element that describes the distributed property of the object, simplifying the modeling of the system they are a part of. For low-frequency circuits made from discrete components, this comes naturally as the main impedances of the circuit are inherently lumped. However, at high frequencies, the leads and interconnections take on a transmission line character where the effects of distributed, complex impedances must be accounted for. In this case, accurate lumped model representations become more complex. A similar problem arise in mechanical systems where, for example geometric and mechanical properties are distributed, but can easily be modeled with reasonable accuracy using lumped equivalent element when frequencies are low. The term 'low' is usually defined as when the wavelength of the propagating waves are several multiples of the dimension of the structure being analyzed.

Due to the fabrication processes used, micromachined mechanical systems are compliant more often than not. Hence the mass, stiffness and damping are distributed rather than discrete

parameters. However, equivalent to as for high frequency circuits, the behavior can be modeled by using lumped masses, stiffnesses and dampers which are calculated for points of interests such as clamping and linking regions. One example is that of a long slender beam. If a harmonic force is applied at a frequency well below the beam's resonance frequency, its response can be approximated by a one-dimensional the partial differential equation describing the continuum of the beam, and solved for the appropriate boundary conditions. The lumped parameters are then calculated from the force applied and the resulting deflection at the point of interest. A large number of lumped models for statically loaded beams and plates subject to various loads and boundary conditions are available in [52]. In order to solve dynamical problems, the lumped parameters can be inserted into the equations of motion as,

$$\mathbb{M}\ddot{x} + \mathbb{B}\dot{x} + \mathbb{K}x = \mathbb{F} \tag{1.1}$$

where $\mathbb{M}$, $\mathbb{B}$ and $\mathbb{K}$ are $n \times n$ matrices of lumped masses, damping coefficients and stiffnesses and $\mathbb{F}$ is a vector of forces applied to the various nodes of the assembly. The dot notation in $\dot{x}$ and $\ddot{x}$ refers to the first and second order time derivatives of the nodal DOF in the position vector x.

For certain problems, the lumped properties at a given location in the system are of particular interest. An example of this is the calculation of the equivalent mass and stiffness at any given point in a resonator in order to optimize the coupling effect to other structural members of the system. Such a technique is used in Part I to estimate the anchor losses and frequency separation of single- and dual disk resonators and is presented in generalized form below.

The first step to find a localized equivalent mass and stiffness is to calculate the kinetic energy of the structural member of interest. Assuming a homogeneous material of density $\rho(x, y, z) = \rho$, this is done by integrating the particle velocity $v(x, y, z)$ over the domain:

$$KE = \int \frac{1}{2}\rho v(x, y, z)^2 dV \tag{1.2}$$

The equivalent mass can then be found from equating the kinetic energy with the one dimensional expression for kinetic energy

$$\begin{aligned} KE &= \frac{1}{2} m_{eq} v(x, y, z)^2 \\ &\Downarrow \\ m_{eq} &= \frac{2KE}{v(x, y, z)^2} \end{aligned} \tag{1.3}$$

where m_{eq} is the equivalent mass at location (x, y, z). From the relationship between stiffness, mass and frequency, the equivalent stiffness k_{eq} can then be found from:

$$\begin{aligned} \omega &= \sqrt{\frac{k_{eq}}{m_{eq}}} \\ &\Downarrow \end{aligned}$$

$$k_{eq} = \omega^2 m_{eq} \tag{1.4}$$

Once the equivalent masses and stiffnesses for all structural members of the system have been found, the natural frequencies of the assembly can be found as [53, 54]

$$\omega = \sqrt{\frac{\sum_i k_i}{\sum_i m_i}} \tag{1.5}$$

where the sums run over the stiffnesses and masses active for the mode of interest.

1.4.2 Finite Element Analysis

Some continuum problems are too complex, too comprehensive, or simply impossible to solve analytically. While several numerical methods exist to solve more or less any kind of problem that can be formulated, one method, the FEA, dominates the field of continuum mechanics.

The principle is that approximate solutions of, for example, the strain distribution in a domain (volume, area or line) can be found by trial functions. The trial functions can be linear or polynomial, indicating the fitting function approximating the strain within the element.

Boundary conditions are assigned to the outer boundaries and by dividing the domain for which a solution is sought into multiple lines, areas or volumes depending on the dimensionality of the problem, approximate solutions for the corresponding continuum can be found. The set of elements is called a mesh.

To increase the accuracy of the approximate solution, there are two approaches which can be combined. The most common, referred to as the h-method or mesh refinement, is to decrease the size of the mesh element, effectively reducing the variation over the element and thereby increasing the accuracy. The other method, referred too as the p-method, is to increase the polynomial degree of the trial function, which increases the accuracy of the approximating function.

Because each element contains two or more nodes, which, depending on the dimensionality of the problem, represent 2, 4 or 6 DOFs each, the computational effort increase rapidly when the number of elements are increased. It is therefore common to include a convergence study prior to running time consuming simulations to find a point where no further p- or h-refinement gives significant changes in the result. For further reading on the principles and theory of FEA, see [55, 56].

Perfectly matched layers

In chapter 3 an evaluation of lumped modeling of support losses using a technique developed for machine-structure interaction analysis is presented. As a reference model, a FEA model using a Perfectly Matched Layer (PML) to mimic the infinite size of the substrate is used.

PML are regions of elements with non-reflecting boundaries facing the energy source that absorb all inbound energy. They were originally developed for simulating infinite boundaries in electromagnetic simulations [57]. The concept has later been extended to structural mechanics [58], but also other domains. Work on PMLs for simulating anchor losses in micromachined resonators can be found in [59].

FEA software packages used

Many software packages for FEA exist, both open source and commercial. In the work presented in this thesis, two different packages have been used: COMSOL and ANSYS. COMSOL has been used mainly due to the availability of a structural PML element in the software. Since the work presented in this thesis spans several years, multiple versions of each of the software packages have been used, ending with COMSOL 3.5a and ANSYS 11.

1.4.3 Other methods of interest

A range of other methods are commonly used when modeling microsystems. Some are mentioned with no further discussion in this thesis. A very brief description of the concepts of the methods mentioned is therefore included.

Reduced order modeling

For large and complex systems, the main behavior and properties can in certain cases be described through a subset of their DOFs, e.g. through eigenmode analysis of equation (1.1), disregarding all modes of lesser importance. A recent review on reduced order modeling for MEMS can be found in [60].

Equivalent circuit modeling

Equivalent circuit modeling makes use of the similarity in formulations in various physical domains with the equations governing current, voltages and energy in circuits. This similarity has been used for more than 70 years to model various electromechanical systems [61]. As circuit simulators such as SPICE [62] are highly optimized, casting a system into the form of an equivalent circuit, allows fast simulations of frequency response and transient analysis. Also, having developed an equivalent circuit for the sensor or actuator, system level simulations can easily be performed.

A large number of publications on equivalent circuit modeling of MEMS exist. [63, 64] describes equivalent circuits for electromechanical transducers commonly utilized in microsystems. In [65] equivalent circuits for inertia sensors are described. An RF-MEMS switch with capacitive actuation is described in [66] and a large number of articles on RF-MEMS filters [67, 68, 69, 2] have continued a tradition for modeling electromechanical filters using equivalent circuits [54]. In [70, 71], equivalent circuits are used for modeling the dynamic behavior of microphones.

Although the governing equations for mechanical and electrical systems are similar, two schemes for casting a mechanical system into an electrical one, exist. The two schemes are commonly termed *effort-to-voltage* and *flow-to-voltage* [72]. In the first scheme, compliances, dashpots and masses have their equivalent circuit elements in capacitances, resistors and masses, respectively, while in the latter, compliances, dashpots and masses become inductors, resistors and capacitances, respectively. The *effort-to-voltage* scheme is most common in the MEMS community, probably since the majority are electrical engineers who tend to relate interface forces to voltages. Its main problem is that the system's topology is not maintained through the transformation, which makes the transformation of large systems less intuitive and in some cases, very complicated.

The *flow-to-voltage* scheme offers the great benefit of maintaining topology through the transformation, simplifying the transformation of large and complex system. The cost is that the interface forces are modeled as currents, complicating system level simulations somewhat. An extensive review and discussion on the pros and cons of the two methods can be found in [73].

Part I

Stacked disk resonators:Design and modeling

Chapter 2

Frequency separation in double disk resonators

2.1 Motivation for stacked disk resonators

Modern microelectronics consist of much more than just CMOS transistors. For Radio Frequency (RF) circuits, the properties of silicon might not meet the requirements of high frequency and power applications, and materials such as gallium arsenide and silicon germanium are used instead for certain types of components. These materials and hence devices are much more expensive than those made from silicon and are typically off-chip devices which increase the cost even further. Significant effort on the integration of off-chip devices on the chip through wafer level bonding and other mounting techniques, has been done, but require large areas to be reserved on the IC. Direct integration of various RF components using CMOS compatible micromachining techniques have been explored for resonators [74, 75], switches [76] and tunable capacitors [77, 78]. Since the cost of an IC is closely related to its area, it is highly desirable for these devices to have as small a footprint as possible. The work presented in this part, addresses this problem by suggesting and exploring a device that potentially can reduce the footprint of coupled disk resonators by a factor of two or more and, which in principle, is possible to integrate directly on an IC.

In addition, an evaluation of a modeling approach for estimating stem losses in single disk resonators is included in chapter 3. This model can easily be implemented for most substrate load cases relevant for micromachined resonators, including those of the double stacked disk resonator presented.

2.2 Background

2.2.1 RF circuits and micromachined resonators

RF circuits are designed to process electromagnetic signals at frequencies in the RF range, typically 300 Hz to 3000 GHz [5]. Figure 2.1 shows a typical block diagram of a combined receiver and transmitter, also called a transceiver. Key components are: Voltage Controlled

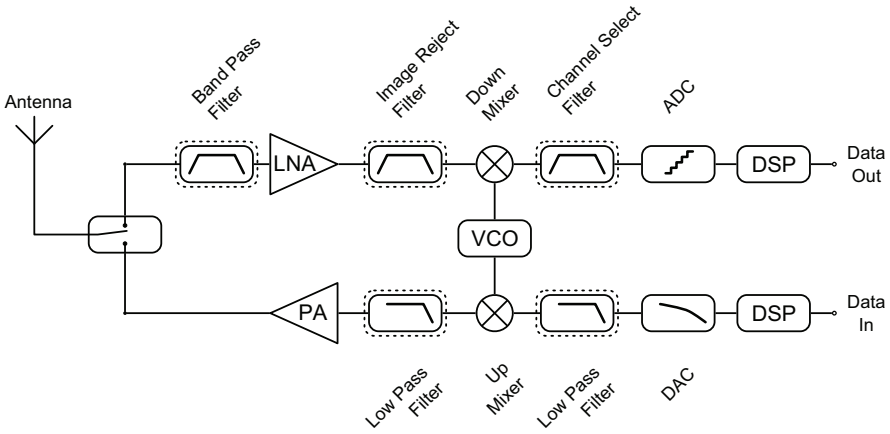

Figure 2.1: A block diagram of a generic RF transceiver. Recreated from [5].

Oscillator (VCO), Low Noise Amplifier (LNA), Power Amplifier (PA), Digital Signal Processor (DSP), Analogue to Digital converter (ADC), Digital to Analogue Converter (DAC) and various filters, marked with dashed rectangles in the figure. As can be seen, filters are vital parts of both the receiver and transmitter sections. As transmission frequencies increase, the challenge of making high performance filters in CMOS directly on the IC increases. Micromachined mechanical filters have a potential for not only high performance at high frequencies and are also in principle possible to integrate directly on the IC.

For the sake of completeness, it should be mentioned that there are a large number of other micromachined components for RF systems. Examples are varactors [77, 79] and switches [80]. An overview on design, modeling and fabrication of these and other devices can be found in [81].

Mechanical filters can be made by coupling two or more resonators. This has been done since after the Second World War [54] with macroscopic metal resonators. These filters were commonly used by the telecommunications industry until they were outperformed by solid state electronics. In the beginning of the 90's the first micromachined resonating structures for RF applications started to surface in the literature [82]. These first generation devices were SMM devices with two comb finger structures actuated electrostatically to vibrate parallel to the wafer surface as illustrated in Figure 2.2(a). The resonators were coupled via soft springs and operated between 5 kHz and 1 MHz. The sample device presented in [82] operated at 18.7 kHz and had a bandwidth of 1.2 kHz. One of the problems with these resonators, was that because of large areas moving normal to each other in near proximity, the Quality factor (Q-factor) of the device was governed by squeeze- and slide film effects, unless low pressure packaging was provided. Because of the bending motion, also thermoelastic damping affected the Q-factor significantly and finally, the frequency range of these devices, was limited to about 100 MHz without resorting to sub-micron lithographic techniques [83].
Addressing these issues, a range of Bulk Acoustic Resonators (BARs) have been explored [84,

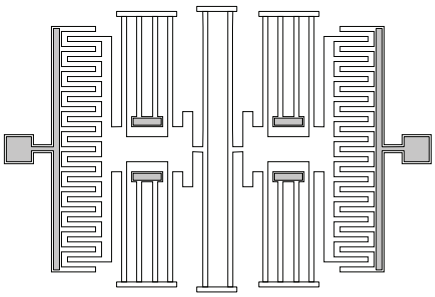

(a) Top view of a shuttle style resonator as implemented in [82].Gray areas are areas anchored to the substrate. The rest is free to move. The signal is input to the left. The comb drive forces the resonator through electrostatic forcing. In the center, a soft coupling spring connects the two resonators and transferring energy. At the right end, the signal exits the filter through the combdrive.

(b) Perspective view of a filter from two vertical bending mode resonators coupled via a small bar. Electrodes underneath each double clamped bar function as input and output electrodes for the electrostatic actuation. Example structure from [67]

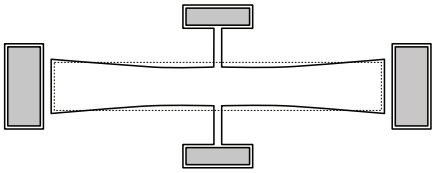

(c) BAR in the shape of a single slant beam.

Figure 2.2: Brief overview of various kinds of micromachined resonators

85, 86, 87, 88, 89]. Because the resonant modes are of extensional rather than of bending nature, the devices can contain much more energy per volume unit, meaning they have a potential for higher Q-factor since

$$Q = \frac{W}{\Delta W} \tag{2.1}$$

where W is the energy stored in the resonator and ΔW is the energy loss per cycle. ΔW is the sum of all energy drained from the system through various loss mechanisms. While many other formulations for Q-factor can be found, this formulation is particular suitable since expressions for both the kinetic energy and the loss per cycle are readily available in the literature. As BARs are typically operated with amplitudes in the nm range rather than μm range, as the shuttle style resonators described above, squeeze- and slide film effects are less dominant. Also, compared to bending mode resonators, the extensional mode shape is less affected by thermoelastic damping as the distances between hot and cold regions is greater.

While the simplest imaginable micromachined Longitudinal Bulk Resonator (LBR) resonator is a slate beam [84] as depicted in 2.2(c), BARs with many other geometries have also been demonstrated. Examples are annular resonators [84, 86, 90] and square plates in square extensional and Lamé modes [85, 91, 92]. A different class of BARs, which forms the basis for the work presented Part I, are circular disk resonators operating in radial contour modes. Alternative modes are the so-called wine-glass modes [93, 68], but they will not be considered here.

For extensive reviews on recent developments in resonators and other RF MEMS components,

see [94, 95, 96, 97].

2.2.2 Radial contour mode disk resonators

In [83], a disk resonator operating in radial contour mode was presented. The system consisted of a circular disk supported by a stem in its center (Figure 2.3(a)) and two electrodes for actuation and readout partially surrounding the disk periphery. With a diameter of 34 μm and made from pSi, it operated at about 156 MHz with a Q-factor of 9400 at 50 $\mu Torr$. The fabrication process involved different masks for the disk and center stem, which resulted in a misaligned stem and as a result, in distorted mode shapes. This in turn decreased the Q-factor. The process was later improved by defining the disk and stem in the same mask, effectively eliminating any misalignment [2]. With diameters of 36 and 20 μm, the resulting pSi systems operated at 151.3 and 274 MHz in the first mode (Figure 2.3(a)) with Q-factors of 12289 and 8950, respectively. Disk resonators as described here, can also be operated in higher order modes as illustrated in figures 2.3(c) and 2.3(d). The 20 μm system was also characterized for the second and third order mode, where the operating frequencies and the Q-factors were found to be 734.6 MHz and 7890 and 1.156 GHz and 2683, respectively. If these high performance resonators could

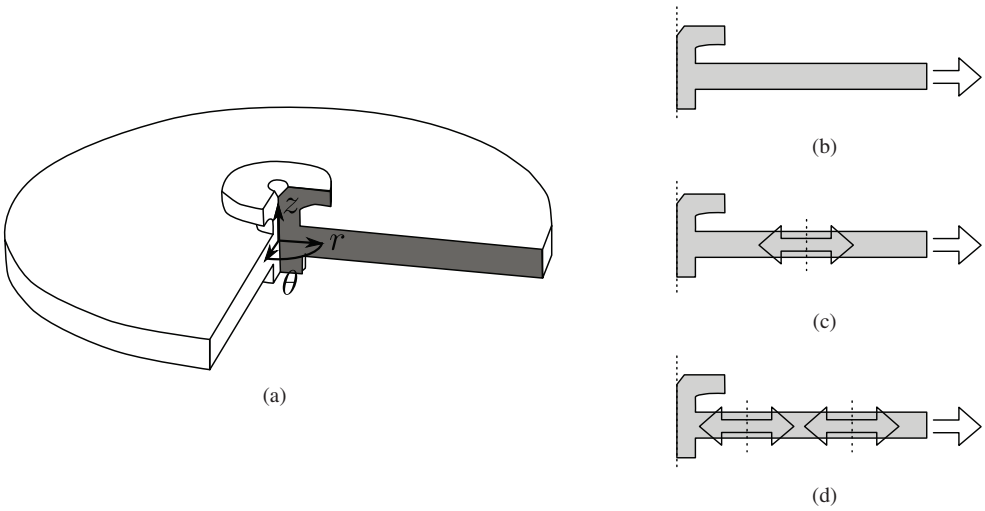

Figure 2.3: (a) 3D sketch of a centrally supported disk resonator excluding the partially surrounding electrodes. A 90^o sections has been hidden to illustrate the axisymmetric cross section. Modal shapes for (b) first, (c) second and (d) third order radial contour modes illustrated. The first order mode has a nodal point only in the center of the disk. The second and third order mode has nodal rings in addition to the center node.

be mechanically coupled, filter with steep roll of characteristic can be achieved or, if the high Q-factor behavior does not permit a flat band pass region, closely spaced single narrow band filters can be made. This forms the ground for the next section.

2.3 Stacked disk resonators

Micromachined disk resonators have been coupled to form filters [98]. However, the disks were placed side by side and occupied a large area on the die, increasing the cost of the system. Also, for certain applications, the size of the complete system can be critical, e.g. in sensor systems including a RF transmitter for in-vivo monitoring of blood vessels [99]. Because of this, we suggested in [18] to stack two disk resonators vertically as illustrated in Figure 2.4. The system

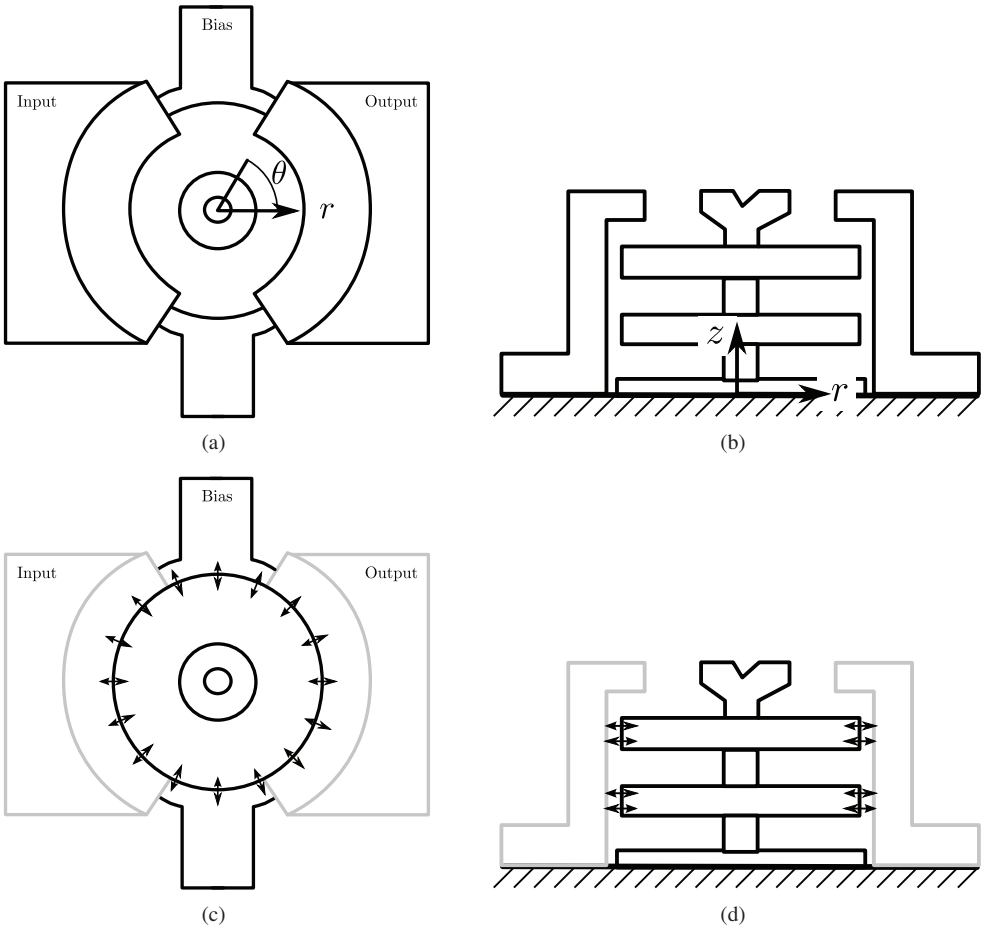

Figure 2.4: (a) Top view and (b) cross section of the proposed stacking of disk resonators. Coordinate system used indicated.c) and d) show idealized vibration pattern.

consists of two disks supported in their center by a stem. It is attached to a bottom electrode on the substrate, and provides means of biasing the disks. Partially surrounding the disks are two electrodes for electrostatic actuation and readout. On the top end of the stem, sits a top hat. The top hat is a residual structure from the fabrication process described in [2] and outlined in subsection 2.8.1. During operation, the disks are set to vibrate radially as illustrated in figures 2.4 c) and d).

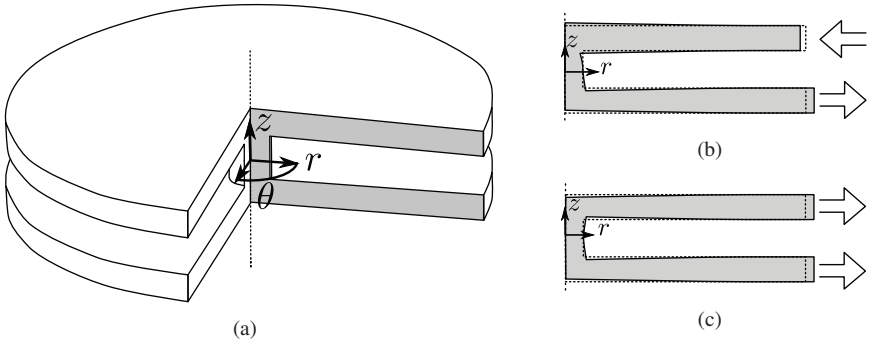

Figure 2.5: A dumbbell as used to derive analytic expressions for coupling mechanisms in stacked disk resonators. A 90^o section has been hidden to illustrate the cross section shown in figures b) and c). The two modes of interest are b) anti-phase and c) in-phase.

2.4 Lumped modeling of stacked disk resonators

2.4.1 Motion analysis

To understand the harmonic deformation of a double disk stacked resonator system, each of the sub-structures in Figure 2.4 and their interactions have to be analyzed. The surrounding near semi-circular electrodes are fixed at their base, and their construction should be sufficiently rigid to withstand deformation from the electrostatic forces resulting from the interaction with the disks. This leaves a system of two disks and a central stem to be analyzed.

A single disk with no stem sections vibrating in free space in a radial contour mode will not only deform radially, but also vertically over its thickness due to the Poisson effect. Such a deformation will be symmetrical about the central plane, and since the radial extension is axisymmetric, this plane will at all times be at rest vertically. This means that also the center of gravity for the disk will be at rest. Connecting two disks of the same diameter via a small diameter central stem, a dumbbell-like structure as illustrated in Figure 2.5, is formed.

With two identical and interconnected disks vibrating in a radial contour mode, two distinct modes will appear near the single disk modal frequency. The modes are identified by the disk perimeters being either in opposite (anti-phase) or in phase (in-phase), as illustrated in figures 2.5(b) and 2.5(c), respectively.

The dumbbell anti-phase mode

For the anti-phase mode, the disks perimeters are in opposite phase as illustrated in Figure 2.5(b). Because of this, the disk surfaces facing each other are in phase, effectively shuffling the stem section up and down between the disks. This means that the only forces involved for the stem along the z-axis, are those resulting from its own inertia. The energy involved in this motion is assumed to be small compared to the energy of the disks.

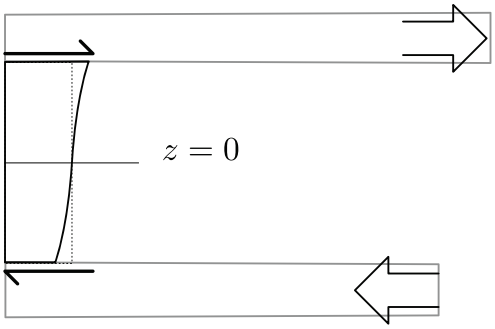

Figure 2.6: Due to the antisymmetric loading of the stem at the interfaces with the disks, the stem will deform antisymmetric with respect to a plane at $z = 0$.

Since the stem is attached to the disk and the energy of the disk is large compared to that of the stem, a first order approximation is that the stem follows the motion of the disk. This means that each end of the inter-disk stem section will be subject to radial shear forces resulting in radial deformation with an anti-symmetry plane at the stem center as illustrated for $z = 0$ in Figure 2.6. The stiffness and mass this deformation represents, adds to the stiffness and mass of the disk and increase the frequency of the system.

The effect of shear forces and added effective stiffness due to the stem will also be present for a single disk system with a central stem, and is a coupling effect between the disk and stem. For a dumbbell system, this means that both an anti-symmetry and a symmetry plane exist in the middle of the stem. This means that the effect from the radial deformation will also affect the frequency of the in-phase mode.

The dumbbell in-phase mode

For the in-phase mode, the perimeters of the disks move in phase. Because of the Poisson effect, the inner disk surfaces facing each other will be in opposite phase. This means that the ends of the inter-disk stem will be subjected to equal but oppositely directed forces. Due to the symmetric loading, the longitudinal deformation of the stem will have a nodal point at rest in its center.

Since the vertical vibrational amplitude is only a small fraction of the radial amplitude and its mass is assumed to be much smaller than the mass of the full system, the vibrational energy of the stem will account for only a small fraction of the energy of the whole system. As a first order approximation, it is therefore assumed that due to the symmetric loading of the stem and the relatively large mass of the disks, also the center of the disks can be considered to be at rest. This is illustrated in Figure 2.5(c).

As argued above, the added stiffness from the radial deformation of the stem will also be present for the in-phase mode, but with the deformation which is symmetric over the center

plane of the stem.

Dumbbell anchored to the bulk

While the dumbbell discussed above is useful for gaining insight, a real double disk resonator must be anchored to the substrate. As illustrated in Figure 2.4, this can conveniently be done with a central stem through both disks. Hence, a complete model must also account for the effects of interaction between the dumbbell and the bottom stem section. For the anti-phase mode, this means that the bottom disk will be subject to radial shear forces not only at the surface facing the top disk, but also at the bottom surface. For the in-phase mode, the net inertial force from the dumbbell to the bottom stem is zero. This can be argued from the assumption that the center of gravity for both disks and the inter-disk stem section are at rest. Hence, the forces and deformation of the bottom stem can only be caused by the thickness deformation of the bottom disk. Similar as for the inter-disk stem section, the anti-phase mode will introduce radial shear forces to the top of the bottom stem, but in contrast to for the inter-disk stem section, one end of the bottom stem is fixed. The deformation from both the shear forces at the disk interface and the longitudinal loads must therefore distribute over the full length of the stem.

Top hat

For the anti-phase mode, the top hat affects the top disk in the same way as how the bottom stem section affects the bottom disk: as an additional radial stiffness. If the top hat is considered as a stem stub of constant radius, a radial deformation at the disk interface will cause a radial deformation distributed over the full length of the stem stub. Since the real profile of the top hat is wider at the free end, it can be treated as much stiffer compared to the end at the disk interface. Thus one can assume the free end as radially fixed and treat the top hat in the same manner as the bottom stem.

With the top hat free to move up and down, the periodic deformation of the top disk will generate inertia forces from the mass of the top hat. Because the top disk has a center of gravity assumed to be at rest, the vertical amplitude of the center of gravity for the top hat can be assumed to be equal to the deformation over half the thickness of the top disk. Similar as for the other stem sections, the mass and kinetic energy of the top hat is small compared to the mass and energy of the disks. Hence, the inertial forces of the top hat can be assumed to be negligible, which in term means that the top hat is assumed to have no effect on the frequency of the in-phase mode.

Discretization of stacked disk structure

In order to describe the behavior of the various structural members of the system, their properties can be represented by a set of interconnected Spring-Mass-Dashpots (SMDs). If only considering vertical motion, the system of stacked disks can be modeled as illustrated in Figure 2.7. Due to the symmetric deformation over the disk center plane, the disk property of each

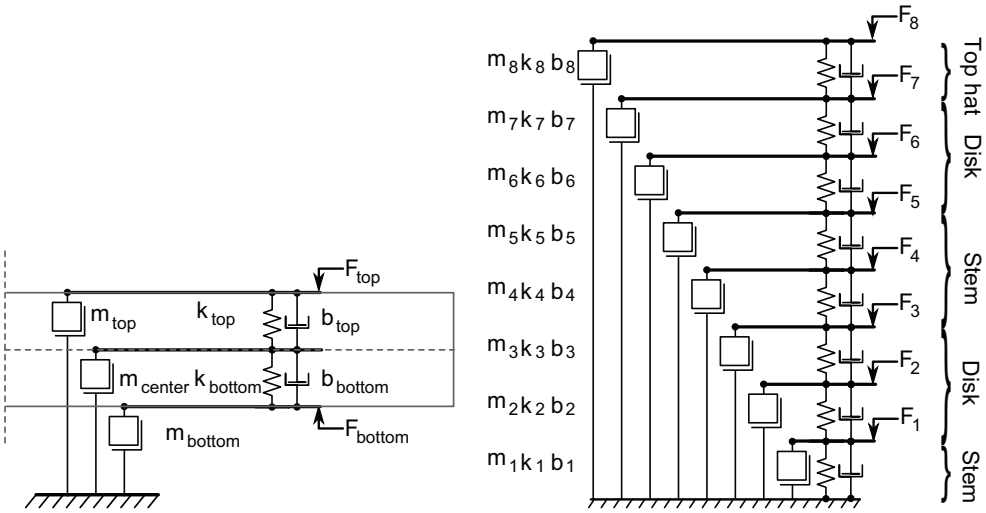

Figure 2.7: (a) Each disk is described by two springs, two dashpots and three masses connecting three DOFs. The reaction forces act on the surface of the disk. Disk cross section outlined in gray. (b) The vertical motion of full system can be described by assembling eight levels of SMDs. Similar to the disk, the inter-disk stem requires three DOFs to reproduce the symmetric deformation. The bottom stem can be accounted for by two DOFs.

disk can be represented by three nodes with three masses, two springs and two dashpots as illustrated in Figure 2.7(a). Likewise, the three stem sections are represented by separate SMDs. For each *level*, which is referred to as a node, a force can be assigned. In Figure 2.7(b), all forces will be zero except F_2, F_3, F_6 and F_7 which are reaction forces from the thickness deformation over the disks. These forces can be expressed

$$F_2 = -F_3 = F_6 = -F_7 = k_{dzz} \times u_{zz} k_{top} = (k_{top} + k_{bottom}) \times 2u_{zz} \tag{2.2}$$

where k_{dzz} and u_{zz} are the equivalent stiffness and deformation over half the disk thickness. The relationship between the vertical deformation, u_{zz} , and the disk perimeter amplitude A_d will be described in detail in subsection 2.4.3.

Materials

Radial contour disk resonators are typically fabricated using SMM techniques [83, 2], which typically means that poly-crystalline materials are used. The most common material for fabricating SMM resonators is pSi, although multi-material systems have also been used [100]. For simplicity, all resonator structures described below are assumed to be from pSi with material properties as listed in Table 2.1.

Table 2.1: Material parameters used for pSi

	Poly silicon	Reference
Young's modulus	160 GPa	[101]
Poisson's ratio	0.22	[101]
Density	2330 kg/m^3	[14]

Other assumptions made

In addition to the assumptions made above, the following assumptions are made to simplify the modeling:

- Disk amplitudes are taken to be equal in magnitude for both disks for both modes.
- Disk deformation is taken to be perfectly axisymmetric extensional.
- All materials are assumed to be lossless.
- The disks are assumed to be identical.

Approximate functions for stem deformation

The dimensional notation used is shown in Figure 2.8.

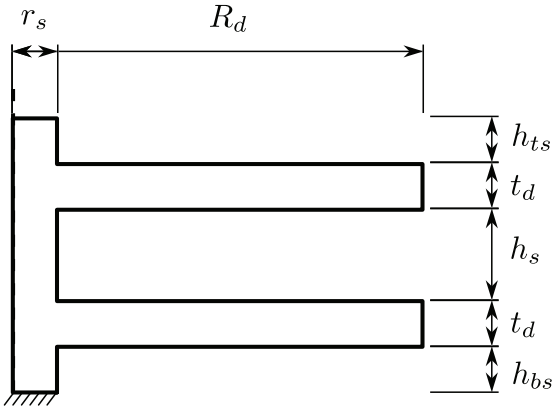

Figure 2.8: Notation used for dimensional features.

For calculating the kinetic energy of the stems, used for calculating the equivalent stiffness and mass for both modes, the velocity in the stem at radial coordinate r must be found. As the radial deformation of the disk is known and a first approximation is that the stem end follows the disk surface, one can estimate the deformation profile along the length of the stem. There are three deformation states which require individual functions. For the anti-phase mode, the inter-disk stem is only subject to oppositely directed shear forces at each end. This is illustrated in Figure 2.9(a). For the in-phase mode, the radial deformation is symmetric about the stem

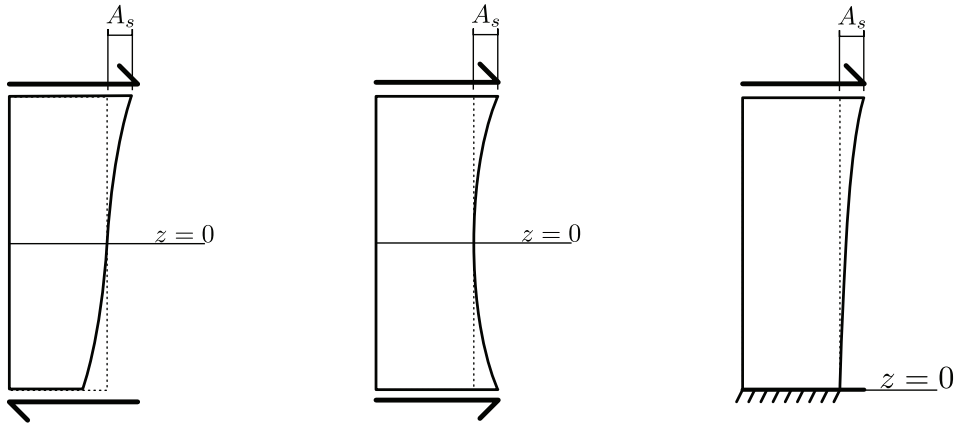

(a) (b) (c)

Figure 2.9: (a) The inter-disk stem section is subject to oppositely directed shear forces at the ends. The radial deformation is therefore antisymmetric over the center of the stem. (b) For the symmetric mode the radial deformation is symmetric over $z = 0$ while for the bottom stem in (c) the deformation is distributed over the whole length of the stem.

center and for the bottom stem only one end of the stem is deformed radially as illustrated in figures 2.9(b) and 2.9(c), respectively. Assuming the approximation for the deformation of the stem radius ($\Delta r_s(z, r)$) is on the form

$$\Delta r_s(z, r) = A_s(r)(a + bz + cz^2) \tag{2.3}$$

where the second part is a function normalized at the disk interface. Setting $A_s(r) = 1$, one can formulate conditions that allows finding the coefficients.

For the anti-phase mode and inter-disk stem section, the deformation at $\Delta r_s(0, r_s) = 0$, which means $a = 0$. The coefficient b can be found from requiring that

$$\Delta r_s\left(\frac{h_s}{2}, r\right) == 1 \tag{2.4}$$

$$\Downarrow$$

$$b = \frac{4 - c{h_s}^2}{2h_s} \tag{2.5}$$

The antisymmetric radial deformation requires that

$$\frac{d\Delta r_s(0, r)}{dz} \geq 0 \tag{2.6}$$

which gives

$$c = \frac{\eta}{{h_s}^2} \tag{2.7}$$

where η is a fitting parameter which must be less than four. As illustrated in Figure 2.9, a deformation with the largest displacement at the disk interface which gradually decrease towards a center of the stem, requires that

$$\frac{d\Delta r_s(h_s, r)}{dz} > \frac{d\Delta r_s(0, r)}{dz} \tag{2.8}$$

which gives

$$\eta \in [0 \ldots 4 > \tag{2.9}$$

In the in-phase mode, it is likely that there will be a radial deformation at the center of the stem. For a first order model, this is assumed negligible, which means $a = 0$. The symmetric deformation requires

$$\frac{d\Delta r_s(0, r)}{dz} = 0 \tag{2.10}$$

which gives $\eta = 4$.

Contrary to for the inter-disk stem, the deformation of the bottom stem distributes over the full length of the stem. Since it is fixed at the bottom the conditions used for finding the fitting parameters used for the in-phase mode can be used for the full stem length. This gives

$$b = \frac{1 - c{h_{bs}}^2}{h_{bs}} \tag{2.11}$$

$$c = \frac{1}{{h_{bs}}^2} \tag{2.12}$$

Table 2.2: Table summarizing coefficients for (2.3) and the various radial deformation states.

Coefficient	**a**	**b**	**c**	
Inter-disk stem				
Anti-symmetric mode	0	$\frac{4-c{h_s}^2}{2h_s}$	$\frac{\eta}{{h_s}^2}$	$\eta \in [0 \ldots 4 >$
Symmetric mode	0	$\frac{4-c{h_s}^2}{2h_s}$	$\frac{4}{{h_s}^2}$	
Bottom stem				
Anti-symmetric mode	0	$\frac{1-c{h_{bs}}^2}{h_{bs}}$	$\frac{1}{{h_s}^2}$	
Symmetric mode	0	$\frac{1-c{h_{bs}}^2}{h_{bs}}$	$\frac{1}{{h_s}^2}$	

2.4.2 Single-disk model

The model for axisymmetric radial extensions of a thin disk, can be found in various versions in the literature [2, 3], but all are based on a classic paper by Onoe [102]. They are all equivalent and here the formulation from [3] has been used.

The resonance frequency for a disk of thickness t_d and radius R_d, with a Young's modulus E_y, a Poisson's ratio ν and density ρ, can be expressed as

$$\omega_d = \frac{\kappa}{R_d}\sqrt{\frac{E_y}{\rho_d(1-\nu^2)}} \tag{2.13}$$

where κ is a parameter accounting for the modal shape and the material properties. While numerical values for κ can be found in the literature, here it is chosen such that the calculated frequency coincide with FEA results for an unconstrained single disk. Values used, are listed in Table B.3.

The radial displacement at radial coordinate r can be expressed as [3]

$$U(r) = A_d J_1\left(\frac{\kappa r}{R_d}\right) \tag{2.14}$$

where A_d is the complex amplitude at the disk perimeter and J_1 is the Bessel function of the first kind and first order. Assuming a time harmonic displacement of the form

$$u_r(r) = U(r)e^{\imath\omega_d t} \tag{2.15}$$

the kinetic energy can be written as

$$KE_{disk} = \int_0^{R_d}\int_0^{t_d}\int_0^{2\pi} \rho\frac{1}{2}\left(\omega_d J_1\left(\frac{\kappa r}{R_d}\right)\right)^2 d\theta dz dr \tag{2.16}$$

where ω_d is found from (2.13).

For later, it is useful to derive expressions for the equivalent mass and stiffness for the disk perimeter. Inserting (2.16) into (1.3), with the radial perimeter velocity ($\dot{u}_r(R_d)$), the equivalent mass for the disk perimeter is obtained as

$$m_{diskrr} = \frac{\kappa\rho {R_d}^2 t_d\left(\kappa J_0(\kappa)^2 - 2J_1(\kappa)J_0(\kappa) + \kappa J_1(\kappa)^2\right)}{\pi(H_0(\kappa)J_1(\kappa) - H_1(\kappa)J_0(\kappa))^2} \tag{2.17}$$

where H_0 and H_1 are Struve functions of zeroth and first order respectively. Inserting (2.17) into (1.4), the corresponding equivalent stiffness is obtained:

$$k_{diskrr} = {\omega_d}^2 m_{diskrr} \tag{2.18}$$

The disk perimeter displacement can be obtained from inserting $r = R_d$ in (2.14) which gives

$$u_{diskrr} = A_d J_1(\kappa) \tag{2.19}$$

2.4.3 Dumbbell model

Having found the kinetic energy for a single disk, the coupling velocities for each of the two modes of the symmetric two disk system are needed to calculate the effective mass for each mode. For both modes, the coupling is at the interface with the stem. From the discussion in subsection 2.4.1, it is clear that both the radial and the vertical coupling velocities are needed in order to describe the mechanisms affecting the modal frequencies.

Anti-phase mode

In the anti-phase mode, the radial velocity $v_{rr}(r)$ at the disk surface can be found as the time derivative of (2.15). Because the displacement over the disk thickness varies with radial location, an average velocity will reflect the energy transfer more correctly than a point velocity in the disk center. Averaged over the stem-disk interface, it is:

$$\bar{v}_{rr} = \frac{\int_0^{2\pi}\int_0^{r_s} v_{rr}(r, t_d/2)drd\theta}{\pi {r_s}^2} \tag{2.20}$$

Inserting (2.20) and (2.16) into (1.3) gives the radial equivalent mass at the stem interface as

$$m_{drr} = \frac{9\pi\rho {R_d}^4 t_d}{\kappa^3 {r_s}^2} \frac{\left(\kappa {J_0}^2(\kappa) - 2J_1(\kappa)J_0(\kappa) + \kappa {J_1}^2(\kappa)\right)}{{}_1{F_2}^2\left(\frac{3}{2}; 2, \frac{5}{2}; -\frac{\kappa^2 {r_s}^2}{4{R_d}^2}\right)} \tag{2.21}$$

where ${}_1F_2$ denotes a hyper geometric function

$${}_1F_2\left(\frac{3}{2}; 2, \frac{5}{2}; -\frac{\kappa^2 {r_s}^2}{4{R_d}^2}\right) = \frac{3\pi {R_d}^2}{(\kappa r_s)^2}\left(J_1\left(\frac{\kappa r_s}{R_d}\right)H_0\left(\frac{\kappa r_s}{R_d}\right) - J_0\left(\frac{\kappa r_s}{R_d}\right)H_1\left(\frac{\kappa r_s}{R_d}\right)\right) \tag{2.22}$$

Inserting (2.21) and (2.16) into (1.4), the following equivalent stiffness for the radial motion is found

$$k_{drr} = {\omega_d}^2 m_{drr} \tag{2.23}$$

The anti-phase mode corresponds to a radial deformation of the stem. It is modeled using the radial coupling velocity (2.20) and the kinetic energy of the stem when deformed as described in subsection 2.4.1 where it was assumed that no longitudinal deformation of the stem takes place for the anti-phase mode. From section 2.4.1:

$$\Delta r_s(r, z) = A_s(r)\left(\frac{4-\eta}{2h_s}z + \frac{\eta}{{h_s}^2}z^2\right) \quad \eta \in [0 \ldots 4> \tag{2.24}$$

where η is a fitting factor and $A_s(r)$ is the disk amplitude at radial coordinate r.

$$A_s(r) = A_d J_0\left(\frac{\kappa r}{R_d}\right) \tag{2.25}$$

Because of the antisymmetric deformation, only half the stem is considered. Its kinetic energy is found by integrating the time derivative of the displacement profile (2.24) over the volume of

half the length of the stem, for the mode anti-phase mode frequency. Assuming time dependence in the form of (2.15), gives

$$KE_{stem} = \frac{(160-20\eta+\eta^2)}{15360}\frac{\pi\kappa^2\rho {A_d}^2{\omega_d}^2 h_s {r_s}^4}{{R_d}^2}{}_1F_2\left(\frac{3}{2};3,3;-\frac{\kappa^2 r_s^2}{R_d^2}\right) \tag{2.26}$$

When expanded the hypergeometric function is

$$\begin{aligned} {}_1F_2\left(\frac{3}{2};3,3;-\frac{\kappa^2 {r_s}^2}{{R_d}^2}\right) &= \frac{8{R_d}^2}{\kappa^2 r_s^2} \\ &\times \left({J_0}^2\left(\frac{\kappa r_s}{R_d}\right)+{J_1}^2\left(\frac{\kappa r_s}{R_d}\right)-\frac{2R_d}{\kappa r_s}J_0\left(\frac{\kappa r_s}{R_d}\right)J_1\left(\frac{\kappa r_s}{R_d}\right)\right) \end{aligned} \tag{2.27}$$

Inserted into (1.3) and (1.4), using the coupling velocity from (2.20) and using $\eta = 3$, the expression for equivalent mass is

$$m_{srr} = \frac{327\pi\rho h_s {r_s}^2}{2560}\frac{{}_1F_2\left(\frac{3}{2};3,3;-\frac{\kappa^2 {r_s}^2}{{R_d}^2}\right)}{{}_1{F_2}^2\left(\frac{3}{2};2,\frac{5}{2};-\frac{\kappa^2 {r_s}^2}{4{R_d}^2}\right)} \tag{2.28}$$

Because the relationship between equivalent mass and stiffness is found from its resonance frequency (ref. 1.4), the equivalent stiffness is then found as

$$k_{srr} = {\omega_s}^2 m_{srr} \tag{2.29}$$

where ω_s is found from inserting the stem radius into (2.13).

The resonance frequency of the anti-phase mode of the dumbbell can now be found as

$$\omega_{dasym} = \sqrt{\frac{k_{drr}+k_{srr}}{m_{drr}+m_{srr}}} \tag{2.30}$$

In-phase mode

To combine the effects from both radial and longitudinal stem deformation in the model for the in-phase mode, the equivalent stiffness and mass for a disk with half the inter-disk stem attached, is found before a resonant frequency of the disk-stem assembly is calculated. This frequency is then used in all later operations to calculate the kinetic energies and the coupling velocity for the vertical motion.

Similarly as for the radial stiffness and mass for the anti-phase mode, the basis frequency for the in-phase mode is

$$\omega_{dsymbasis} = \omega_{dasym}\ with\ \eta = 4 \tag{2.31}$$

The coupling effect is assumed to be due to a thickness deformation in the disks. It is found by integrating the strain over the thickness of the disk. The vertical strain at location r can be

formulated as [3]

$$\varepsilon_{zz}(r) = \frac{\nu}{\nu - 1} \frac{\kappa A_d J_0\left(\frac{\kappa r}{R_d}\right)}{R_d} \tag{2.32}$$

where J_0 is a Bessel function of the first kind and zeroth order. The vertical deformation at location (r, z) relative to the center of the disk can be expressed as a linear function in z

$$u_{zz}(r, z) = z\varepsilon_{zz}(r) \tag{2.33}$$

Inserting (2.15) into (2.33) and finding the time derivative, the vertical velocity amplitude is expressed as

$$v_{zz}(r, z) = \omega_{dsymbasis} u_{zz}(r, z) \tag{2.34}$$

To find the effective coupling velocity, the energy transfer at the stem interface must be considered. It is reflected by the average coupling velocity at the stem/disk interface, which can be found as

$$\bar{v}_{zz} = \frac{\int_0^{2\pi} \int_0^{r_s} v_{zz}(r, t_d/2) dr d\phi}{\pi {r_s}^2} \tag{2.35}$$

Inserting (2.35) and (2.16) into (1.3) and using the $\omega_{dsymbasis}$ from (2.31) to calculate the kinetic energy and coupling velocity for one disk, the equivalent mass for the vertical deformation of a single disk is

$$m_{dzz} = \frac{(\nu - 1)^2}{\nu^2} \frac{\pi \rho {R_d}^2 {r_s}^2}{\kappa t_d} \frac{\left(\kappa {J_0}^2(\kappa) - 2J_1(\kappa)J_0(\kappa) + \kappa {J_1}^2(\kappa)\right)}{{J_1}^2\left(\frac{\kappa r_s}{R_d}\right)} \tag{2.36}$$

Inserting this equivalent mass into (1.4) we obtain the following equivalent stiffness for vertical motion with a stem with radius r_s

$$k_{dzz} = {\omega_{dsymbasis}}^2 m_{dzz} \tag{2.37}$$

Because of both mechanical and practical fabrication issues, the length of the inter-disk stem is typically less than 1 μm. For wavelengths much longer than the stem this means that a quasi static approach can be used, meaning that static values for masses and stiffnesses are used for the stem properties. The mass of a rod of height h_s and radius r_s is

$$m_{szz} = \rho h_s \pi {r_s}^2 \tag{2.38}$$

This expression also appears if we use the energy based approach outlined in subsection 1.4.1 [54]. The axial stiffness can be found as [52]

$$k_{szz} = \frac{E_y \pi {r_s}^2}{h_s} \tag{2.39}$$

The stem has a nodal point at the center, which means that half its lumped mass is assigned to the nodal point at its center and one quarter to each end.

The in-phase modal frequency for the dumbbell can now be found as

$$\omega_{dsym} = \sqrt{\frac{k_{dzz} + 2k_{szz}}{m_{dzz} + m_{szz}/4}} \tag{2.40}$$

2.4.4 Bottom stem and top hat

Similar to the inter-disk stem section, the bottom stem is loaded and deformed differently for the two modes but now the stem is clamped at the base. For the in-phase mode, the bottom stem is loaded vertically. For a bottom stem of height h_{bs} and radius r_{bs}, we then have, assuming a uniform load distribution over the cross section and assuming a stem length much less than the wavelength, its mass and stiffness can be approximated by

$$m_{bszz} = \rho h_{bs} \pi {r_{bs}}^2 \tag{2.41}$$

$$k_{bszz} = \frac{E_y \pi {r_{bs}}^2}{h_{bs}} \tag{2.42}$$

Contrary to the case of the inter-disk stem section, the bottom stem is deformed over its full length and, accordingly, the full stiffness is used in the final system assembly.

For the anti-phase mode, the equivalent mass and stiffness of the bottom stem is found in a similar fashion as for the inter-disk stem section, but with no radial deformation at the base of the stem. The kinetic energy is then found through integration over a radial velocity profile found from an approximated displacement profile for the modal frequency of the disk. From section 2.4.1 and equations (2.11) and (2.12), the approximation function is

$$\Delta r_{bs}(r, z) = A_s(r) \left(\frac{z}{h_{bs}} \right)^2 \tag{2.43}$$

For the radial deformation, the kinetic energy is then found to be

$$KE_{bs} = \frac{\pi \kappa^2 \rho {A_d}^2 h_{bs} {\omega_d}^2 {r_s}^4}{80 {R_d}^2} \, {}_1F_2 \left(\frac{3}{2}; 3, 3; -\frac{\kappa^2 {r_s}^2}{{R_d}^2} \right) \tag{2.44}$$

Inserting (2.44) and (2.20) into (1.3) and (1.4) gives the following expressions for equivalent mass and stiffness of the radial deformation for the bottom stem:

$$m_{bsrr} = \frac{9\pi \rho h_{bs} {r_s}^2}{40} \frac{{}_1F_2 \left(\frac{3}{2}; 3, 3; -\frac{\kappa^2 {r_s}^2}{{R_d}^2} \right)}{{}_1{F_2}^2 \left(\frac{3}{2}; 2, \frac{5}{2}; -\frac{\kappa^2 {r_s}^2}{4{R_d}^2} \right)} \tag{2.45}$$

$$k_{bsrr} = {\omega_s}^2 m_{bsrr} \tag{2.46}$$

As vertical inertia forces are assumed to be negligible, the top hat section is not included for the symmetric mode model. For the anti-phase mode, the top hat contributes with an additional radial stiffness to the top disk which can be found in a similar fashion that of the bottom stem. As argued in subsection 2.4.1, it is assumed that the stem section can be approximated by a

stem stub of constant radius, whose free end has no radial amplitude and that its height is the same as for the bottom stem.

2.4.5 Model assembly

To find the frequency of the two modes, the stiffnesses and masses are summed over all active components as in (1.5). The stiffnesses and masses relevant to the symmetric mode are those of the longitudinal modes of the inter-disk and bottom stem, as well as the equivalent mass and stiffness of the vertical deformation for the disks. For the inter-disk stem, one quarter of the mass and the stiffness for half the stem are assigned to each of the disks due to the symmetry. For the bottom stem, half the mass is assigned to each end and the full stiffness is used. As inertial forces are assumed negligible, the top hat does not deform, and its full mass is included in the calculations. This yields the following expression for the frequency of the symmetric mode of the system

$$\omega_{sym} = \sqrt{\frac{k_{bszz} + 4k_{szz} + 2k_{dzz}}{\frac{m_{bszz}}{2} + 2\frac{m_{szz}}{4} + 2m_{dzz} + m_{thzz}}} \tag{2.47}$$

where $m_{thzz} = m_{bszz}$.

For the antisymmetric mode, the relevant masses and stiffnesses are the radial equivalent stiffness and masses of the disks and of all the stem sections. Due to the symmetry of the model, only half the structure needs to be included in the model. The anti-phase modal frequency is then:

$$\omega_{asym} = \sqrt{\frac{k_{bsrr} + k_{srr} + k_{drr}}{m_{bsrr} + m_{srr} + m_{drr}}} \tag{2.48}$$

2.4.6 Equivalent circuit modeling

Figure 2.7 illustrates a lumped parameter system describing the vertical motion of key locations in the stacked disk resonator system. Using the *effort-to-current* scheme described in section 1.4.3, it can be converted to an equivalent circuit by replacing forces with current sources, dashpots with resistors, compliances with inductors and masses with capacitors. As all materials were assumed to be lossless, all the resistors values can be set to zero. However, this would cause numerical problems when simulating the circuit, and suitable resistor values should be chosen for the disks resistors to reach a chosen Q-factor. The problem of *simulating* the Q-factor is addressed separately in chapter 3, where a simple model suitable for conversion to equivalent circuit form and integration with this model is investigated.

As only the reaction forces from the deformation over the thickness of the disk contribute to vertical motion, and as argued in section 2.4.1, only the current sources I_2, I_3, I_6 and I_7 are assigned values. Also, since of the symmetrical deformation over the disk thickness will cause reaction forces of opposite directions, the current sources of each disk are also oppositely directed. The resulting equivalent circuit is illustrated in Figure 2.10(a). To extend this model

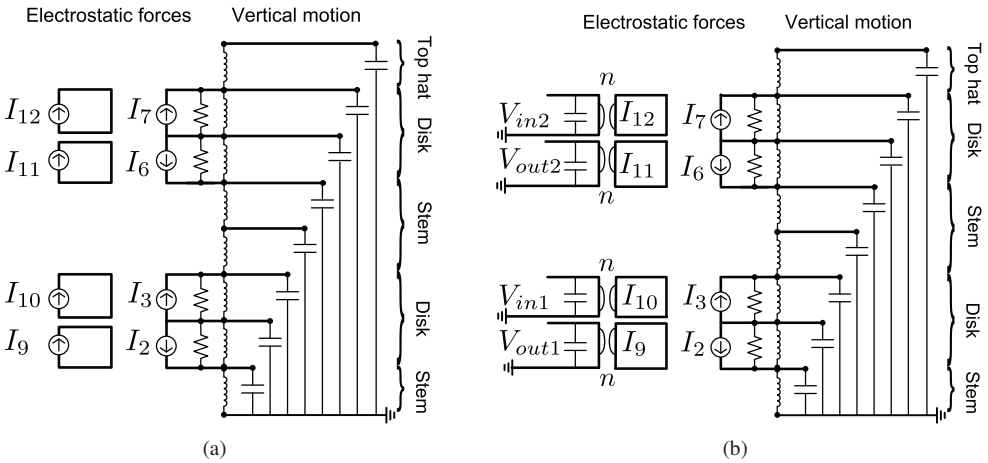

Figure 2.10: (a) After simplification and transformation of the mechanical model illustrated in Figure 2.7, the equivalent circuit has one capacitor for each mass, one inductor for each spring, two resistors and two oppositely directed current sources for each disk. The perimeter displacement to vertical deformation is governed by the relationship between the current sources I_2, I_3 and I_9, I_{10}, and I_6, I_7 and I_{11}, I_{12}. (b) In order to transform the equivalent circuit to have a voltage controlled interface, gyrators are used and replace the current sources. The gyrator's turn ratio, n is the same for all, as the electrode area of all electrodes can be considered to be identical.

to account for the electrostatic gaps and enable full system simulation, including interaction effects with other circuitry, it is necessary to relate the voltage input, as commonly used, to the vertical motion.

The electrostatic forces applied between each electrode and disk perimeter is

$$F_{elec}(V) = \frac{\varepsilon_0 \varepsilon_r A V^2}{(g_0 - u_{rr})^2} \tag{2.49}$$

where A is the electrode area, g_0 is the initial gap and ε_0 and ε_r are the vacuum permitivity and relative permitivity, respectively. The corresponding reaction force at the perimeter of a lossless disk is

$$F_{rr} = k_{diskrr} u_{rr} + m_{diskdrr} \ddot{u}_{diskrr} \tag{2.50}$$

where u_{rr} is the instantaneous radial displacement at the disk perimeter. Since the radial deformation u_{rr} is locked in phase with the deformation over the thickness, $u_{zz}(r_s, t_d/2)$, and the aim is to relate the currents I_2, I_3 to I_9, I_{10} and I_6, I_7 to I_{11}, I_{12}, the inertia forces are not relevant to include as they will be accounted for by the capacitances in the circuit for the vertical motion. As the forces acting on the surface of the disks are opposite directed and of equal magnitude (ref. Figure 2.10(b)), it should be clear that $I_2 = I_3$ and $I_6 = I_7$.

Assuming an ideal and an perfectly symmetric deformation over the thickness of the disk, the reaction force F_{zz} on each surface can be described by

$$F_{zz} = 2k_{dzz}u_{zz} \tag{2.51}$$

where $2k_{dzz}$ is used in order to achieve conservation of energy when two spring elements are used to describe the equivalent stiffness of the disks. Replacing A_d in (2.32) with u_{rr} and inserting it in (2.33), one can express the relationship between u_{rr} and u_{zz} as

$$u_{rr} = u_{zz}\frac{\nu-1}{\nu}\frac{2R_d}{t_d\kappa J_0\left(\frac{r_s\kappa}{Rd}\right)} \tag{2.52}$$

Inserting (2.52) into (2.50) and replacing u_{zz} with $F_{zz}/(2k_{zz})$ one has

$$F_{rr} = k_{diskrr}\frac{F_{zz}}{k_{zz}}\frac{\nu-1}{\nu}\frac{R_d}{t_d\kappa J_0\left(\frac{r_s\kappa}{Rd}\right)} \tag{2.53}$$

Replacing forces with currents, we then have

$$I_2 = I_3 = F_{zz} \tag{2.54}$$

$$I_7 = I_6 = F_{zz} \tag{2.55}$$

$$(I_9 + I_{10}) = I_3\frac{k_{diskrr}}{k_{zz}}\frac{\nu-1}{\nu}\frac{R_d}{t_d\kappa J_0\left(\frac{r_s\kappa}{R_d}\right)} \tag{2.56}$$

$$(I_{11} + I_{12}) = I_7\frac{k_{diskrr}}{k_{zz}}\frac{\nu-1}{\nu}\frac{R_d}{t_d\kappa J_0\left(\frac{r_s\kappa}{R_d}\right)} \tag{2.57}$$

2.5 FEA reference model

The devices explored here have not yet been fabricated and hence data for model comparison must be extracted from high fidelity FEA. Also, using FEA, a detailed understanding of the mechanisms of the device can be achieved and shortcomings of the model can be uncovered. To minimize the computational effort, an axisymmetric model has been used. In this work the focus has been on the frequency separation between the two lowest order modes. This means that the analysis can be performed using modal analysis, allowing AC signal input and the surrounding electrodes to be disregarded. The model is therefore simplified to consist of only three parts: two disks and a stem penetrating both of them as illustrated in Figure 2.11. The stem is fixed at the base.

A mesh convergence study was performed using the h-method [55]. The mesh density was increased until no noticeable change in modal frequencies was obtained by further mesh refinement. All subsequent simulations were performed with an equal or higher mesh density.

The material parameters used in the model are listed in Table 2.1. Since an axisymmetric model was used, only axisymmetric modes are accounted for. Depending on the ratio between the disk radius and thickness, there are bending modes at frequencies close to the axisymmetric extensional modes. Initial simulations show that these modes may pass though the frequency range of the double disk resonator when the stem radius is changed. This is not accounted for

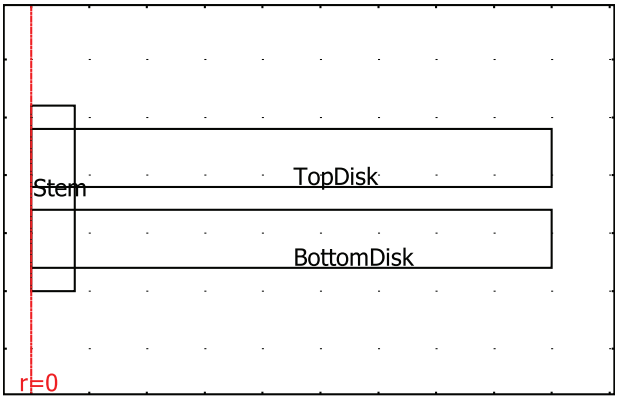

Figure 2.11: For the reference FEA, an axisymmetric model has been used to minimize the computational effort. The model consists of three parts: two disks and a central stem clamped at the base. The stem shape over the top disk has been simplified to a circular rod. Screen dump from COMSOL of model used.

in the analytical model. Therefore 980 parameterized simulations were run using a script to find parameter spaces for which the analytical model is valid. The simulated disks had radius to thickness ratios in the range 6 to 12, with disk radii varying in $2\mu m$ steps from $16\mu m$ to $28\mu m$. In addition, the stem radius was varied from $0.05\mu m$ to $2\mu m$ in 20 steps, to include a range of radii spanning from unrealistically small values to beyond where the model and results from FEA diverge. For all simulations, all stem heights were 0.8 μm, including the stub used for approximating the top hat. A complete listing of parameters used can be found in Appendix B.

2.6 Modeling results

This section is divided into three sections. First, the functions (2.24) and (2.43) used for approximating the stem sections' radial deformations are evaluated. In subsection 2.6.2, results from FEA and the analytic model of the dumbbell are given. Finally, the effects of the stem and top hat are included and the results from both FEA and the analytic model, are presented in subsection 2.6.3.

2.6.1 Verification of the approximation function and coefficients

To evaluate the function used for approximating the radial stem deformation described in subsections 2.4.3 and 2.4.4, the coefficients listed in Table 2.2 are inserted and compared with the corresponding radial displacement profiles extracted from FEA. For the inter-disk stem, data are extracted from the center and up to the stem surface as illustrated in Figure 2.12(a). For the bottom stem, the displacement is extracted over the full stem length as illustrated in Figure 2.12(c). The data extracted are normalized such that they will have a unit displacement at $z = h_b/2\mu m$ and $z = h_{bs}$ which means 0.4 μm and $0.8\mu m$, for the systems featured in Figure 2.12. Figure 2.12(b) shows a comparison between the approximate displacement profile (2.24)

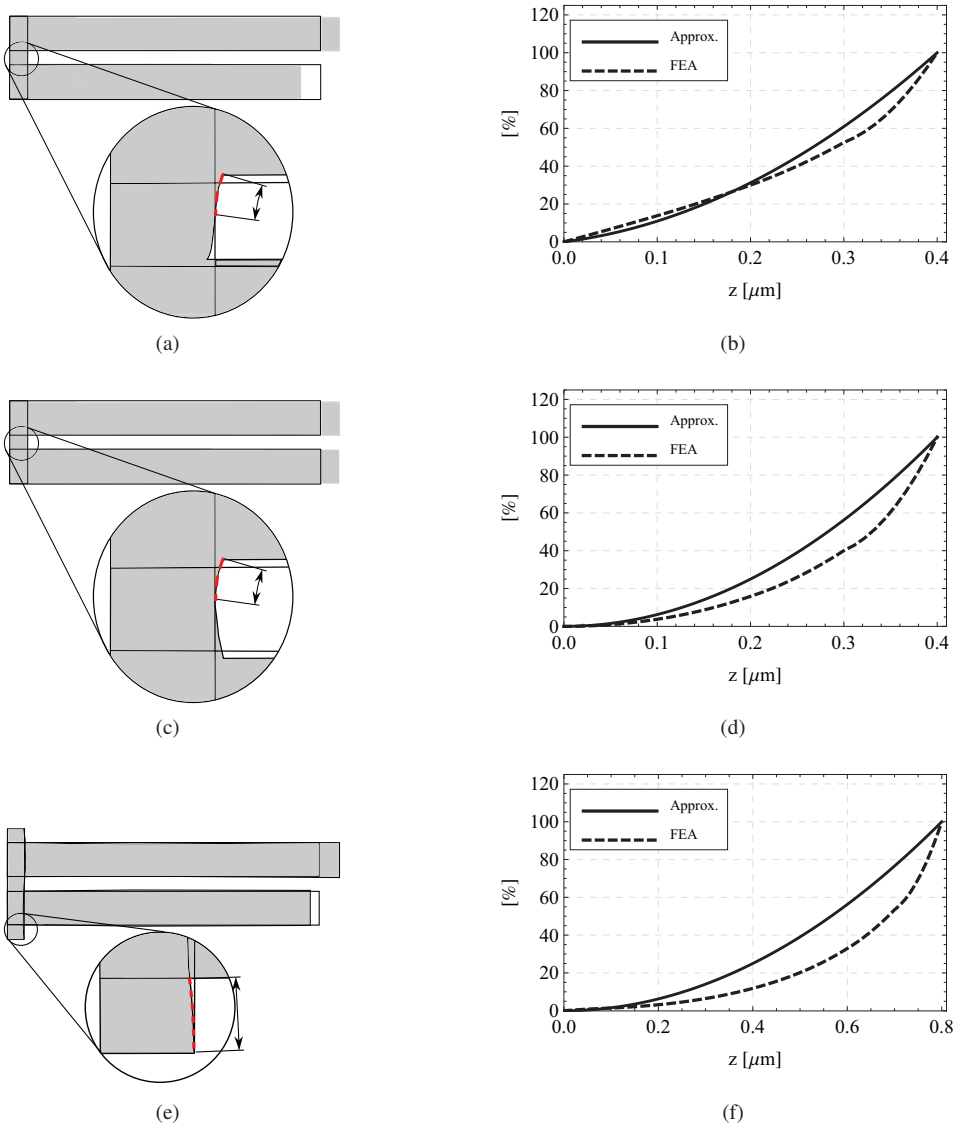

Figure 2.12: Radial displacement profiles were extracted from FEA for the inter-disk stem section from a dumbbell and the bottom stem for the full system. (a), (c) and (e) indicate location of path from where data was extracted. Figures (b), (d) and (f) and show the approximating functions and normalized data extracted from FEA. Both the inter-disk and bottom stems are of 0.8 μm height.

and the corresponding profile extracted from FEA. Similar as for the inter-disk stem, figures 2.12(c) and 2.12(d) show from where the displacement profile for the bottom stem section of a full system is extracted, and the corresponding comparison of the approximate displacement profile (2.43) with that extracted from FEA.

2.6.2 Modal analysis of dumbbell

Figure 2.13 shows the frequency versus stem radius for two representative dual disk dumbbells. Figure 2.13(a) shows result for a disk of radius 20 μm and Aspect Ratio (AR)=9. While the model for the in-phase mode (2.30) closely follow the results from FEA to a stem radius of about than 1 μm, the model for the anti-phase mode (2.40) consistently overestimate the frequency. Figure 2.13(b) shows a similar plot for a dumbbell with disk radius of 24 μm and AR=9. Similar

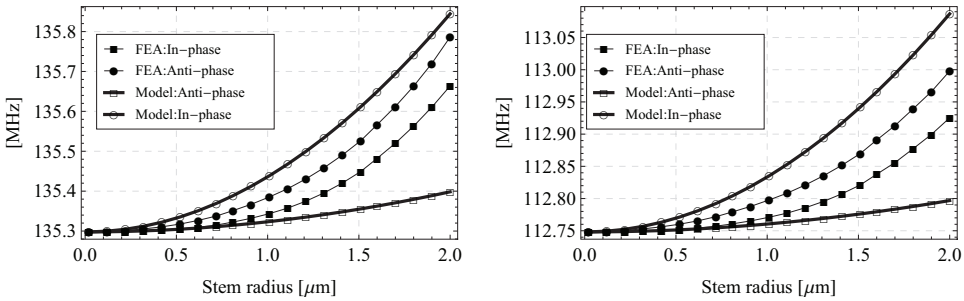

(a) (b)

Figure 2.13: Frequency versus stem radius for two dumbbells with disks of radius and AR (a) 20μm and 9 (b) 24 μm and 9

to as in Figure 2.13(a), the model for the in-phase mode follows the results from FEA closely up to a stem radius of about 1 μm from whereon it underestimates it. For the anti-phase mode, the frequency is once more consistently overestimated.

2.6.3 Modal analysis of full system

The results from the FEA are illustrated in figures 2.14(a) and 2.14(b) for two typical system of disk radii $20\mu m$ and $24\mu m$, respectively. The 3D plots show the frequency of the in-phase mode versus the disk aspect ratio AR and the stem radius. In Figure 2.14(a) an irregularity can be seen in the otherwise smooth behavior for ARs in the range 6 to 10. A similar behavior is seen in Figure 2.14(b) for ARs in the range 6 to 8. These are regions where spurious bending modes pass through the frequency range of the stacked disk resonators, causing a distortion of the mode shape as illustrated in Figure 2.15. A similar irregularity can be seen at low stem radii for AR=12 for all disk radii and also for AR=11 for disks of radius $18\mu m$ and $24\mu m$. However, for this range of ARs, a mode order inversion occurs at the irregularity, leaving the in-phase mode at a frequency lower than the anti-phase mode at the higher stem radii. Figure 2.16 shows parameter spaces where bending modes and mode order inversion will occur within the range of stem radii investigated.

Comparison of analytical and FEA results

Figures 2.17(a) and 2.17(b) show the dependence of the in-phase and the anti-phase mode frequencies on the stem radius for a system with disk radii of $20\mu m$ and $24\mu m$, respectively. For

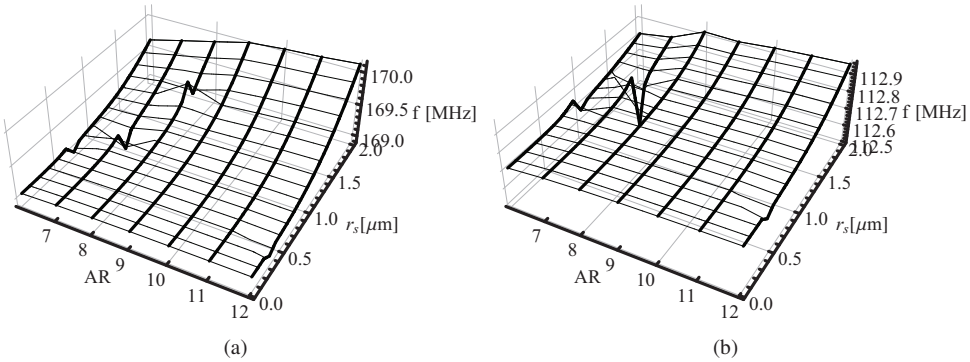

Figure 2.14: Frequency for highest frequency modes of a two disk systems versus the AR radius/thickness and stem radius. The disk radii are (a) $16\mu m$ and (b) $24\mu m$. Both surfaces indicate discontinuities, meaning that spurious modes interfere and distort the extensional modes.

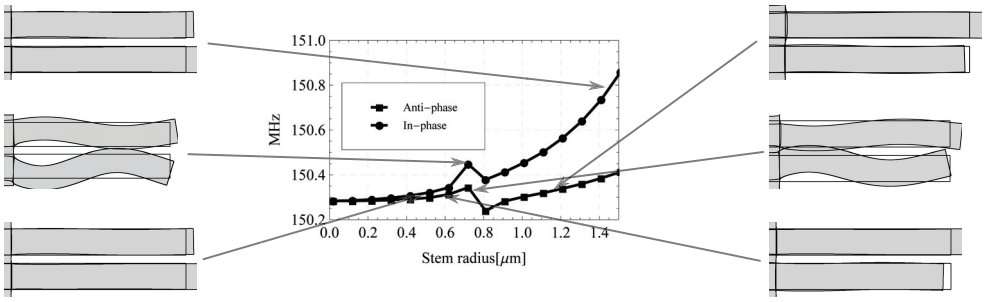

Figure 2.15: The modal shapes for the extracted frequencies for a system with disks of radius $18\mu m$. For stem radii below and above $1.1\mu m$, the mode shape is mainly extensional, while for stem radii near $1.1\mu m$, the mode shape is severely distorted.

the anti-phase mode, the stem radius where the model and FEA depart, increases with disk radius, from about $1\mu m$ for the smaller disks and closer to $1.25\mu m$ for the larger disks. In addition, it is also found that the radial amplitude of the top disk is larger than for the bottom disk and this difference increases with both stem and disk radius. Moreover, the center of the top disk is nearly at standstill while the bottom disk center moves up and down, causing bending to the disks. This effect increases with stem radius.

For the in-phase mode, the modal frequency is consistently overestimated. The center of the bottom disk is found to be nearly at rest, causing vertical motion of the center of the top disk, causing bending motion to be induced.

2.7 Discussion of model for the frequency separation

For small stem radii and ARs outside regions of mode reordering or distortion from bending modes (Figure 2.16), the model derived above reproduces the results from FEA quite well.

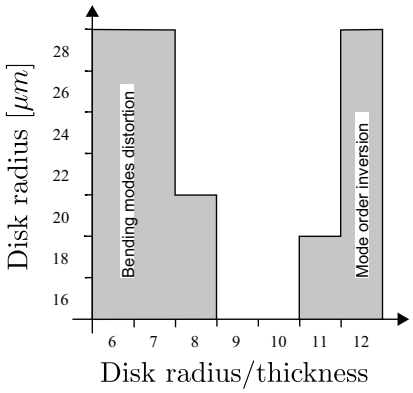

Figure 2.16: Summary of FEA results showing parameter combinations where bending modes or mode reordering will occur for certain stem radii.

However as the stem radius and the mode separation increase, the accuracy of the model gradually decreases. For large stem radii, the model for the anti-phase mode underestimate the modal frequency. This can be because the kinetic energy of the stem is calculated using the frequency of the disk, rather than the actual resonance frequency. With an iterative or recursive method, this should be possible to implement, although it might obscure the analytical clarity the model provides.

Another potential source of error is the approximating function used for calculating the kinetic energy, the equivalent masses of the stems and the frequency used for finding the corresponding stiffness. For the bottom stem the parameter η was determined by the boundary conditions, but for the inter-disk stem η was found to be between zero and four for the anti-phase mode. While $\eta = 0$ gives a linear approximation and $\eta = 4$ gives a second order approximation, FEA (Figure 2.12(b)) show that the deformation profile is somewhere between these two. As the aim of is to develop a simple model, an integer value was to be chosen for η. As it seems more parabolic than linear, $\eta = 3$ was used. For the in-phase mode the radial deformation at the center was assumed negligible. Depending on the height of the stem, this assumption will be erroneous, and a radial extension at the stem center will happen independent if the stem is compressed or extended.

For the in-phase mode, the frequency is consistently overestimated. Potential sources of error are the quasi static assumption taken and the corresponding models for stiffness and mass. The highest frequency system simulated operates at about 200 MHz, at which wavelengths in pSi is more than 40 μm, meaning more than 50 times the length of any of the stem sections and five times the length of the total system height for the largest disk with the lowest AR. This means that the quasi static model for each stem section should be valid, but that there might be some difference in phase vertically in the full height of the stack. However, considering that the source of vertical motion is separated only by the length of the stems and two times half the disk thickness, the quasi static approximation seems even more reasonable. However, the

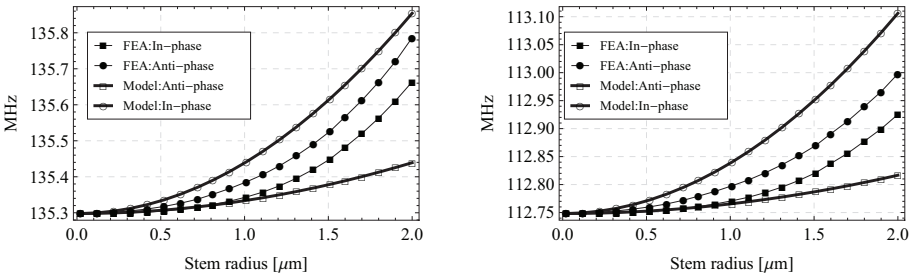

(a) (b)

Figure 2.17: (a) For the $20\mu m$ disk the analytic model follow the FEA results closely up to a stem radius of about $1.25\mu m$ for the in-phase mode while it is consistently overestimated for the anti-phase mode. (b) The analytic model for a system with disks with $24\mu m$ radius follows the FEA results up to a stem radius of $1.25\mu m$ for the in-phase mode and consistently overestimate the frequency of the in-phase mode.

model used for the stiffness of the axial deformation of the stems are likely to not reflect the real stiffness of short bars with axial strain. The model used is based on the assumption of uniform strain throughout the major length of the bar, an assumption which becomes invalid when its radius is the same order as the stem height. As no good model for such short bars has been found in the literature, the best available model has been used.
Other potential reasons for the deviations in reproducing the exact modal frequencies can be interaction with nearby modes, e.i. disk-stem interactions not accounted for by the analytical model and inertial forces generated by the vertical motion of the disk centers.

From the results and discussions presented in the sections above, an improvement to the design illustrated in Figure 2.4, would be to clamp the top hat by anchoring it to the substrate as indicated in Figure 2.18, resulting in the stem section being clamped at both ends. This would reduce the difference in disk amplitude and reduce the vertical motion transferring energy to nearby bending modes. This would not only increase the range of stem radii for which a fabricated device would be useful (due to the reduction in bending mode energy), but also decrease the difference between the model presented here and the results from FEA, yielding a more predictable design.

Discontinuities in the modal frequencies extracted from FEA can be found in figures 2.14(a) and 2.14(b) for systems with disks of low ARs. These discontinuities are regions where the radial extensional modes are distorted into bending modes as illustrated in Figure 2.15. For small disk radii and high AR, similar discontinuities can be found. These discontinuities result from mode reordering, meaning that the relative additional stiffness of the radial deformation of the stem is greater than that from the vertical deformation. These phenomenas are not included in the analytical model but are important to avoid when designing a device for fabrication. Hence parameter maps like Figure 2.16 are of great importance.
Nonetheless, the present model and its derivation provide useful insight into the effects govern-

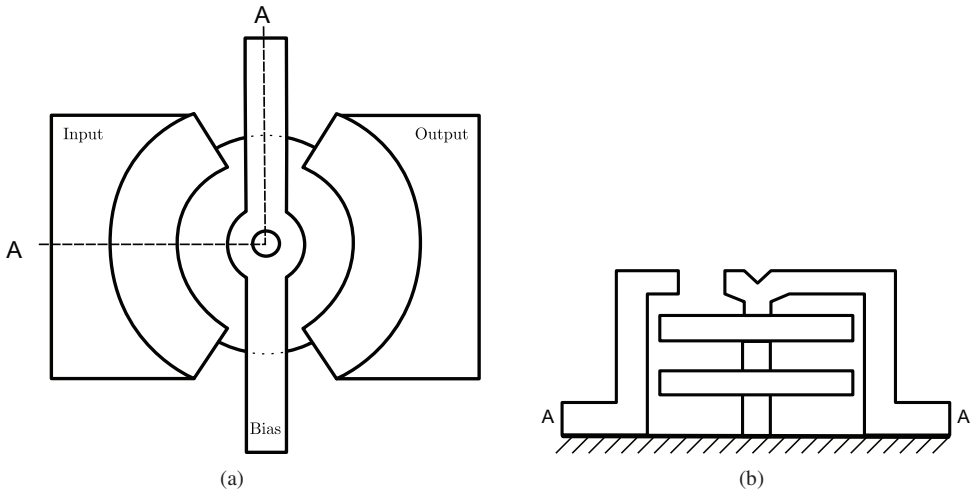

Figure 2.18: (a) Top view and (b) cross section view along A-A of suggested design to reduce vertical bending motion by clamping both ens of the center stem.

ing the frequency separation in stacked disk resonator systems.

2.7.1 Higher order modes

Higher order extensional contour modes have been demonstrated in disk resonators in [2]. The model presented above is based on the assumption that the distance between the substrate and the bottom disk as well as between the two disks is about an order of magnitude less than that of the acoustic wavelength. For pSi systems with the present dimensions, this corresponds to frequencies less than 1 GHz. For frequencies within this range, the assumption should be valid, and only the frequency scalar κ will need to be changed to encompass higher order modes [2, 102]. It is worth noticing that the single disk system in [2] with a disk radius of 10 μm operates at 274 MHz, 734 MHz and 1.15 GHz in the first, second and third mode respectively. Hence the quasi static approximation should be valid for the two lower modes, and even for higher order modes for systems with larger disks.

2.7.2 Evaluation of the accuracy of the simulation results

It is important to focus on the trustworthiness of the FEA when using it for validation of the analytic model. As stated in subsection 1.4.2, a main principle of FEA is that one can obtain a solution over a finite domain of a system and as this domain is sectioned into smaller subdomains, the accuracy of the the solution should converge towards the continuum solution. This is commonly acknowledged and presented in numerous textbooks on FEA [55]. Methods for extracting estimates of the error exist [103]. Such methods are mainly relevant when systems of large displacement are simulated.
As the simulations presented in section 2.5 were run with a number of elements exceeding what

was required to achieve convergence (ref. subsection 1.4.2), and only a basic modal analysis was required to extract the resonant frequencies, the solution obtained from the FEA can be assumed to be correct from a computational point of view.
However, as with all modeling methods, the model only reflects what has been put into it. When comparing FEA with experimental results, there are numerous uncertainties in the input to the FEA: material parameters, physical dimensions and non-ideal boundary conditions. However in the work presented here, two idealized implementations of the same structure have been compared. Hence the basis for the two models is the same, and their coinciding results therefore serve as verification that the main coupling effects of the system is described by the model.

2.7.3 Further modeling work

To improve the model further, inertial forces should be accounted for. This can be done by using the expressions derived here, inserting them into the equations of motion and casting the system into an equivalent circuit as described in subsection 2.4.6. The equivalent circuit can easily be implemented in circuit simulators such as SPICE to allow rapid simulations. It must be noted that such a model would include the first order effects of the inertial forces, but not the forces resulting from the bending modes of the disks, enhanced by the vertical motion.
This work has been initiated by one of my coauthors in [18], and is left for him or others to finish.

2.8 Fabrication

This section is divided into three subsections. In the first subsection, an extended version of the process described in [2] is outlined. This process sequence was developed and partially performed at SINTEF MiNaLab. As will be made clear, these trials were unsuccessful in fabricating a working device.

The second subsection outlines an alternative process based on Double layered Silicon On Insulator (DSOI) where initial trials was performed during a three month stay at University of California in 2009. The last subsection summarizes what has been learned and makes an effort to describe a geometry avoiding some of the problems experienced.

2.8.1 Surface micromachined stacked disk resonators

In [83], the first micromachined disk resonator was presented. One major problem identified with the process used, was that the stem and disk were defined on separate mask layers. As the nodal point of a disk vibrating in radial contour mode is in the center, a mask misalignment gave an off-center stem, resulting in distorted mode shapes and hence a reduction in Q-factor. The problem was addressed and solved in [2]. Using one mask for defining both the disk's dimension and location of the center hole, a self aligning process was achieved. The process described below, extends this process by adding one additional structural layer and one sacrificial layer.

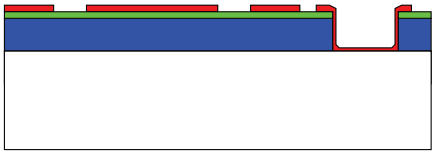

(a) A standard wafer is thermally oxidized and Si_4N_3 is deposited before contact holes are etched using a combination of wet and dry etches. A thin layer of pSi is then deposited and patterned to form bottom leads for signals and biasing.

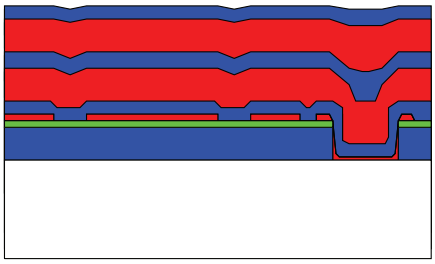

(b) A stack of SiO_2 and poly-Si layers are then deposited.

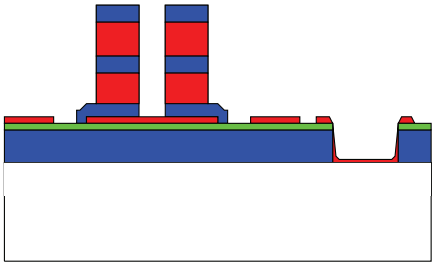

(c) DRIE is then used to etch through the sequence of layers, terminating against the oxide.

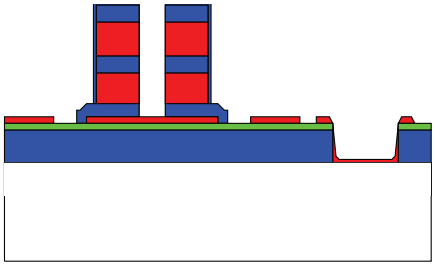

(d) After a short thermal oxidation to form the electrode gap, oxide is then removed from the center hole and areas away from the layer stack.

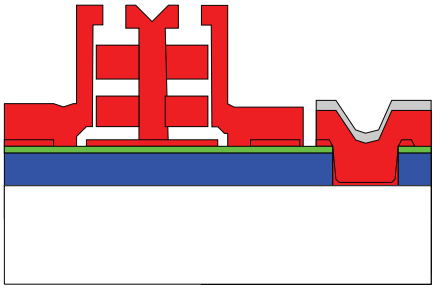

(e) A poly-Si layer then caps the layer stack, is patterned and etched with DRIE before exposed oxide is removed with HF-vapor.

Figure 2.19: Outline of SMM process for making stacked disk resonators

Figure 2.19 shows an outline of the SMM process. Starting with a regular (100) wafer, a thick ($2\mu m$) thermal oxide is grown before 300 nm Si_4N_3 is deposited using PCVD. Both layers are then etched with DRIE to allow openings for electrical contact to the substrate (Figure 2.19(a)). A 550 nm layer of pSi is then deposited, implanted, patterned and etched to form leads for biasing the disks. Through a sequence of depositions of pSi and thermal oxidations, three sacrificial layers and two structural layers are formed (Figure 2.19(b)). The thermal oxidation is used instead of PCVD oxide as initial trials showed that the process available, failed to form well defined oxide layers. Its use requires that the underlying pSi layer is somewhat thicker than what one would like to have. This comes from the fact that during thermal oxidation, about 44 percent of the final thickness of the thermal oxide, comes from consuming the pSi [34]. Two oxide and two pSi layers are then etched with DRIE before a thermal oxidation is used to form about 100 nm oxide on exposed pSi. A thick layer of photresist is deployed using a standard process that would give $8\mu m$ resist on a flat wafer. The actual thickness will vary over the wafer depending on local topography. A separate mask is used to open it up in the center of the disk. Oxide is then removed inside the center hole and areas away from the disks (Figure 2.19(c)). The complete system is then capped with a new layer of pSi and aluminum for the bondpads is sputtered. The aluminum is then patterned and etched before the last pSi layer is patterned and etched with DRIE to make individual electrodes. The final step is to remove exposed oxide using HF vapor phase etching.

Processing results

The process outlined above and in Figure 2.19 was started at SINTEF MiNaLab, in Oslo, Norway. Detailed plans for all steps were made together with the laboratory staff, which also performed all fabrication steps.

Although the process described above makes use of standard processes, problems appeared during processing, some of which turned out to be insurmountable with the time and funds available. While the initial plan was to use PCVD to deposit not only the pSi, but also the oxide, it turned out that the Low pressure Plasma assisted Chemical Vapor Deposition (LPCVD) deposited oxide was permeable to the silane gas used during deposition of pSi. Hence, pSi formed inside the oxide and it was not possible to have distinct separation between the the sacrificial layers and structural layers. The problem was solved by using thermal-oxidation. For each of the oxide layers in Figure 2.19(b), a layer of pSi was deposited on top of the already existing pSi. When silicon is thermally oxidized, about 44% of the final thickness of the oxide will be from the oxidized silicon [34]. Hence it was possible to obtain a high quality oxide which offered good separation from the pSi layer deposited next, as seen in the SEM micrograph in Figure 2.20. Early in the process, the removal of oxide in the center hole after the thermal oxidation of the 100 nm gap oxide was identified as challenging. The problem was mainly that it would be hard to use DRIE with good anisotropy inside the hole because of its small dimensions ($r \leq 3\mu m$). Also, it would be hard to confirm that all the oxide was removed at the bottom of the hole. The plan was therefore to use a combination of DRIE and HF vapor. Since thermal oxide was used for the sacrificial layer rather than PCVD oxide, the problem with oxide in the center hole, was enhanced further as the thermal oxide is dense and etch rates are

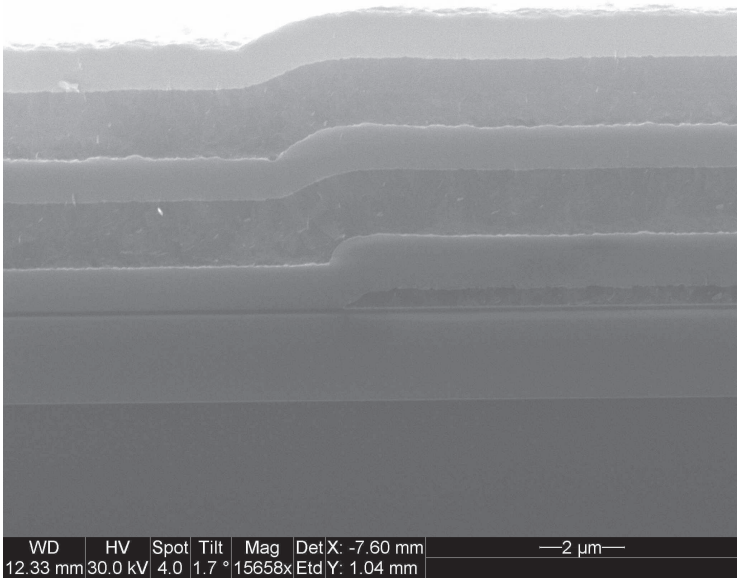

Figure 2.20: A SEM micrograph showing the cross section after the disk layers and sacrificial oxide layer was deposited using the back-oxidation technique.

lower than for PCVD oxides. Figure 2.21(a) show the state of a disk stack after trying to remove the oxide in the hole using HF vapor etching. The photoresist detached from the wafer surface, an oxide underneath the bottom disk was etched. The corresponding results inside the center hole is depicted in Figure 2.21(b).

2.8.2 Bulk micromachined disk resonators

One problem with the SMM resonators, and in particular for use as filters, is that their electrode areas are small due to the thin structural layers. This means that the impedance of the device is in the order of kOhm rather than the desired 50 Ohm as commonly used for transmission lines. One possibility to reduce the impedance of disk resonators is to increase the active electrode area of the disk. For a given system at a given frequency, this can be achieved by increasing the disk thickness. In Figure 2.22 a process based on DSOI wafers with two $10\mu m$ thick device layers and two $2\mu m$ Buried OXide layer (BOX) layers is described and presented as an alternative manufacturing process.

Fabrication results

With the help of lab engineer Matthew Wasilik at Berkeley Sensor and Actuator Center (BSAC), DSOI wafers were processed according to the process outlined in Figure 2.22. Nitride and oxide were deposited and patterned before the DRIE. Since DSOI wafers are not commercially

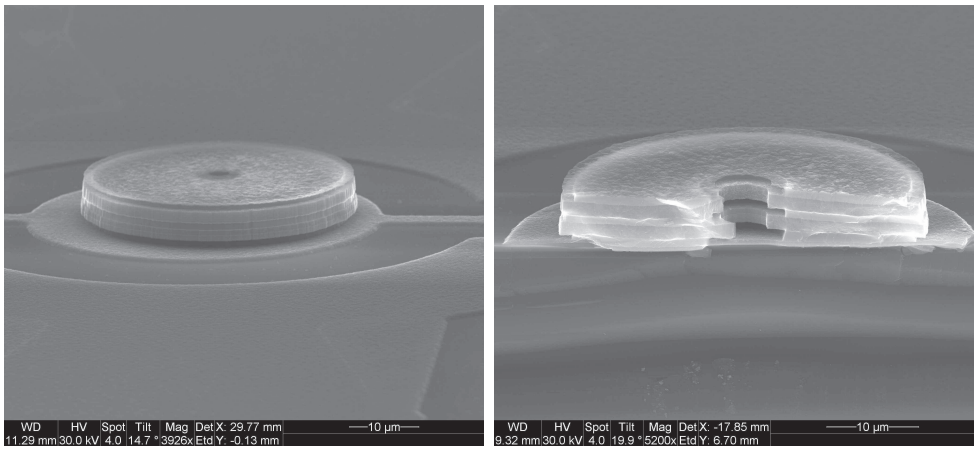

(a) (b)

Figure 2.21: (a) SEM micrograph of a disk after DRIE and a short vapor phase HF etching. (b) Corresponding cross section showing how the oxide in the center hole has been overetched. Images courtesy of Jon.D. Hansen, SINTEF, MiNaLab.

available, 100 mm custom wafers from Ultrasil[104] were used. Both device layers were $10 \pm 0.5\mu m$ thick, and the BOX layers were both $2\mu m$ thick and made from thermally grown oxide. All silicon layers were p-type (Boron) doped. The device layers had a resistivity of 0.005 to 0.020 Ohm cm and the handle wafer 1-30 Ohm cm. Total wafer thickness was 424 μm.

All wafers were RCA cleaned before a low stress high temperature nitride was deposited and measured to 277 nm thickness. Low temperature oxide was then deposited with LPCVD to a thickness of 720 nm before the resist was spun on and patterned. Since the available DRIE equipment, a Centura MPX, was configured only for 6 inch wafers, the 100mm DSOI wafers had to be bonded to 6 inch wafers before etching. Two schemes were tested: photoresist and thermal paste. The thermal paste offers better heat conductivity than photoresist and thereby offers better process control than photoresist. However due to particles in the paste of about the same size as the desired structures, it could potentially cause problems with the structures after release from the carrier wafer. Hence was both alternatives used for the trials.

All layers were etched with in the same DRIE setup, using predefined recipes for each of the layers. Each of the recipes were configured to minimize underetching, avoid scalloping, and minimize footing[1] effects [105] were applicable.

Wafers bonded with photoresist

To attach the 100 mm DSOI wafer to the 6 inch handle wafer using photoresist, the six inch wafer was covered with resist using an automated spinner with Edge Bead Removal (EBR) and the DSOI wafer positioned manually in the center. The assembly was then baked on a hotplate

[1]Footing is a nonideal effect of charge build up in the BOX layer when etching SOI wafers using DRIE.

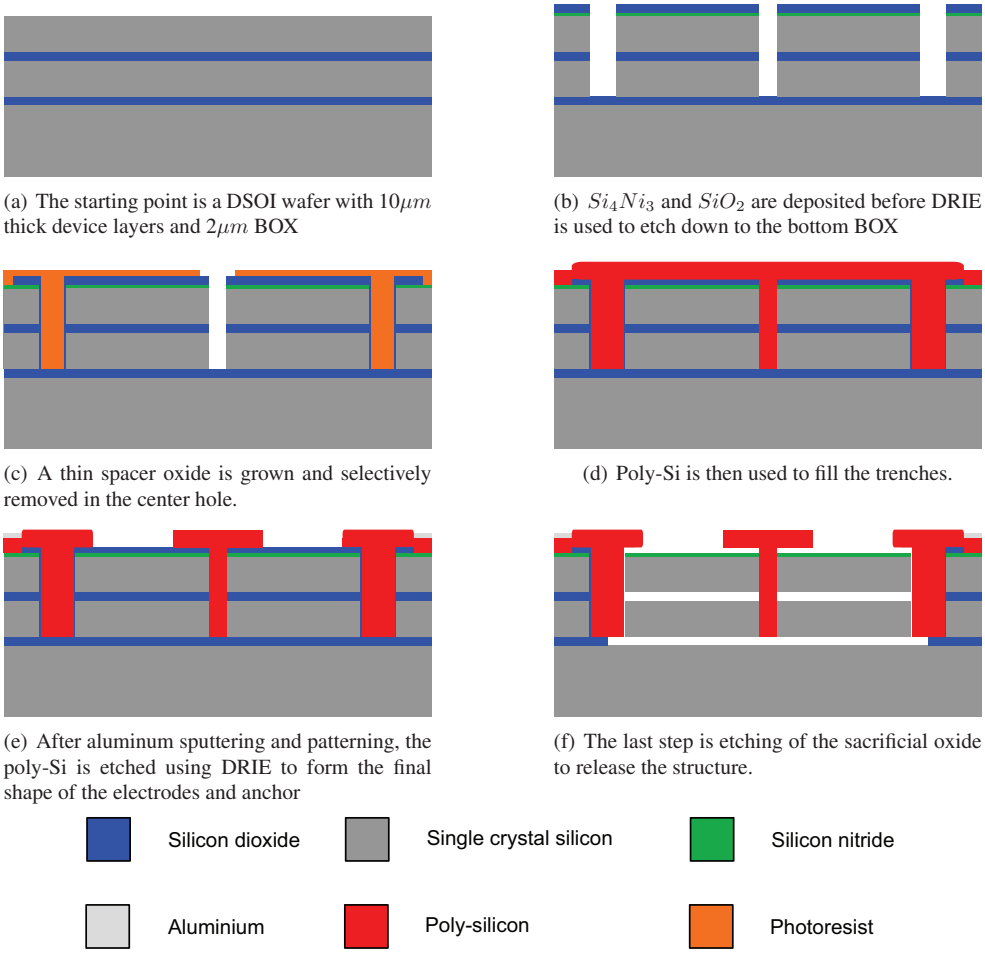

(a) The starting point is a DSOI wafer with $10\mu m$ thick device layers and $2\mu m$ BOX

(b) Si_4Ni_3 and SiO_2 are deposited before DRIE is used to etch down to the bottom BOX

(c) A thin spacer oxide is grown and selectively removed in the center hole.

(d) Poly-Si is then used to fill the trenches.

(e) After aluminum sputtering and patterning, the poly-Si is etched using DRIE to form the final shape of the electrodes and anchor

(f) The last step is etching of the sacrificial oxide to release the structure.

Figure 2.22: Process outline of DSOI based process.

for 4 min before the EBR regions and sides of the DSOI wafer were manually covered with resist. A final baking on a hot plate was then done before the wafer was etched.

The etch progress of the different layers was monitored using a microscope and a profilometer. First operation was a 163 second etch through the oxide layer. The wafer was then visually inspected and the etch-through was (wrongfully) confirmed with the profilometer. This was followed by a nitride etch which had to be done in multiple steps as perforation of the nitride could not be verified after the initial 150 second etch. An additional 30 second nitride etch with no change in status motivated a 40 second oxide etch to ensure that all the oxide was removed, before 7 times 30 second nitride etches were required before all the nitride was etched through. The first device layer was then etched in two steps of 121 and 44 second, separated by a visual inspection. It is worth noticing that based on experience with regular Silicon On Insulator (SOI) wafers, the first 121 second etch was expected to etch completely through the

first device layer. At this point, the resist was starting to be depleted at the perimeter of the wafer, which meant that any successful devices would be in the center of the wafer. The first BOX layer was then etched using a sequence of oxide etches of 189, 180, 60, 60, 60, 60 and 60 seconds. For each step, the wafers were removed from the chamber and inspected optically and with a profilometer. Based on the achieved etch rate for the top device layer, a final step of 176 seconds was used to etch the bottom device layer. The wafer was then stripped for resist and cleaned before being characterized in a SEM. Figure 2.23(a) shows a cross section from a test structure of straight lines with similar line width as an ideal disk cross section, meaning that the mask features corresponding to the $6\mu m$ and $10\mu m$ openings seen, were $3\mu m$ and $5\mu m$, respectively, on the mask. Clearly the etch did not result in the desired cross section. The top

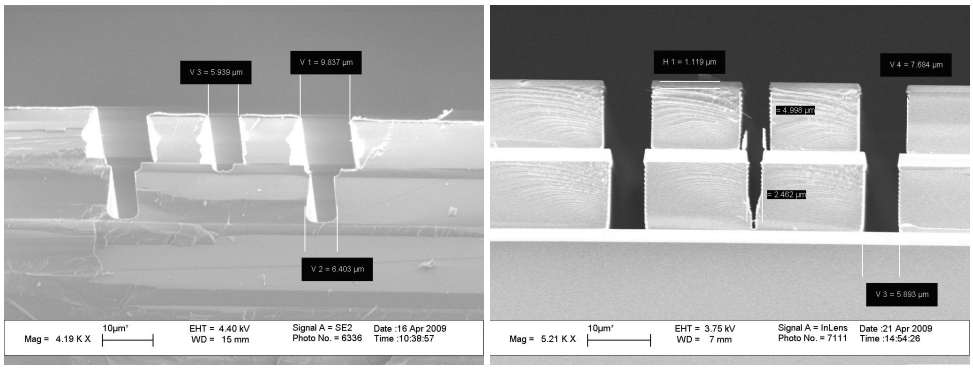

(a) (b)

Figure 2.23: SEM micrographs showing cross sections of trenches in DSOI wafers etched using DRIE. (a) shows structures from a wafer attached to a carrier wafer with photoresist while (b) shows similar structures from a wafer attached to a carrier wafer using thermal paste.

device layer was severely etched sideways in a nonuniform matter and the first BOX layer was not uniformly etched in the center trench and the two neighboring trenches. In addition, the bottom device layer was not completely etched through.

Explaining these undesired results based on only one wafer is difficult, but a brief discussion is in place. The lateral etching of the top device layer most likely happened during etching of the bottom device layer. This can be argued based on the dimensions of the BOX layer openings whose opening is significantly smaller than the width of the trenches at the bottom of the top device layer. When looking at the unsuccessful etch through of the BOX in the center trench, the etch rate of the BOX layer is apparently affected by the width of the opening. For the bottom device layer, the duration of the etching was 50% longer than what would be expected for single layer SOI wafers.

Wafers bonded with thermal paste

To attach the 100 mm DSOI wafer to the 6 inch carrier wafer Cool Grease thermal conductive paste [106] was used. A thin layer of paste was distributed in the center to a radius slightly larger

than 100 mm. The DSOI wafer was then manually positioned in the center and the excess paste removed with a solvent. The rest of the carrier wafer and the sides of the DSOI were manually covered with photoresist and baked. The oxide of the wafer bonded with thermal paste was then etched in multiple steps of 180, 30, 30 and 30 seconds before the oxide was confirmed to be completely removed with an optical microscope and a profilometer. The nitride layer was then etched in a sequence of 40, 20, 30 and 30 seconds.

The first device layer was then etched for 121, 55 and 44 seconds before the first BOX layer was etched for 180, 180, 60, 120 and 120 seconds. The final etching step was a 220 second etch through the bottom device layer. The wafer was then simultaneously released from the carrier wafer and stripped for photoresist in an acetone bath, before characterization in the SEM. As for the wafer attached with photoresist, a cross section of straight lines of width similar to an ideal cross section of a disk is shown in Figure 2.23(b). The sidewalls are nearly straight and the difference in the width of the trenches in the two device layers are less than in Figure 2.23(a). The etch rate of the center hole was somewhat lower than in the wider trenches. Also, the trench in the bottom device layer is tapered and not completely etched. A strange artifact are the two *pillars* in the center hole at the BOX layer.

2.8.3 Discussion

Two different approaches for processing stacked double disk resonators have been investigated. In the first process sequence, an SMM process, it proved difficult to fabricate the devices due to the small dimensions and depth of the center holes. The removal of oxide inside these holes resulted in significant overetching, which according to FEA would render the devices useless for model verification as the stem diameter would be outside the useful range of the model derived. However, as it became apparent that the fabrication would be unsuccessful, it was also realized that the whole system could have been suspended from the top to reduce the problems. Not only would it simplify the fabrication process by lessening the problem of removing the oxide in the center hole, but also by removing the need for a pSi layer. The suggested structure is illustrated in Figure 2.24. In the second process, which addresses some of the challenges uncovered early in the work with the first process, novel double layered SOI wafers were used. This process would result in a structure similar to that seen in Figure 2.24. For the wafers bonded to the carrier wafer using photoresist and thermal paste, the etch rates of both the silicon and oxide was slower than expected. One possible explanation for this can be an increased temperature of the substrate due to a thermal barrier caused by the top BOX layer.

Although the experiment with the DSOI wafer attached to the carrier wafer using thermal paste produced promising results, the difference in dimensions between the two device layers must be minimized if DSOI wafers are to be used to fabricate stacked disk resonators. In addition, the test structures used whose cross section is illustrated in Figure 2.23, are not representative for the actual structure as their dimensions are comparable to a cross section through the disks center only in one in-plane direction. This highlights that even if the process can be tuned to give acceptable results for the cross sections shown, it is likely that the process would need further tuning before acceptable results can be achieved also for the real device.

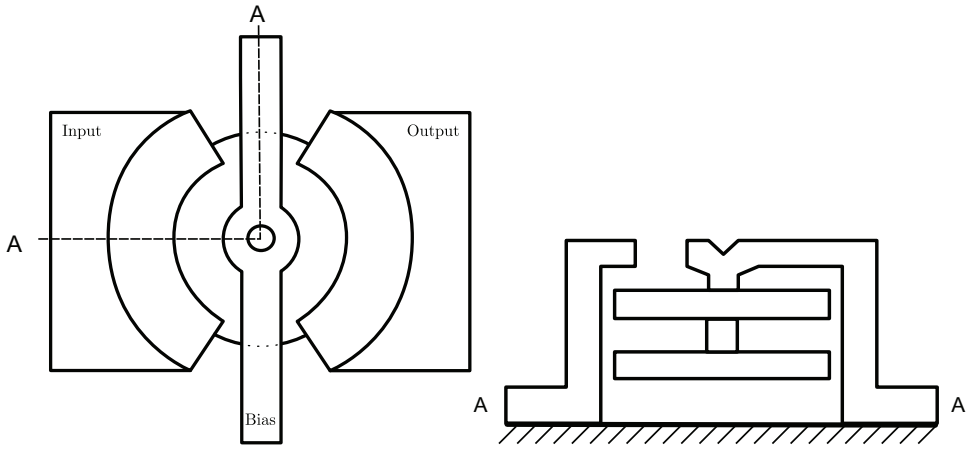

Figure 2.24: Suggested structure utilizing top side suspension and thereby avoiding the difficult removal of oxide at the bottom of the material stack prior to the small diameter hole refill.

The work presented was performed over a three month stay at BSAC, and has been put on hold until funding for further trials can be established. Time did not allow a proper failure analysis and the process optimization that was needed to fabricate functional devices.

To the author's knowledge, no work focusing on fabricating MEMS from DSOI wafers has been reported in the literature. It is therefore highly desirable to continue work on this, both from an academic point of view and for making stacked disk resonators.

2.9 Summary

In this part, a lumped model for the frequency separation of a dual disk stacked disk resonator system and two fabrication trials were presented. Although the model is useful for calculating the frequency separation in such resonator systems, more importantly, it provides insight into what geometric features affect the frequency separation. This is important when evaluating the viability of coupling two or more disk resonators vertically. It is also useful for understanding which process steps deserve the most effort when optimizing the process to minimize process variations. The work presented in this part does not present results from fabricated and tested devices. This is unfortunate as the fabrication process itself is more likely to be the limiting factor in novel micro-system devices, than the modeling and understanding of the device itself. Although processing techniques have evolved over the duration of this work, microsystem design is still strongly dependent on process development, even when standardized processes are used.

Chapter 3

Modeling of support losses

3.1 Motivation

One of the key performance indicators for resonators, is the Q-factor. It reflects the selectivity, frequency stability and energy losses of the complete system. When resonators are coupled to form a filter, their individual Q-factor determines the flatness of the filter. While there are many ways to calculate Q-factor, one expression is particularly useful for the discussion below

$$Q = \frac{W}{\Delta W} \tag{3.1}$$

where W is the energy contained in the device and ΔW is the energy dissipated per cycle. The energy W can be found by integrating the displacement velocity over the volume and mass of the system (1.2) while energy dissipation must be found for each relevant loss mechanism and summed. Hence is

$$\frac{1}{Q_{tot}} = \sum_{i}^{n} \frac{1}{Q_i} \tag{3.2}$$

where Q_i is the partial contribution to the total Q-factor from the i'th loss mechanism. Loss mechanisms commonly discussed with respect to microsystems are thermoelastic damping [107, 108, 109], squeeze- and slide film damping [110, 111, 112], and support losses [113, 114, 3]. While gas damping can be made negligible through low pressure packaging, and thermoelastic losses are only significant for bending mode resonators, support loss has been identified as the main loss mechanism for disk resonators [3].

3.2 Modeling approaches for support losses

Support loss in micromachined resonators are due to energy radiating from the resonators point of attachment to the substrate and into the relative infinite bulk of the substrate. Although intrinsic material losses are small in SCS, the small interface area of the attachment effectively means the radiated energy is reverberated in the substrate until absorbed or lost through energy radiating from the substrate and into its surroundings, rather than radiated back into the resonator.

To estimate the energy radiated from the anchor points, methods adopted from the soil-structure modeling community has been adapted. The main problem is the infinite size of the substrate relative to the structure itself. The solution to this is the use of semi-infinite half spaces. Models for such semi-infinite half spaces were established for point loads more than 50 years ago for isotropic materials [115], and has later been extended to multilayered- [116] and anisotropic half spaces [117]. A full review of this topic is outside the scope of this text, but can be found in [118].

In the same review, two approaches are highlighted in particular as complementary useful for this purpose: FEA including its sibling, the Boundary Element Method (BEM) and lumped modeling.

FEA of support losses in micromachined resonators have been addressed through the development, implementation and use of PMLs in [59, 119, 120, 121].

With respect to analytical expressions and lumped modeling, the half-space models developed in the classical papers [122, 123, 115, 124], have been adopted specifically for micromachined resonators in [114, 3] and shown to reproduce experimental results with reasonable accuracy. However their complexity obscures insight to the loss mechanism itself through the use of extensive numeric schemes.

Here a simpler model based on lumped modeling of structure soil interaction is investigated. The model for the semi-infinite half space is well established and published in textbooks such as [7]. The aim is to develop analytical expressions to estimate support losses through the use of simple SMD systems, which in term can easily be transformed into equivalent circuit models for use in system level simulations. To evaluate the model developed, results from FEA and the literature, are used.

3.3 Background theory

3.3.1 Lumped models for semi-infinite half spaces

In [6] a strength of materials approach for modeling soil-structure interaction is presented. The method is equivalent to what is used when deriving the Euler beam equations. Here, only a brief review will be presented and the reader is referred to [125, 6, 126, 7, 127] for detailed presentations. As a starting point for the lumped parameter model for a semi infinite half space, a half space subject to a harmonic vertical load $P(t)$ uniform over a circular area A is considered.

$$P(t) = P_0(\omega)Exp(\mathrm{i}\omega t) \tag{3.3}$$

where P_0 is the complex amplitude of the load, ω the radian frequency of the applied load and t is time. Due the harmonic loading, three kinds of waves will propagate into the half space: dilatational waves, shear waves and Rayleigh waves. Each type will be present in different volumes of the semi-infinite half space as illustrated in Figure 3.1.

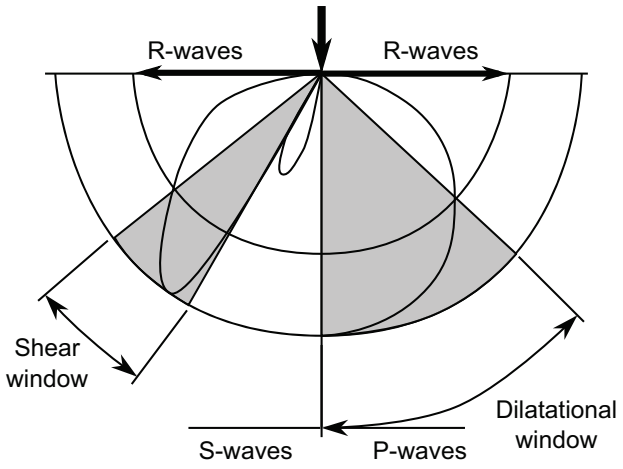

Figure 3.1: The three different wave propagation modes are confined to various regions of a semi infinite half space. The lobes indicate relative displacement magnitudes. The Rayleigh waves propagate along the surface and diminish rapidly with depth. The shear waves are only present in a very small angular opening while the dilatational waves propagate in a cone about the vertical axis. Figure reproduced from [6]

Rayleigh waves are also known as surface acoustic waves and are confined to a layer under the surface of about one wavelength in thickness. For point loads, the Rayleigh waves will account for the major part of energy radiating into the bulk [115].

On the other hand, dilatational waves, also known as pressure waves, propagate downwards in a cornet shape confined by a region of shear forces (Figure 3.1). This cone of dilatational waves forms the basis of the model, and as will be argued below, is capable of accounting for radiation losses from harmonic surface loads. As illustrated in Figure 3.2, the area A(z) of the cross section of the cone, is a function of distance from the cone apex(z=0). It can be expressed as

$$A(z) = \left(\frac{z}{z_0}\right)^2 A_0 \tag{3.4}$$

where the height z_0 will be determined later. Assuming that the strains from the p-waves are axial to the cone axis, which is equivalent to the assumption 'plane sections remains plane', used when deriving the commonly used linear beam equations, the displacement $u(t,r)$ on does not have to account for changes in strain as a function of radial coordinate and the amplitude can be expressed on complex form as

$$u(t) \;=\; u(\omega)e^{\mathrm{i}\omega t} \tag{3.5}$$

Consider a disk of thickness dz subject to normal forces N and $N+\partial N/\partial z\ dz$ where $\partial N/\partial z\ dz$ is the additional force due to the load-rate. Equilibrium of forces now require

$$-N(z,\omega) + N(z,\omega) + \frac{\partial N(z,\omega)}{\partial z}dz + \omega^2 A(z)\rho\ dz\ u(z,\omega) = 0 \tag{3.6}$$

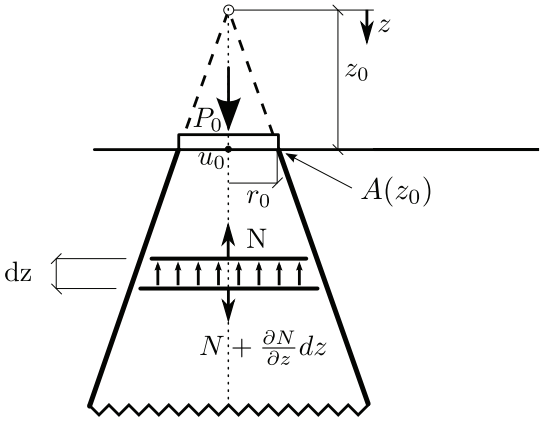

Figure 3.2: Reproduced cone graphics from [7] showing the parameters used for deriving a model for support losses from harmonic normal loads to an semi-infinite half space.

From the force-displacement relationship we have

$$N(z,\omega) = \rho c_p^2 A(z) \frac{\partial u(z,\omega)}{\partial z} \tag{3.7}$$

where c_p is the wave propagation speed of the pressure wave. Combining (3.4), (3.6) and (3.7), we get the one dimensional wave equation whose solution applies only when accounting for outwards propagating waves, and thus mimic the semi-infinity of the half space. For equilibrium at the surface, we now require that the surface force is equal to the normal force at $z = z_0$ from which we gain

$$u(z,\omega) = \frac{z_0}{z} e^{\imath \frac{\omega}{c_p}(z-z_0)} u_0(\omega) \tag{3.8}$$

The full calculation can be found in [7]. This gives the following expression for the pressure amplitude required to deform the surface a distance u_0

$$P_0(\omega) = S(\omega) u_0(\omega) \tag{3.9}$$

where $u_0(\omega) = u(z_0, \omega)$ and the dynamic stiffness coefficient $S(\omega)$ is

$$S(\omega) = K + \imath\omega C \tag{3.10}$$

The first term is called the static stiffness coefficient, which can be found to be

$$K = \frac{\rho c_p^2 \pi r_s^2}{z_0} \tag{3.11}$$

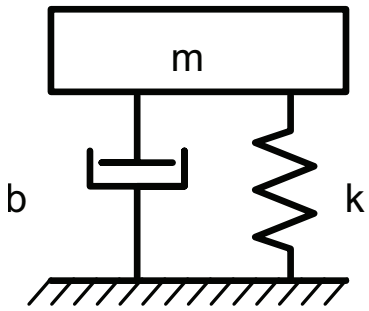

Figure 3.3: The properties of the cone model can be described as a system consisting of a spring, a dashpot and a mass.

The second term is the so-called dashpot coefficient

$$C = \rho c_p \pi r_s^2 \tag{3.12}$$

We can now assemble a SMD model of the cone as illustrated in Figure 3.3. For compressible materials in the range $\nu < 1/3$, energy will radiate from the interface at the surface, which can be described in the model by assuming the mass is zero. For materials with $\nu > 1/3$ a better model is achieved if one include the material confined by a trapped mass [7] which moves with the surface displacement if it was a cone pointing down into the substrate. Information on the case of nearly incompressible ($1/3 \leq \nu < 1/2$) and incompressible materials ($\nu = 1/2$) is not relevant for (100) SCS substrates and vertical loading, but can be found in [7].

With the exact stiffness expressed for a semi infinite half space as [6]

$$K_{exact} = \frac{4\rho {c_s}^2 r_0}{1-\nu} \tag{3.13}$$

where c_s is the shear wave propagation velocity. z_0 can now be found by equating (3.13) with (3.11), which gives

$$z_0 = \frac{\pi}{4}(1-\nu)\left(\frac{c_p}{c_s}\right)^2 r_0 \tag{3.14}$$

Effect of ignoring the Rayleigh- and shear waves

In [128] the division of power radiated into a semi infinite half space from a point load located at the surface, is calculated. About 2/3 of power is lost via Rayleigh waves while shear waves and dilatational waves account for 26% and 7 % respectively. Neither wave type is seemingly accounted for by the model presented above. One can therefore be lead to believe that the cone model is not capable of modeling the response of the semi infinite half space properly. In a paper dedicated to this issue [125], it is argued that the calculations presented in [128] are only correct for point loads. For footings of a finite size, one must consider the low and high

frequency limits separately. For high frequencies where the ratio

$$a_0 = \frac{r_s \omega}{c_s} \tag{3.15}$$

is higher than 3.5, the power lost through the Raleigh waves diminish as the frequency increase. The reason for this is that the Rayleigh waves propagate in a layer of about one wavelength in thickness. As the frequency increase the volume into which power can be lost, diminishes. For the low frequency end, the case is somewhat more complicated. The Rayleigh waves does not exist in the near field of the circular footing, only in regions greater than about half a wave length away from its center, a region termed the far field. In the near field, the unconceived Rayleigh waves have a behavior similar to the dilatational waves. Hence the energy that would usually be transmitted as Rayleigh waves will be treated as dilatational waves and all the energy accounted for by the loss in the cone. As the frequency increase, this assumption breaks down at about $a_0 = 2.9$, but at this point the perimeter area of the layer transmitting Rayleigh waves is sufficiently small so that the error done, is minimal. Any further increase in frequency, will reduce this perimeter area further, and the error decrease further. A complete discussion can be found in [125].

Assumption of isotropic properties for the bulk

One of the main points of resonators as modeled here is the potential for on-chip integration with CMOS circuitry. The substrates are most likely wafers of (100) SCS. SCS has a diamond atomic structure, meaning it is highly anisotropic. For a (100) silicon wafer, the surface is spanned by <100> directions. This means that the surface normal will also be a <100> direction, which has a Young's modulus of 130 GPa and a Poisson's ratio of 0.28 [1]. As is assumed, the waves propagating from the stem footing are plane and normal to the surface, the assumption of an isotropic substrate with material properties of the <100> directions is reasonable. To account for the anisotropic nature of the SCS substrate would complicate the model beyond the desired level of complexity for a simple analytic model.

3.4 Modeling outline

Before the model for the semi-infinite half space and the resonator is assembled, an analysis of the complete system is given as a foundation for the model expressions.

3.4.1 Motional and structural analysis

From section 2.4, it is clear that a symmetric radial deformation of a disk leads to a deformation over the thickness of the disk. For a disk resonator with a cross section as illustrated in Figure 3.4, it is clear that an axisymmetric radial extension of the disk, leads to vertical forces being generated. As the system's only point of attachment is the stem stub leading down to the substrate, forces and hence energy being lost via the support, must propagate through this section. In [3], a model translating the radial extension to normal surface forces on the interface with the bulk, was suggested. Taking into account process variations and a numerical correction factor,

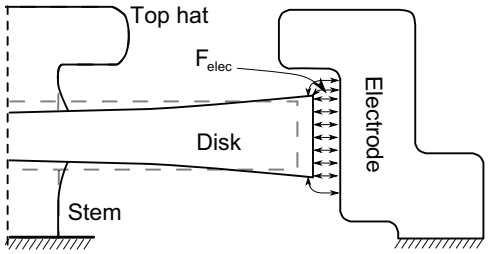

Figure 3.4: Cross section of disk resonator

the model presented spanned ranges for Q-factors which included values found from relevant examples in the literature. The model presented, assumed wave propagation through the stem, the disk center at standstill and a perfectly fixed stem base. This means that the displacement from the disk deformation was assumed to translate 1:1 to the top of the stem and that bulk deformations were not accounted for.

Not featured in the model presented [3], was the 'top hat', a residual structure from the fabrication process, which will generate inertial forces from the vertical motion induced by the disk deformation.

Typical planar surface micromachined layers are no more than $2\mu m$ thick. When used as a sacrificial layer separating the disk in Figure 3.4 from the substrate, the result is a short stem, and depending on material properties, it is of a length less than 1/8 of the wavelength for frequencies up to about 1 GHz for pSi and even higher frequencies for nanocrystaline diamond (ref. Figure 3.5). This means that the strain varies linearly over the length of the stem and that a quasi static model can be used when calculating forces from the stem to the substrate. With

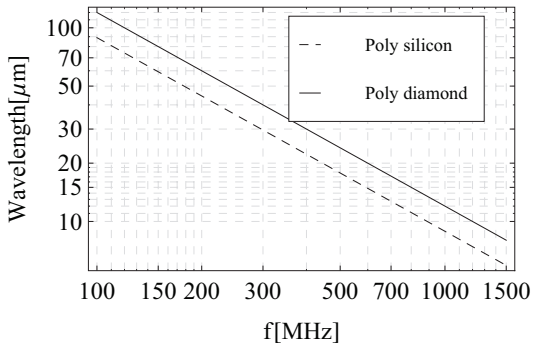

Figure 3.5: Acoustic wavelengths for diamond and pSi versus frequency

a disk attached to the substrate via the stem, a vertical deformation would have to be either a

vertical motion of the center of gravity of the disk, an elongation of the stem or a combination. Since the disks deforms symmetric about a plane in its center, its center of gravity is at rest if no other forces act on it. Such other forces can be either from the top hat or from the stem. The mass of the top hat is small compared to the mass of the disk and being short and thick, relatively, it will only generate inertial forces. Compared to the forces transferred between the disk and the bottom stem, the inertial forces are assumed negligible, and the top hat section not included in the model.

The mass of the bottom stem in motion by the deformation over the thickness of the disk, is even less than that of the top hat. Hence only the force from the deformation of the stem is of interest.

At the base of the stem, the vertical forces propagating from the stem-disk interface will be mainly transferred to the bulk as forces normal to the substrate. The forces will result in a displacement at the surface, effectively pumping energy into the substrate. The substrate, although of both finite thickness and lateral dimensions, is much larger than the stem footing, and a negligible amount of the energy reflected from the substrate boundaries will re-enter the disk resonator via the stem. Hence it reasonable to assume that all energy outbound from the stem is lost. The structure described in [2] and used as reference here, has multiple layers separating the stem base and the bulk of the substrate: a thin (350 Å) silicon nitride and a thick ($2\mu m$) silicon dioxide. Due to differences in material properties, each material transition represents a potentially reflecting boundary, however in [114], the effect of these reflecting boundaries as well as the backside boundary, is found to be negligible.

3.4.2 Model outline

In order to find a simple model for estimating the Q-factor of centrally supported disk resonators, the structure is divided into smaller and manageable substructures for which simple models can be found. The system is then reassembled and the analytic expressions evaluated and compared with results from the literature.

From the geometry of the device, it is natural to divide the structure into the following parts: disk, stem and substrate. For each part, a simple model reflecting their main contribution is sought. To find the interface forces between each section, which will govern the amount of energy transferred between the sections, the whole system is one-dimensionalized into a system of vertical forces. For the disk, this means finding the equivalent mass and stiffness for vertical motion at the stem interface. The stem, as outlined in subsection 2.4.1, can be considered short compared to the wavelength of the motion from the deformation of the disk, and hence be treated as a quasi-static member, meaning phase shifts over the length of the stem, are considered negligible. For the substrate, a simple model is adapted from the soil structure interaction community. The model mimics the behavior of an infinite half space by finding values for the components of a SMD system. Assuming that effects from the top-hat and material losses in the stem section are negligible, the partitioning of the structure and the resulting lumped model of equivalent springs, masses and dashpots, is illustrated in Figure 3.6. Although the top-hat is

not accounted for in the investigated model, it is included in the illustration for completeness. The disk is sectioned in two sets of springs (k_2 and k_3), dashpots (c_2 and c_3) and three masses

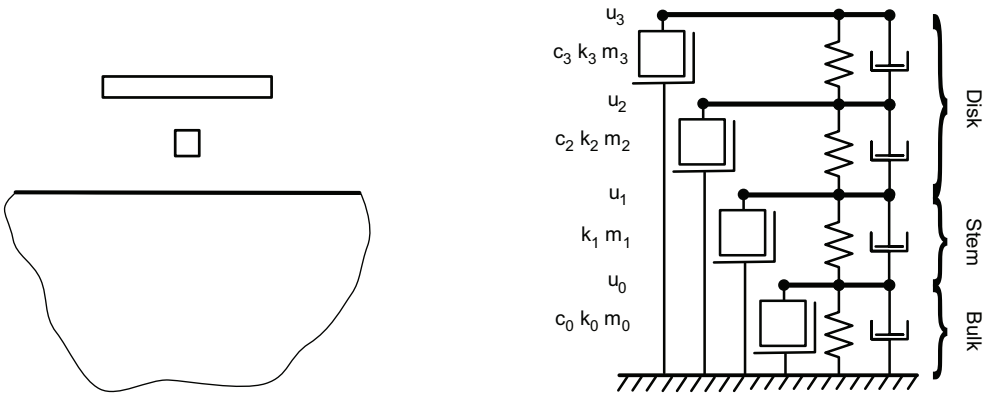

Figure 3.6: (a) The partitioning of the structure is done such that simple models for each component can be used. The substrate, support stem, and disk are considered as separate entities. (b) Models for each part is found separately based on their motion during operation of the resonator before the system is reassembled and interactions accounted for.

(m_1, m_2 and m_3) in order to reflect the symmetric deformation over the thickness of the disk. With respect to Figure 3.6, this means that one quarter of the disk's mass is assigned each of m_1 and m_3 while the remaining half is assigned to m_2. It is assumed that no vertical deformation of the top hat takes place, and it is therefore not accounted for in the model.

Force division

When contracting or expanding, the disk will generate vertical reaction forces at the interface at the top of the stem section, (k_1-c_1), in Figure 3.6(b). As a result of this, both the stem and substrate deforms, generating counter forces. This means that the effective force at the stem-substrate interface is less than that generated by the disk. This force can be found from relative force division as

$$F_{eff}(f) = F_{zz}(f)\frac{k_1}{k_1 + S(\omega)} \tag{3.16}$$

where k_1 is the stem stiffness, S_0 is the dynamic stiffness of the substrate and $F_{zz}(f)$ is the force amplitude at the stem-disk interface.

3.4.3 Q-factor calculations

Reviewing (3.1) in context of the model outlined above, the two parameters to be found, are the energy, W, and the energy drained per cycle, ΔW . While W can be found as the kinetic energy as given in (2.16), ΔW must be found from the response of the substrate, $u_0(\omega)$ (ref.

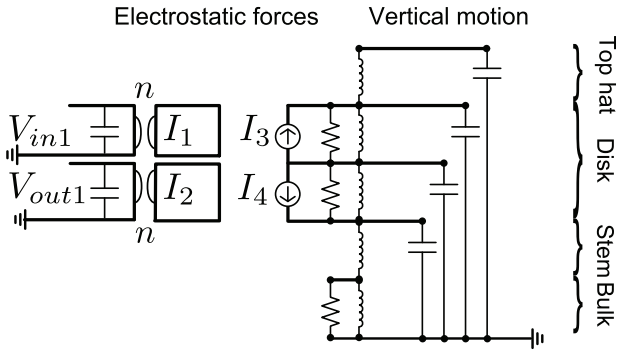

Figure 3.7: A suggestion for a equivalent circuit based on the model presented in this chapter and the equivalent circuit presented in Figure 2.10.

Figure 3.6) and the dynamic stiffness $S(\omega)$

$$\Delta W = \frac{\omega}{2} u_0(\omega)^* Im(S)(\omega) u_0(\omega) \tag{3.17}$$

where * means the complex conjugate [6].

3.4.4 Equivalent circuit modeling

Using the same approach as outlined for the double disk resonator in subsection 2.4.6, the SMD of Figure 3.6(b) can be transformed into an equivalent circuit suitable for simulating with a circuit simulator. The resulting circuit is illustrated in Figure 3.7.

3.5 Resonator model

3.5.1 Disk model

The expressions describing a periodic radial deformation of a single disk was given in subsection 2.4.2. Once, more, the radial deformation of the disk causes a deformation over its thickness due to the Poisson's ratio. The expressions for this vertical deformation u_{zz}(2.33) and rate of deformation v_{zz} (2.34) over half its thickness was derived in section 2.4.3. The force generated by this deformation can be found as the reaction forces of the disk. Assuming negligible damping in the disk itself, the reaction forces become

$$F_{disk} = k_d \times \bar{u}_{zz} + m_d \times \bar{\ddot{u}}_{zz} \tag{3.18}$$

where $\bar{u}_{zz}$ and $\bar{\ddot{u}}_{zz}$ are the deformation and the acceleration at the stem interface averaged over its cross section area. k_d and m_d are the equivalent stiffness and mass for the disk at the stem interface, respectively. Their expressions were derived in section 2.4.3 and are given in (2.37) and (2.36), respectively. In the analysis of the structure, it was assumed that the center of gravity of the mass could be assumed to be at rest. Hence the reaction forces from acceleration are not

to be included, and (3.18) can be reduced to

$$F_{disk} = k_d \times \bar{u}_{zz} \tag{3.19}$$

3.5.2 Stem model

The center stem height is governed by the thickness of a sacrificial oxide. Typical thicknesses for sacrificial oxides in surface micromachined devices are less than $1\mu m$. In [2], the sacrificial oxide used is $0.7\mu m$ thick. If the stem height is small compared to the acoustic wavelength, the stem can be considered as a compression member and there is no need to consider it as a waveguide. For pSi with a Young's modulus of 160 GPa and density 2320 kg/m^3, the frequency where 1/8 of a wavelength is about 0.7 μm is 1.1 GHz(ref. Figure 3.5). Hence a quasi static model of the stem is acceptable up to frequencies of about 1 GHz. Assuming small displacements such that the cross section of the stem can be considered uniform over the length of the stem, the effective stiffness and mass of the stem can be found as[52]

$$k_s = \frac{\pi r_s^2 E_s}{h_s} \tag{3.20}$$

$$m_s = \pi r_s^2 h_s \rho_s \tag{3.21}$$

3.6 FEA of support losses

Above, the derivation of an all analytical model for support losses based on the following assumptions is shown:

- Waves propagating away from the surface remain plane
- The substrate can be modeled using isotropic material properties for the <100> direction in single crystal silicon.
- Force applied to the surface is uniform.

To verify the model validity, FEA using the commercial software COMSOL 3.5 has been performed using the above simplifications. Computational effort was minimized through the use of an axisymmetric model. To mimic the infinity of the substrate, it was modeled with a central core embedded in a PML. Ideally this layer provides a reflection free boundary which absorbs all inbound energy. In the axisymmetric FEA model used here and illustrated in Figure 3.8, the PML surround a square central section which is assumed lossless, homogeneous and with isotropic material properties as listed in Table 3.1. The interface forces from the resonator

Table 3.1: Material parameters for SCS for a <100> direction [1]

Substrate:SCS (100)		
Young's modulus $\langle 100 \rangle$	130	[GPa]
Poisson's ratio $\langle 100 \rangle$	0.28	[-]
Density	2330	[kg/m^3]

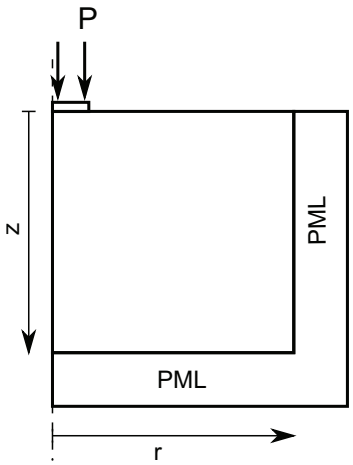

Figure 3.8: The model used for evaluation of the bulk includes an infinitely stiff and light disk on the surface through which forces were applied. Under this disk, an isotropic region with properties similar to <100> silicon is embedded in a PML.

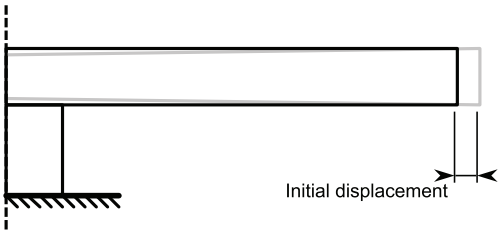

Figure 3.9: The FEA model that was used to extract the interface forces resulting from a radial amplitude of 10 nm.

footing were mimicked with a harmonic line load ([N/m]) applied to the top line of an additional area with infinite stiffness and lightness. This additional area was included to mimic the assumption of a uniform load. An axisymetric FEA model of one disk an stem system as illustrated in Figure 3.9 was given an initial radial deformation of 10 nm and simulated for a few cycles. The amplitude of the resulting force at the bulk interface was extracted and used to find the value for the line load. A frequency sweep from 10 Hz to 1 GHz in 500 steps was performed and the response of the substrate model logged to file.

Although state of the art FEA software packages have the capability to model the disk resonators of interest here in great detail, including effects of temperature, electrostatic actuation and readout, squeeze- and slide film effects, thermo-elastic damping and anisotropic material properties, such a complex model would be beyond the scope of this work. Much work has been put into the modeling of the stem effects in sections 2.4 and 2.5 and expressions derived for the disk and bottom stem for the in-phase mode of the stacked double disk resonator. These expressions were verified and can be transferred directly to the single disk resonator model. Therefore the FEA used here only includes the semi-infinite half space with calculated interface forces

and not the disk- and stem structure in order to minimize the computational effort for the time consuming frequency sweeps.

3.7 Evaluation of the bulk model

3.7.1 Analytical versus FEA model

During development of the FEA for the substrate reference model, it became clear that the size of its core (See Figure 3.8) affected the result. The response of the bulk changed periodically with frequency and shifted with the core size. This was interpreted as if the PML elements were by no means *perfect*, and that the boundary between the undamped central core and the PML, reflected energy. The variation in the response is believed to be due to standing waves in the center core due to the imperfect boundary conditions. The data extracted from the FEA is therefore averaged over results from nine different core sizes before compared with results from the analytical model. The comparison is shown in Figure 3.10(a) with standard deviation from the averaging indicated with dashed lines. As can be seen in Figure 3.10(b), the analytic model

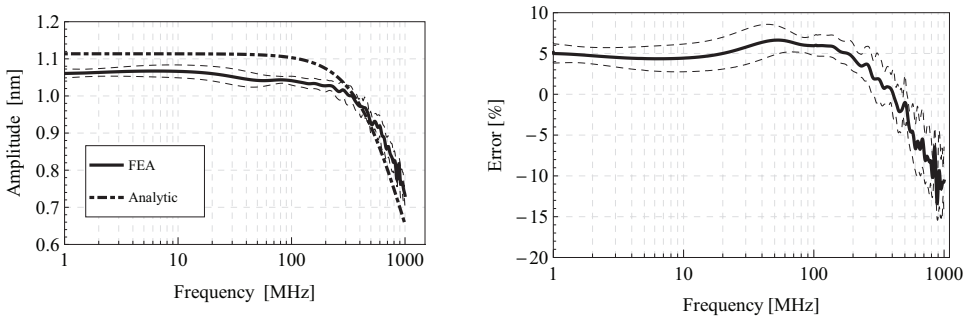

Figure 3.10: (a) Comparison of surface response for analytic model and FEA results. FEA data are the average of 9 simulations with various sizes for the bulk core. Dashed lines indicated the standard deviation of the FEA results. (b) Error estimation for analytical model versus FEA. Model uncertainty indicated with dashed lines.

overestimates the surface amplitude by about 5% up to about 500 MHz. Above this frequency, the model underestimates the surface amplitude. Relative error for the frequency range up to 1 GHz is less than 15%.

3.8 Evaluation of the analytical expression for Q

The model for the bulk, stem and a single disk as described in the previous sections was implemented in Mathematica [129], a commercial Computer Algebra System (CAS).

To calculate the response of the full analytical model, the radial disk amplitude used for the initial condition of the FEA model was used. Inserting dimensions and material parameters

from the single disk system described in [2], the Q-factor was then found from (3.1). To evaluate the model, geometric dimensions and material parameters from [2] were used. These are given for a pSi disk and stem section in Table 3.2. The expression for Q-factor can be found from inserting equations (3.17) and (1.2) ($W = KE$) into (3.1). The expanded expression for W can be found in (2.16) while ω, $u_0(\omega)$ and $S(\omega)$ from (3.17), can be found in equations (2.13), (3.16) and (3.10), respectively.

Table 3.2: Material parameters and geometric dimensions as used in [2]. κ value taken from [3].

Parameter	Value	Units
Polysilicon disk and stem		
Young's modulus	160	[GPa]
Poisson's ratio	0.226	[-]
Density	2330	[kg/m^3]
Disk radius case 1	18	[μm]
Disk radius case 2	10	[μm]
Disk thickness	2.0	[μm]
Stem radius case 1	1.0	[μm]
Stem radius case 2	0.8	[μm]
Stem height	0.7	[μm]
κ	1.998	[Hz/m]

With the values from tables 3.2 and 3.1 inserted in (3.1) for disks of radius 18 μm and 10 μm and comparing it to the corresponding Q-factors from [2] at low pressure, as listed in Table 3.3, one finds that the analytic model give about 50 % of the experimental value.

Table 3.3: Experimental results from [2] and values calculated from the analytic expression.

		From [2]		Analytic model	
	Disk radius	Frequency	Q-factor	Frequency	Q-factor
Case 1	18 μm	151.3 MHz	12289	150.283 MHz	5476
Case 2	10 μm	274.0 MHz	8950	270.509 MHz	2752

3.9 Discussion of model for support losses

The total Q-factor is calculated from (3.2) where the contribution from the support losses will only be one of several loss mechanisms. Although support loss has been identified to be the main loss mechanism for centrally supported single disk resonators at low pressures [3], the other loss mechanisms are still present and contribute to lowering the total Q-factor. Given a perfect model for the support loss, it would be expected that it would overestimate the Q-factor compared to experimental measurements. For the model developed here, the geometry was assumed perfect and according to the dimensions given in [2]. It is not stated whether the given dimensions are measured or mask and process dimensions. In addition, a SEM picture of the

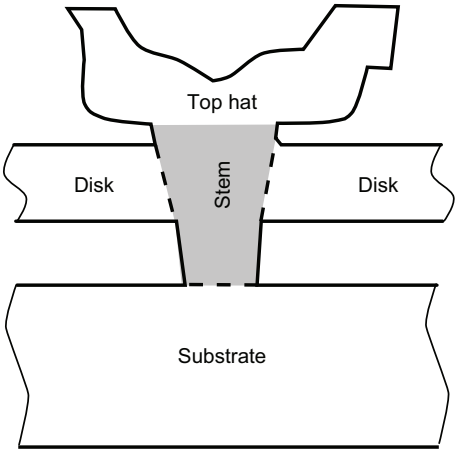

Figure 3.11: Sketch of the cross section of a single disk systems as depicted in [2]. As the stem cross section is tapered, the effective radius is different from the corresponding mask dimension. As the photolithography defining the stem radius is performed on the disk structural layer, the effective stem radius can be assumed to be less than the corresponding masks dimension.

stem section, illustrated in Figure 3.11, show how the stem is tapered, but this is not quantified. Investigating the model's sensitivity to changes in stem radius, as plotted in Figure 3.12, it becomes apparent that even small changes (≈10%) of the stem radius of the analytic model means it can reproduce the Q-factors from [2]. One uncertainty with the model and the comparison

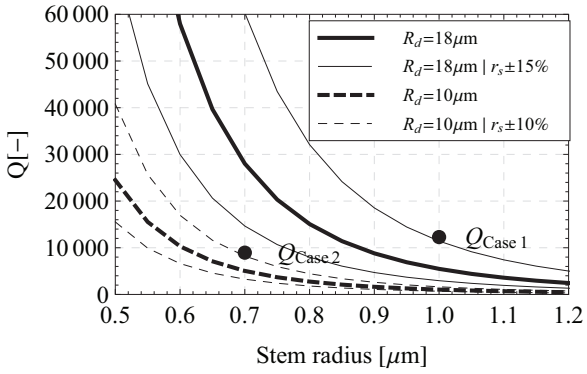

Figure 3.12: Analytic sensitivity of the Q-factor to changes in stem radius.

with the experimental results, is that the model does not include the multiple layers between the base of the stem and the silicon bulk present in the reference devices [2]. These layers can provide acoustic mismatch, and thereby reflect more energy back into the resonator. These layers can also, if sufficiently thick and with a large mismatch, provide waveguides for Rayleigh waves, and thus increase the support loss. This depends on the geometry of the waveguide layer within a few wavelengths distance from the center of the stem. Given the thickness of the layers

in [2], which are small compared to the wavelengths of both case 1 and 2, the first argument is more likely than the latter. The experimental results from [2] fall within the range of the analytic model if one assumes the dimensions given are mask dimensions, and that the actual effective stem radius is somewhat smaller due to the tapering depicted in Figure 3.11. Compared to other models found in the literature [114, 3], the model evaluated above provides a very simple analytical derivation, it does not make use of non-physical parameters and can easily be extended to include multi-structural layers while still providing accuracy comparable to the other significantly more extensive and complicated models for support losses [114, 3]. Hence it provides means of design support to the designer, and can be used to extend the capabilities of equivalent circuit simulations of resonators where support losses are of significance.

3.10 Further work

Similar to as for the double disk resonators, comparison with measurements from fabricated devices with dimensions spanning the range of interest would be preferable. If such measurements were available, more reference points could have been used in Figure 3.12, and hence provide better means of understanding the shortcomings of the model. If measurements for resonators can be found in the literature where the effect of support losses can be isolated from other mechanisms, the models presented for various load cases in [6, 7] can be evaluated for more load cases. Also, although equivalent circuit models have been mentioned many times, no such model has been implemented and its performance investigated. However due to limited time and funds, this remains a task for the future.

3.11 Summary

The model presented for support losses is derived using a simple all-analytic method where no non-physical parameters are used, and it is suitable for conversion for use in equivalent circuit simulations. Using nominal dimensions from [2], the model gives about half the value of the measured Q-factor reported on in the literature. However, only small reductions in stem radii are enough to reproduce the measured Q-factors. Such reduction in effective stem radii of the experimental devices can be argued from the stem tapering illustrated in Figure 3.11. The analytic model therefore provide a new level of usability for estimating support losses in single disk resonators, and can easily be extended to do so for the double disk resonator presented. The main contribution in this chapter, is the introduction and evaluation of a lumped parameter model adopted from the soil-structure interaction community.

Part II

Micromachined microphones

Chapter 4

Micromachined microphones for photoacoustic sensor systems

4.1 Introduction and motivation

Modern office and public buildings are fitted with extensive HVAC systems to ensure air quality and comfort. Such systems are typically configured on a room per room basis at installation and the dynamic airflow is adjusted via one centrally placed valve for each section/floor. If inexpensive gas sensors of sufficient sensitivity and resolution could be developed, they can be fitted along with an adjustable valve in each vent, and the air flow could be adjusted according to what is needed and hence reduce unnecessary exchange of air. The concept is termed DCV and a large number of papers on this topic can be found on various aspects such as control algorithms [130] and cost analysis [131].

Through efficient DCV, optimized airflow rates can be achieved, avoiding unnecessary exchange of heated or cooled air and thereby reduce ventilation cost with 5% to 80% depending on the climate [132, 133].

While many methods for measuring gas concentrations exist, Non-Dispersive InfraRed (NDIR) detection and PAS are two of the common methods used for HVAC CO_2 sensor systems [132, 133]. This is due to their potential for high sensitivity and low cost [132]. Such devices with resolutions down to 0.1 ppm already exist, but require calibration every 2 to 5 years and are still too large and/or too expensive [132].

The work presented in the following sections presents two microphones fabricated using an industrial MPW service in which tire pressure sensors are made in tens of millions per year for a cost of less than one Euro per sensor. The intended application is for monitoring low frequency acoustic signals in a low cost CO_2 PAS system. The focus of the work has been to increase the sensitivity and resolution of the microphones compared to the microphone presented in [134, 135]. The aim is to develop the microphones using a process that enables a complete PAS system to cost less than 10 €. This means that each microphone must cost less than 2 €.

4.2 Background

4.2.1 Photoacoustic gas sensing

About 1880, Alexander Graham Bell discovered the photoacoustic effect [136, 137]. He observed that when chopped light was incident to a confined absorbing gas, an audible signal was generated.

The observed audible signal is generated by the thermal expansion resulting from the absorption of the periodic light. The principle has been used for spectroscopy of solids and semisolids [136], measuring thermoelasticity, generating mechanical motion, monitoring de-excitation processes and gas concentration measurements [137]. Here, only PAS for gas sensing is described. For an extensive review on the use of photoacoustics, see [137].

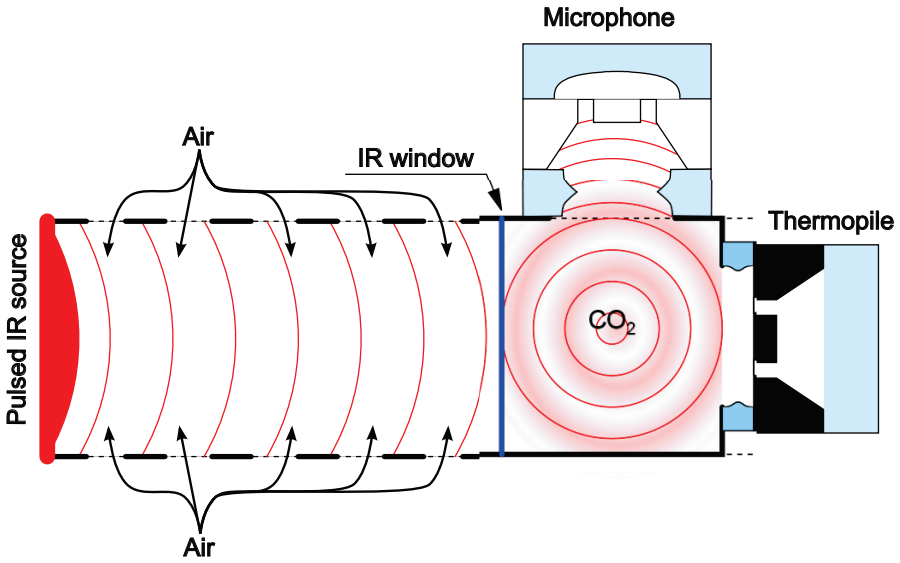

Figure 4.1: An illustration of a PAS with all important components.

Figure 4.1 shows a sketch of a PAS for low cost CO_2 monitoring similar to what is described in [138]. To the left, a solid state Infra Red (IR) source as described in [139] emits pulsed light. The light passes through a ventilated tube to allow the ambient air to be sampled. As all gases have unique absorption spectra, the spectral intensity inbound to the reference chamber on the right, is inversely exponentially proportional to the concentration of various gases in the sample. When the light enters the reference chamber filled with the gas whose concentration one wants to measure, absorption occurs only at the spectral absorption lines of that specific gas. This means that the resulting thermal expansion in the reference chamber is inversely exponentially proportional to the gas concentration of interest in the sample, which again means that the

amplitude of the generated acoustic signal is inversely exponentially proportional with the gas concentration in the sample. The uniqueness of the absorption lines, gives in principle the measurement near perfect selectivity.

On the very right, is a micromachined thermopile. This is used to monitor the radiation intensity of the IR emitter and provides means of long term stability and makes the system less sensitive to pollution and dirt. On the top of the reference chamber sits a microphone to monitor the acoustic signal. This microphone is the focal point of the work presented here.

4.3 Design principles

4.3.1 What is a microphone

A microphone is a transducer that transforms time varying pressure to electrical signals. This is commonly done through the use of a membrane absorbing the energy of the signal. Depending on the transducer mechanism used, the membrane deforms, deflects or maintain its position. Most macroscopic microphones are the so-called condenser type, where a membrane is configured as a moving electrode in a variable capacitor. When the acoustic signal deforms the membrane, the resulting change in capacitance can be monitored using external circuitry. An illustration of such a condenser microphone is given in Figure 4.2.

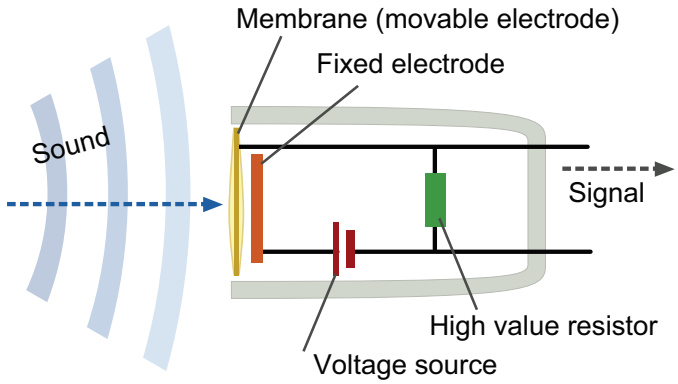

Figure 4.2: An sketch of a condenser microphone illustrating the main principle and configuration. The energy of acoustic signal is absorbed by a moving membrane. The change in the gap between the membrane and a charged and fixed electrode gives rise to a change in the capacitance which can be monitored using external circuitry. Image courtesy of Banco, licensed under Creative Commons.

The sensitivity and resolution of a moving membrane microphone is governed by the size and compliance of the membrane and the efficiency and Signal to Noise Ratio (SNR) of the transducer mechanism used. For low cost micromachined microphones, it is desirable to minimize the size and since the transducer mechanism determines the fabrication process required,

the remaining design parameter where design optimization can be done, is the design of the compliance for the membrane and its suspension.

While many types of macroscopic microphones exists, here the focus is on micromachined microphones which is mainly motivated by the potential for low cost.

A large number of micromachined microphones are described in the literature. The most common type is the condenser microphone [140, 141, 70, 142, 143] which is basically a capacitor with an acoustically movable electrode. They are acknowledged to be the microphones offering the best sensitivity and lowest noise [144]. However, as the sensitivity is proportional to the bias voltage, they require high biases and hence complicated external circuitry, effectively increasing the cost. Microphones based on piezoelectric materials have also been presented [145, 146, 147, 148, 149, 150]. However, long term stability issues, especially for piezoelectric ceramics [151, 152] makes piezoelectric materials less suitable for DCV applications.

In [153] a PAS system using a simple cantilever microphone and optical readout is presented. While providing high sensitivity, the use of the optical readout makes this system incapable of meeting the requirement for a 10€ system. Another example of a PAS with optical readout is given in [154], which owing the use of a He-Ne laser and optical fibers for signal input and readout, would be too expensive for this application.

Piezoresitive sensors have a long history, and manufacturers such as SensoNor fabricate tens of millions of Tire Pressure Sensors (TPSs) for less than 1€ a piece. Several piezoresistive microphones have been presented in the literature [155, 156, 157] with [134] specifically designed for a PAS for CO_2. In the following sections, two piezoresistive microphones based on the same process as used in [134], are presented.

4.3.2 Increasing the compliance of micromachined membranes

The compliance, being the inverse of the stiffness, for a microphone can be increased in two ways: Using a material with a lower Young's modulus or designing a softer mechanical structure. Most micromachined microphones found in the literature have a membrane fabricated from one or more of the materials silicon [158], poly-silicon [159], silicon nitride [140, 142] or aluminum [160]. The design of high-compliance structures for microphones can be divided into two classes: The design of clamped high-compliance membranes and the design of suspension schemes for released membranes.

Clamped high-compliance membranes are commonly designed through adding corrugations [143, 161, 162, 163, 164, 165] as illustrated in Figure 4.3(a). Although these do provide increased compliance compared to non-corrugated membranes, they are still stiffer than released membranes [162]. An example of a released membrane design is illustrated in Figure 4.3(b).

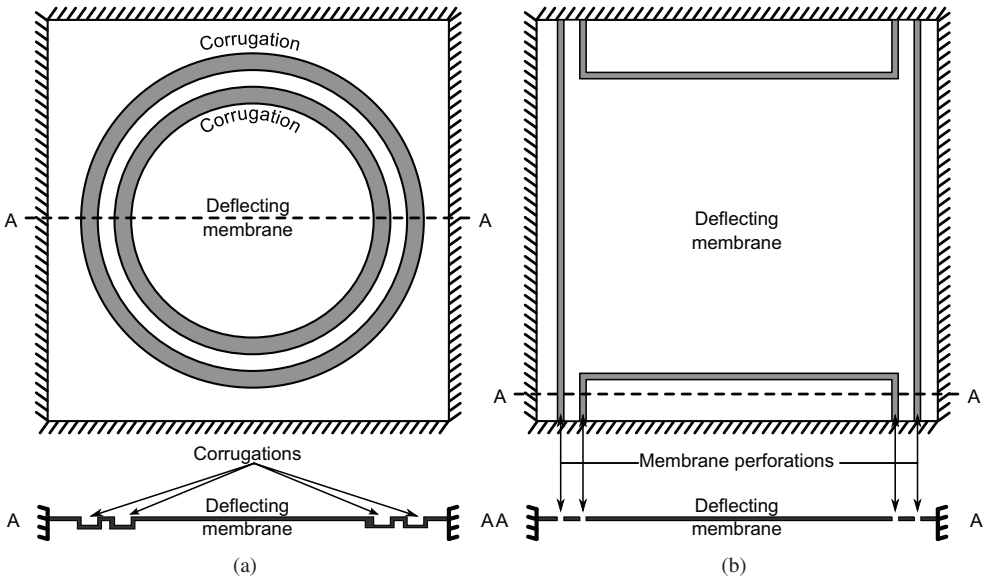

Figure 4.3: (a) Top view and cross section for a clamped and corrugated membrane. The corrugations are used to obtain a larger deflection of the membrane. (b) Top view of a released membrane

The penalty of using released membranes instead of fully clamped membranes is decreased low-frequency sensitivity since parts of the acoustic signal can pass through the membrane openings. Most of the micromachined microphones presented in the literature, are designed for the audible range, meaning that a broad and flat frequency response is desired in the range 20 Hz-20 kHz. While the upper frequency response of microphones is mainly governed by mechanical resonances and gas damping, the low end of the frequency range is governed by the compliance and the size of ventilation openings.

Since the dimensions of a microsystem are much smaller than the acoustic wavelength at frequencies below 100 Hz, the time varying pressure and resulting gas flow can be treated as an incompressible fluid flow rather than an acoustical signal. A steady state laminar flow Q_v through a channel of depth t, width w and length l (ref. Figure 4.4) and with $l >> w$ can be described by [166]

$$Q_v = \frac{lw^3}{12\mu t}\Delta p \tag{4.1}$$

where Δp is the pressure over the slot openings and μ is the viscosity of the gas flowing through. Although (4.1) is only valid for deep slots where a stable laminar flow can be established, it highlights the geometric dependencies. While the slot length equals the perimeter length of the membrane whose area is directly related to the sensitivity, the slot width and depth can be altered with no effect on the membrane area. Hence a reduction in slot width and an increase in slot depth are desirable for lowering the cut-off frequency of the microphones and maximize the sensitivity at low frequencies.

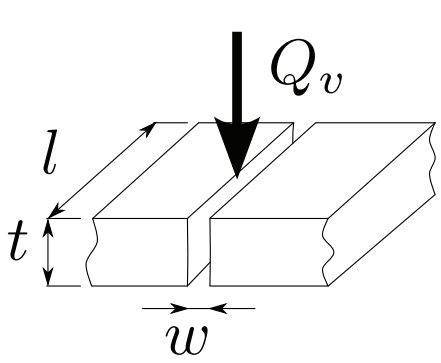

Figure 4.4: A sample geometry included to illustrate the geometric parameters of the slot in the slotted membrane designs presented here. The volumetric flow Q_v through a narrow and deep slot generates a pressure difference over the depth of the slot.

Several released membrane designs with various suspension schemes can be found in the literature. In [153], a membrane is suspended along only one edge, while in [167] four straight beams are used. While folded and serpentine shaped beams can be used to achieve a high-compliance suspension [168, 169], they require large areas, and will increase the length of the perforation slots, thereby reducing the sensitivity of the microphone. While beams parallel with the edges of the membrane also provide efficient use of the available space, added mechanical strength for large displacements can be achieved through the use of beams with aligned center lines, which gives stress stiffening when the membrane is subject to large loads. In addition it complicates the design of the membranes and suspension of different thickness desired to minimize Q_v, and used in subsection 4.4.2.

Using a MPW service, the die sizes are predetermined, limiting the dimensions of the device. To maximize the membrane area while fitting it inside the available space, the most efficient solution is therefore to embed the beams inside the membrane area, resulting in a structure resembling a four-leaf clover with supporting beams between each leaf. If the beams are embedded too far into the membrane area, the microphone becomes more disposed to distortion due to decreased rotational rigidness. Hence is it desirable with short thin beams rather than long thick beams.

As a trade-off between high-compliance, manufacturability and minimizing the perforation slot lengths, a membrane suspended by four straight beams is therefore chosen. For a straight beam of varying thickness, relevant when designing for the MultiMEMS process (ref. subsection 4.3.3), the effective compliance can be found as [52]

$$C_{eq} = \int \frac{L_b^3}{12 E_y I(x)} dx \tag{4.2}$$

where L_b is the beam length, E_y is the isotropic Young's modulus and $I(x)$ is the second area moment of inertia of a beam with thickness varying along its x-axis. $I(x)$ for a rectangular

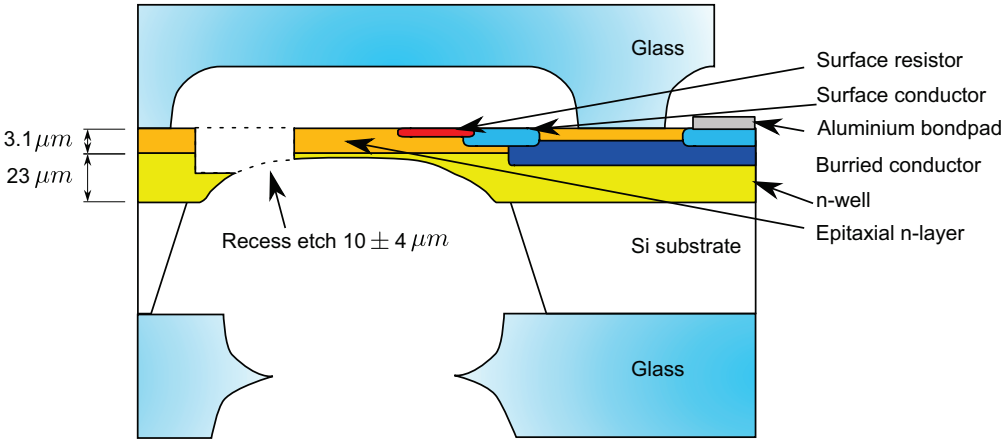

Figure 4.5: A cross section view of a random MultiMEMS structure. The wafer level assembly consist of three wafers: two glass wafers anodically bonded to each side of a silicon substrate. Key features of the MultiMEMS process include buried feed troughs under glass, wafer level packaging with anodic bonding to form a glass-silicon-glass stack, buried and surface conductors and piezoresistors, high precision membranes of 3.1 μm and 23 μm thickness and a recess etch of 10$\pm$4 μm.

beam cross section of width w_b and thickness $t_b(x)$ is

$$I(x) = \frac{w_b(t_b(x))^3}{12} \tag{4.3}$$

which scales cubically with thickness. Inserting (4.3) into (4.2), the compliance is found to scale cubically with beam length and inverse cubically with beam thickness.

4.3.3 MultiMEMS foundry process

Before describing the details of the microphones designed according to the principles outlined above, a brief description of the fabrication process is given. This is necessary to understand the design constraints.

The MultiMEMS foundry process [170] was offered as a MPW service until autumn 2009. It offered the possibility to share the cost of fabrication with others and hence provide affordable MEMS prototyping. A brief explanation of the process is included below and a cross section illustration of a die is shown in Figure 4.5. A complete description can be found in [170].

The process is a BMM process, especially suitable for making pressure sensors and out-of-plane accelerometers. It features a complete set of buried and surface leads and piezoresistors, metal leads and buried feed-through under the top glass. Two glass wafers are etched from both sides to allow optional openings through the glass, which is anodically bonded to the silicon wafer. Low pressure cavities can be provided by not etching the outer sides of the glass. Before bonding, the wafer is etched from the backside using the alkali enchant TMAH end ECES. This

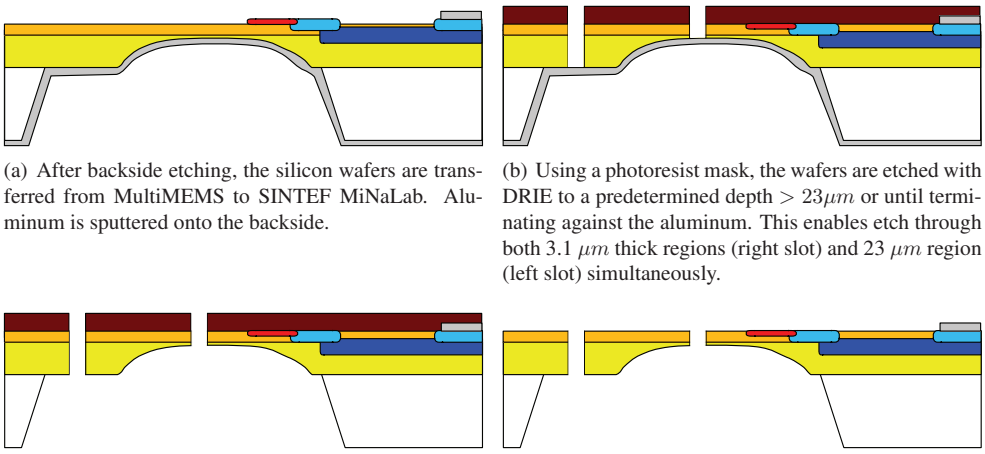

(a) After backside etching, the silicon wafers are transferred from MultiMEMS to SINTEF MiNaLab. Aluminum is sputtered onto the backside.

(b) Using a photoresist mask, the wafers are etched with DRIE to a predetermined depth $> 23\mu m$ or until terminating against the aluminum. This enables etch through both 3.1 μm thick regions (right slot) and 23 μm region (left slot) simultaneously.

(c) Aluminum is stripped.

(d) Resist is stripped and the wafers returned to MultiMEMS for anodic bonding.

Figure 4.6: Cross section view of sample die illustrating key steps used in post-processing the MultiMEMS wafers.

etch results in cavities governed by $\{111\}$ planes in the silicon and the n-type regions of either the 20 μm deep n-wells or the 3 μm n-type EPItaxial (EPI) layer at the surface. A front side DRIE allows etching of 10 ± 4 μm recesses and perforations to release structures.

Additional DRIE

For certain applications, e.g. microfluidics, it is desirable with recesses in the surface that are deeper than 10 ± 4 μm. Because of this, SINTEF MiNaLab developed a post process DRIE sequence for MultiMEMS wafers that allows etching to a predetermined depth greater than 23 μm or until terminating against aluminum. This process has been used to fabricate the microphone presented in subsection 4.4.2. A short description is therefore included in Figure 4.6

4.4 Sensor design

Based on the process description given in Section 4.3.3, two designs following the principles outlined in section 4.3 are presented. Both designs have released membranes suspended in thin beams embedded inside the membrane area. To investigate the effect of deep ventilation slots, one design is based upon the thin $(3.1\mu m)$ membrane and fabricated with the standard MultiMEMS process, while the other is based on the thick $(23\mu m)$ membrane, the MPW process and the additional DRIE. The two designs are referred to as the thin and the thick microphone, respectively.

4.4.1 Thin microphone design

In [134] an application specific microphone for PAS fabricated in the same foundry process as used here, was presented. It featured a clamped circular bossed membrane. The microphone described in this section describes a similar microphone, but with a released membrane. A top view and cross section of the modified design is shown in Figure 4.7. The microphone has

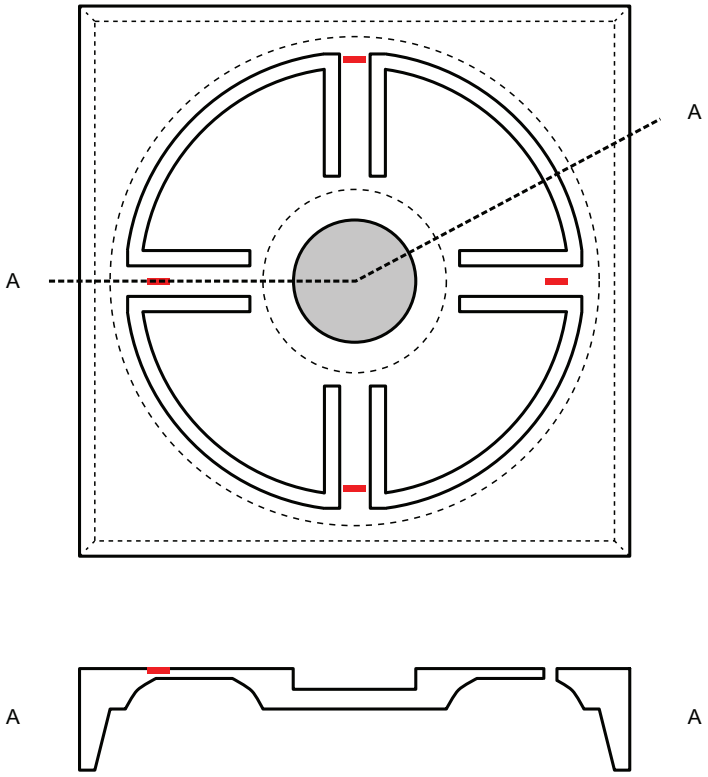

Figure 4.7: The thin microphone has a circular diaphragm. Along the perimeter, a $3\mu m$ wide slot separates the membrane from the bulk, leaving the membrane suspended by four beams inside the membrane area. In the center, a $10\mu m$ recess is included to remove excess mass.

a thin circular membrane surrounded by $3\mu m$ wide slots, leaving it suspended by four beams inside its area. The beams are 116 μm wide and 725 μm long, including the thick to thin transition regions. Piezoresistors are positioned near the base of each beam and configured in a full Wheatstone bridge to maximize sensitivity and reduce temperature effects. To maximize sensitivity it is important to locate the pizeoresistors within regions of high stress. Tapered beam designs can provide regions of constant stress [21, 171], but require extra space and wider beams. In the fabrication process, a gradual transition from the thick to the thin regions can be realized. This provides an extended high-stress region in which the resistors can be positioned. Figure 4.8 shows a cross section along the center of a beam including transition regions at both ends.

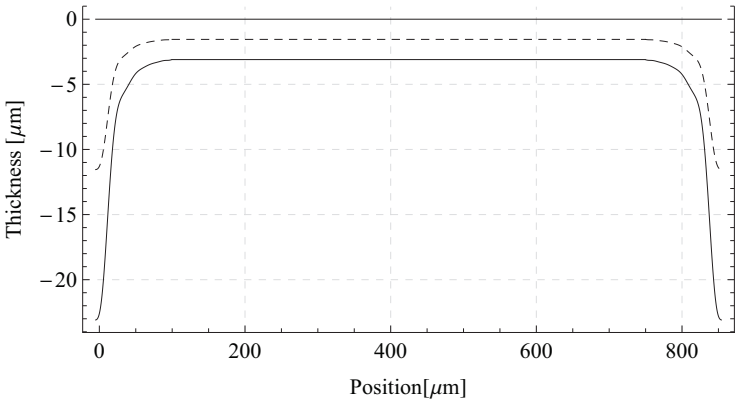

Figure 4.8: The sideways cross section profile along the center of a beam as used in the designs presented here. The example profile shown is with dimensions for the thick microphone. The thin microphone has the exact same profile, but with a shorter constant thickness center section.

4.4.2 Thick microphone design

The thick microphone design resembles the thin microphone design in having a membrane perforated along its edges and supported by four beams embedded inside the membrane region. Because the design aims to include deep narrow slots to increase the low-frequency sensitivity, the optional thick membrane is used. To still have high-compliance beams, the beams are formed from regions of $3\mu m$ thickness. This means that the membrane has two thicknesses separated by transitions as illustrated in Figure 4.9.

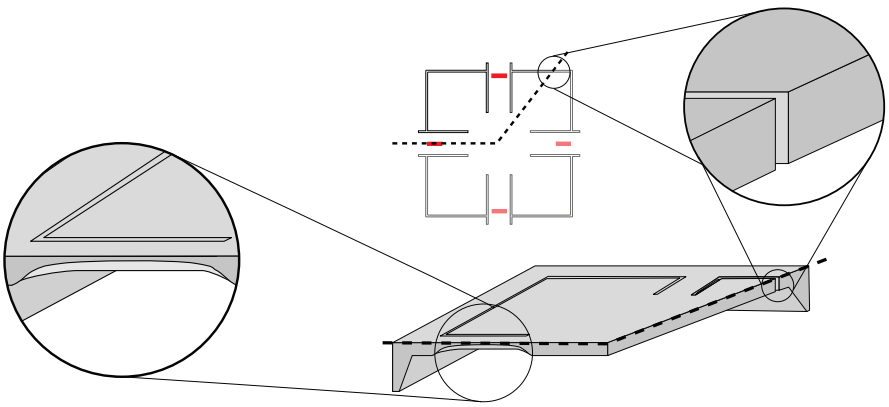

Figure 4.9: Bottom center: A 3D sketch of slightly more than one quarter of the sensor. Top center: Top view indicating the cut through a beam and the membrane. Far left: Cross section of a beam. Top right: Close up of the narrow slot of $3\mu m$ width to make the suspension system as compliant as possible while minimizing the gas flow past the membrane to maximize sensitivity.

4.5 Analytical modeling

The chosen process features a gradual transition from thin to thick areas. This has to be accounted for when modeling the compliance of the system by a function $t(x)$ describing the thickness as a function of location x along the beam. Details of the transition region can be found in [170]. The stress along the center line on the surface of the beam is now found as

$$\sigma_x(x) = \frac{M}{I(x)} \frac{t(x)}{2} \tag{4.4}$$

where M is the bending moment from the pressure over the membrane.

(4.5)

To calculate the sensitivities, the average stress over the extent of the piezoresistors is calculated by

$$\bar{\sigma}_x(x_1 \to x_2) = \frac{\int_{x_1}^{x_2} \sigma_(x) dx}{x_2 - x_1} \tag{4.6}$$

where x_1 and x_2 are the start- and end- coordinates for the piezoresistor. Changes in the resistors are found by

$$\Delta R = R(\pi_l \bar{\sigma}_l + \pi_t \bar{\sigma}_t) \tag{4.7}$$

where $\bar{\sigma}_l$ and $\bar{\sigma}_t$ are the average longitudinal and transversal stresses found separately for unidirectional stress in (4.6), respectively. π_l and π_t are the corresponding piezoresistive coefficients as given in [170]. Since the resistors are best configured in a full Wheatstone bridge to maximize sensitivity and minimize temperature effects, the output voltage is calculated as

$$V_{out} = V_{in} \left(\frac{R_t}{R_t + R_l} - \frac{R_l}{R_t + R_l} \right) \tag{4.8}$$

where R_l and R_t are the resistances of the longitudinal and transversal resistors, respectively. The sensitivity is then found as

$$S = \frac{V_{out}}{\Delta P} \tag{4.9}$$

where ΔP is the pressure over the membrane. For piezoresistive sensors, it is also common to normalize the sensitivity with respect to the supply voltage as the output voltage varies with the voltage of the input power supply.

$$S = \frac{V_{out}}{\Delta P} \frac{1}{V_{in}} \tag{4.10}$$

4.5.1 Finite element analysis and material parameters

The FEA software ANSYS V.11 is used to verify the analytic model and calculate stresses from large displacements. Since the stress in the beams is unidirectional, isotropic parameters for silicon in $\langle 110 \rangle$ can be used with little loss of accuracy. Material parameters used are listed in Table 4.1

Table 4.1: Material parameters for the SCS silicon is taken for a $\langle 110 \rangle$ direction from [1]

Parameter	Value	Units
Young's modulus $\langle 110 \rangle$	169	[GPa]
Poisson's ratio $\langle 110 \rangle$	0.07	[-]
Density	2330	[kg/m^3]

4.6 Characterization setup

The characterization setup reported on here was developed by Allesandro Sanginario and reported in [16].

One of the microphones presented in [134] was calibrated against a MEMSCAP SP82 pressure sensor [172] and its sensitivity was found to be $11\mu V/(V \times Pa)$. The microphones were mounted in TO-8 transistor headers, which were mounted on small circuit boards. The circuit boards were then mounted on an acoustic coupler (ref. Figure 4.10(b)) with four one inch Veco P28KC04 speakers attached as illustrated in Figure 4.10(a). Two power supplies were used to

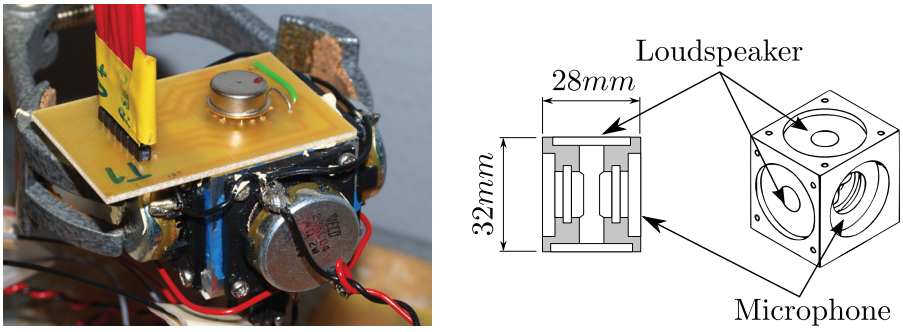

(a) (b)

Figure 4.10: (a) Four speakers, the reference microphone and microphone to be characterized were mounted on an (b) aluminum acoustic coupler to generate the acoustic signal.

power two Burr-Brown INA101 instrumentation amplifiers and a power amplifier OPA458 to drive the speakers. A separate power supply set to 5V, powered the microphones. A custom LabView program was used with a National Instruments USB-6211 Data AcQuisition (DAQ) system to generate a signal to the speakers and collect data. Data collected was digitally filtered to include data from the applied signal $\pm 5Hz$ and SIgnal to Noise And Distortion (SINAD) was extracted using standard modules from LabView. The system is illustrated in Figure 4.11.

Data was collected in 2 Hz steps over the range of interest. For each frequency, the signal was applied long enough to achieve steady state response before the measurement was made. The sensitivity was then calculated from

$$\frac{V_{ref}}{G_{ref}V_s}\frac{1}{S_{ref}} == \frac{V_{mic}}{G_{mic}V_s}\frac{1}{S_{mic}} \tag{4.11}$$

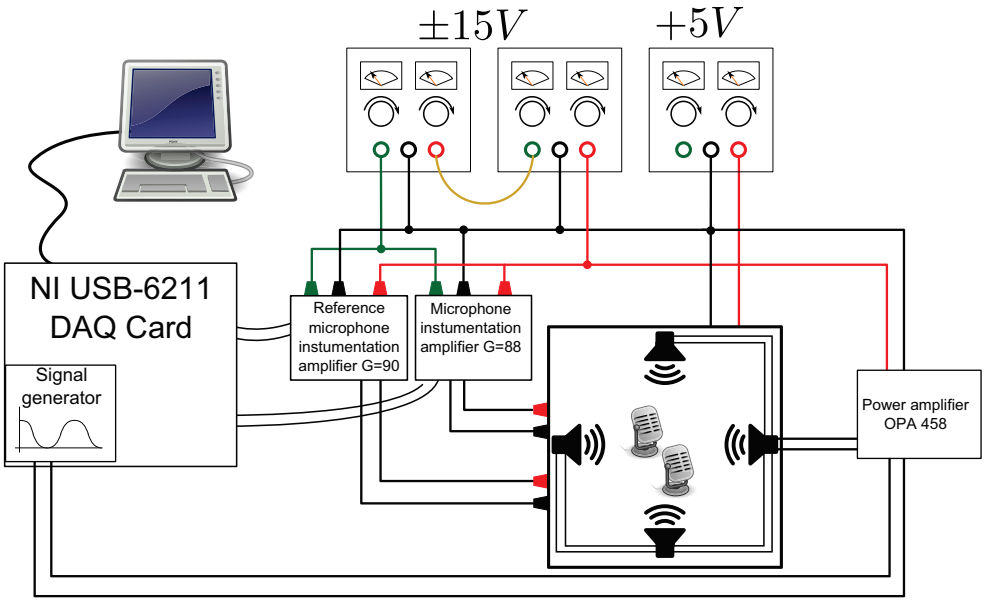

Figure 4.11: The setup for characterization consist of two power supplies at $\pm 10V$ for the instrumentation amplifiers, one power supply with $5V$ for the reference and microphone being tested. The signal is generated using LabView and a USB card model USB-6211. Microphone, computer and loudspeaker icons licensed by Creative Commons.

where subscripts ref and mic refer to the reference and microphone to be characterized, and V, V_s, G and S refers to the signal output, supply voltage, amplifier gain and sensitivity.

4.7 Results

Two versions of slotted piezoresistive silicon microphones were successfully fabricated. Both microphones were fabricated in an MPW process, one using the standard process, one using the additional DRIE. The finished 6x6 mm^2 dies are shown in Figure 4.12.

4.7.1 Modeling results

Using the expressions given in section 4.5, the mechanical sensitivities are found and verified with FEA to be about 58 $\mu V/(V \times Pa)$ and 247 $\mu V/(V \times Pa)$. Figure 4.14 shows results from FEA a comparison of the principal stress along the center of the surface of the beam for the thick design with a 1 Pa stress over the membrane. The locations of the piezoresistors are indicated by the shaded regions. The inner region is for the transversal resistors and the outer for the longitudinal resistors.

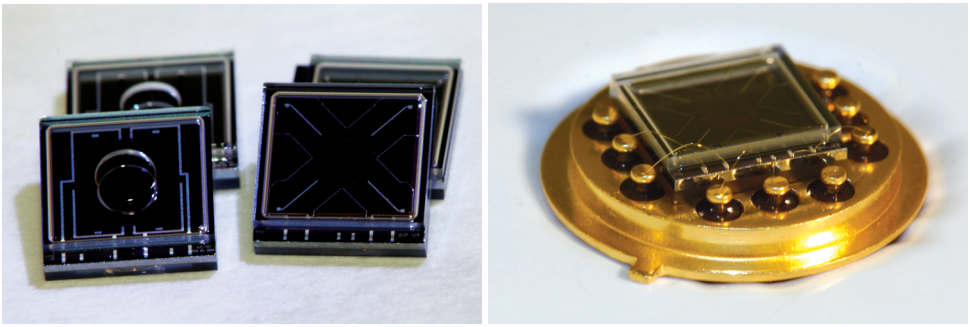

(a) (b)

Figure 4.12: (a) Two versions of the perforated microphone design has been fabricated. One with a $3\mu m$ circular diaphragm and one with a 23 μm square diaphragm. (b) Both types were mounted and wired bonded to TO-8 headers.

4.7.2 Measurements from thin microphones

A top view micrograph of the fabricated thin microphone is included in Figure 4.13(a). The four rectangles from the center toward the perimeter are the four beams supporting the membrane. The center circle is a recess in the thick region, which is surrounded by the circular $3\mu m$ thick area. The piezoresistors are located inside the gray areas (surface oxide) at the base of each beam. Leads along the diagonal outside the membrane are electrical contacts to the area under the thin regions, included to improve the reproducibility of the ECES used for precise definition of the membrane thickness.

Figure 4.15 shows sensitivity and SINAD for eight thin microphones. Sensitivity is normalized to 1 Volt supply voltage and unit amplification. Noise from the measurement setup is included in SINAD. All data was collected with constant power applied to the loudspeakers, corresponding to pressures up to 15000 Pa. Figure 4.16 shows the calculated pressure versus frequency from data collected with the reference microphone. SINAD spanned 12-33 db.

4.7.3 Measurements from thick microphones

A top view micrograph of the microphone with $23\mu m$ thickness membrane is shown in Figure 4.13(b). The rounded rectangles outline the extent of the thin ($3\mu m$) region comprising the beams. At the base of each beam, a darker area, which is surface oxide, covers the implanted piezoresistors. Extending out from the base of each beam, the narrow slots through the membrane can be seen as dark thin lines lines along the edge of the micrograph. The dark, angled Y-shaped structures inside the membrane are electrical leads used for ECES during backside etching. The circle in the center is a hole in the top glass. Figure 4.17 shows sensitivity and SINAD ratio for three thick membrane microphones. Sensitivity is normalized to 1 Volt supply voltage and amplification is not included. SINAD includes noise from both the amplifier and the microphone. Only three out of eight thick microphones were found to function properly after packaging. Two of the microphones had sensitivities one order of magnitude less than

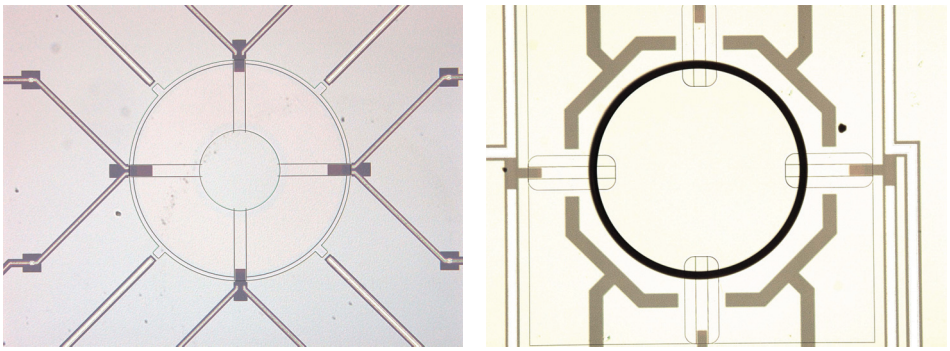

(a) (b)

Figure 4.13: Two sensors designs were fabricated successfully in the MultiMEMS MPW service. (a) The thin diaphragm microphone has a circular diaphragm. The thin line spanning an angle of 90^o between the dark gray areas, are slots of 3 μm width. The dark gray areas are regions of surface oxide covering the piezoresistors. Diaphragm diameter is 2118 μm. Along the diagonal are aluminum lines leading forward to contacts used for improving the ECES. (b) The thick membrane design has a square diaphragm of dimensions 3414 $\times$ 3414 μm^2. The perimeter slot was fabricated with a 3 μm mask line width and can be seen as a thin line tangent to the base of the beams and along the bottom of the picture. The gray lines resembling the cross section of a parabola dish leading into the beam areas and surrounding the center circular shape, are leads used for improving the ECES. The dark circle is a hole in the top glass.

those of Figure 4.17. The remaining three gave no signal at all.
As can be seen in Figure 4.17 (b), the SINAD increases with frequency up to about 55 Hz, where it starts to decrease. This decrease was identified to be caused by distortion. Data was collected only up to 100 Hz.

4.7.4 Reference microphone results

In order to discuss the microphones with respect to use in a complete PAS system, the SINAD for the reference microphone is included in Figure 4.19.

4.7.5 Slot widths

As both microphones show a variation in sensitivity, the slot widths were measured using an optical microscope, (Leica DM 4000 M). The measurements were done at a randomly chosen location along the slot opening before the dies were mounted in the transistor headers. The average measured values are given with standard deviation for each set of measurements as well as for the complete set of measurements in figures 4.20 and 4.21 for the thin and thick microphones respectively. Note that for both designs, the mask line width for the slots, were 3 μm. The thin microphone is only measured from the front side and the average slot width is about 3.8 μm, which implies 0.4 μm overetch relative to the Computer Assisted Design (CAD) drawings. For the thick microphones, two measurements are performed in order to get an idea about the shape of the slots: one from the front side in the thick areas and a corresponding

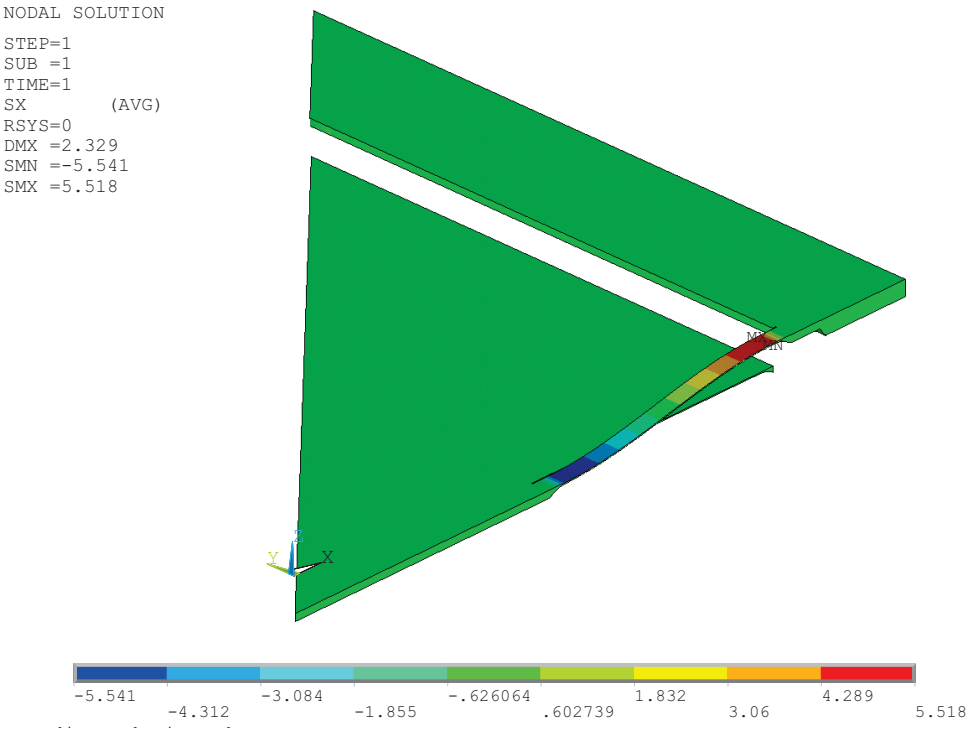

(a)

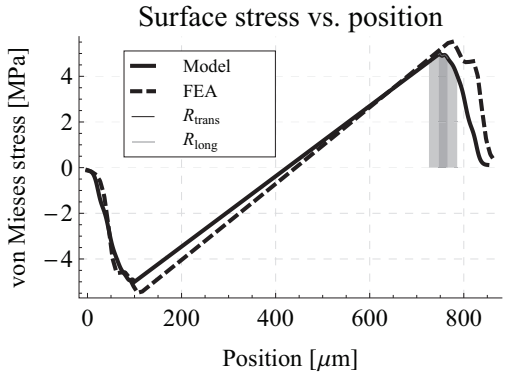

(b)

Figure 4.14: (a) Principle stress plotted for 1/8 of the thick membrane microphone using ANSYS. Curved section is one half of a thin beam. Membrane is deflected from a 1 Pa static load over the membrane. Bottom scale showing principle stress in MPa. DMX=max deflection in microns. (b) Corresponding stress profile extracted from FEA and compared to calculated stress profile.

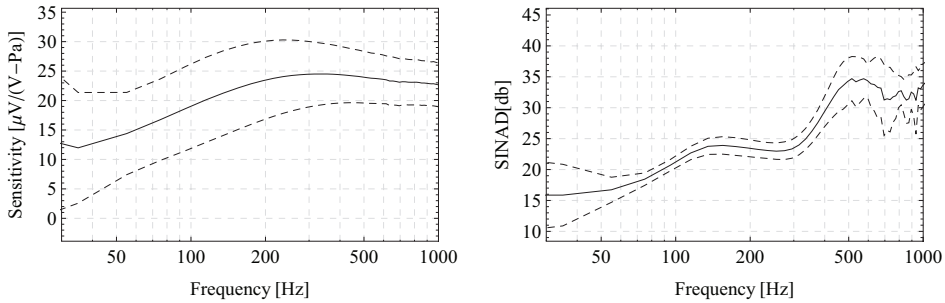

Figure 4.15: (a) The average sensitivity and corresponding standard deviation for eight microphones with thin membrane. (b) The average SINAD ratio with corresponding standard deviation for eight microphones with thin membranes.

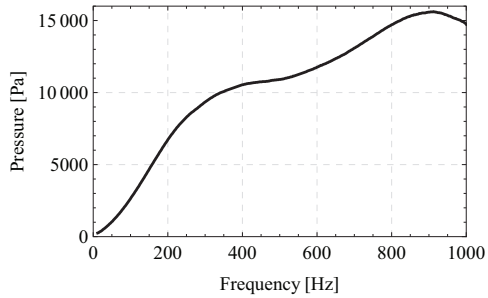

Figure 4.16: Pressures characteristic calculated from reference microphone data. Corresponding SINAD spanned 12 to 33 db.

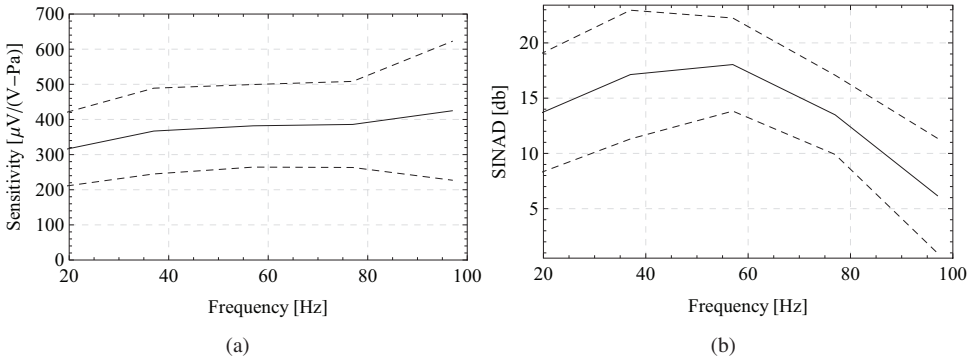

Figure 4.17: (a) Sensitivity and (b) SINAD values versus frequency for two microphones with thick membranes.

measurement from the backside. With 0.3 μm difference in slot width from the top to the bottom side, the average values from eight microphones indicate a slightly tapered shape for the

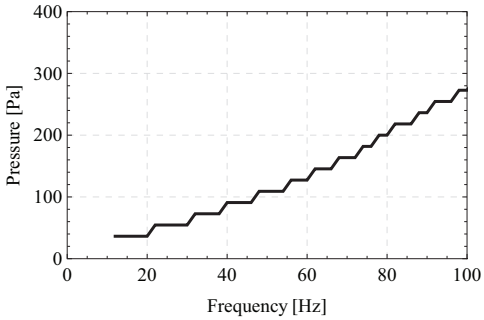

Figure 4.18: Pressures characteristic calculated from reference microphone data collected while characterizing the thick microphone. Corresponding SINAD spanned 2 to 18 db.

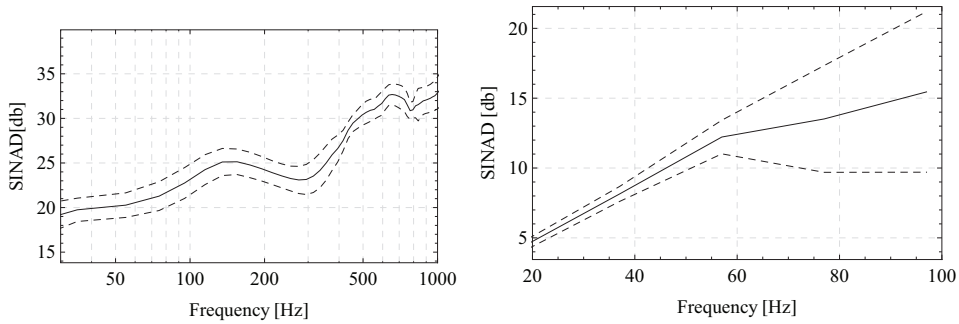

Figure 4.19: SINAD values versus frequency for the reference microphone from the measurements of the (a) thin and (b) thick microphones.

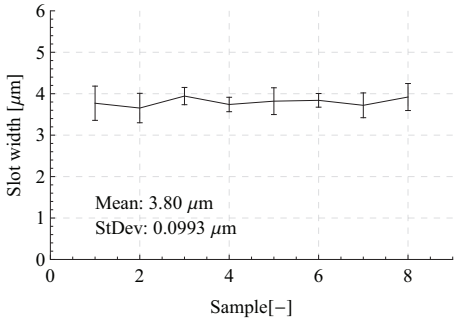

Figure 4.20: Average slot widths for thin microphone as measured from the frontside. The error bars show the standard deviation from the multiple measurements for each microphone. The text in the bottom left corner show overall average and standard deviation.

slot. From 4.21,which shows the measured slot widths on the backside of the thick membranes, it is clear that they are somewhat wider at the bottom than at the top.

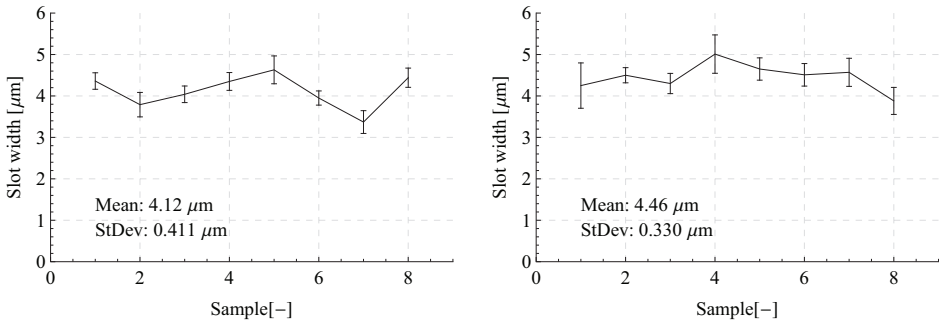

Figure 4.21: Measured slot widths with standard deviation indicated for each measured microphone and average value and standard deviation for thick microphones. (a) Values as measured from the front side. (b) Values as measured from the backside.

Chapter 5

Summary and discussion

5.1 Thin circular microphone

The thin circular microphone shows on average a doubling in sensitivity compared to the microphones presented in [134] for frequencies above 200 Hz. This is due to the increased compliance. The microphone shows a flat characteristic for frequencies between 200 Hz and 1 kHz. At the lowest frequencies, the SINAD values are low, indicating that the measurement setup is not capable of producing sufficient sound pressures or that the slot widths allow pressure equalization with a time constant similar to the frequency. According to [153] an estimate for the time constant can be found as

$$\tau = 1.58\frac{V_{eff}}{av} \tag{5.1}$$

where a is the cross section area of the gap, v is the velocity of sound and the effective volume V_{eff} is found as a function of the volumes on either side of the membrane

$$\frac{1}{V_{eff}} = \frac{1}{V_1} + \frac{1}{V_2} \tag{5.2}$$

Using these expressions and the dimensions of the thin microphone, the cut-off frequency is estimated to be less than 10 Hz. This indicates that the setup used for characterization can be improved for the lower range of frequencies. A more suitable measurement method is the use of a pistonphone, which is a simple mechanical piston compressing a known volume with a known stroke length. Hence the pressure amplitude can be calculated, removing the need for a reference microphone [173].

5.2 Thick square membrane

Only three out of eight thick microphones were found to function properly, and the functioning ones were found to have a large variation in sensitivity. The remaining five microphones mounted did not function as expected. This could be due to incomplete etching or lateral stiction, effectively leaving the membrane suspension significantly stiffer than those fully released. A visual inspection revealed that two microphones had one or more fractured beams, while for the remaining three microphones, no obvious reason was found. The characterization of the

microphone with 23 μm long ventilation slots is demanding with the current setup. If the sound pressure is increased too much, the microphones go into distortion and energy is transferred to their resonant mode, which theoretically should be about 350 Hz. When the pressure amplitude is decreased, the loudspeakers no longer supply a well defined sound pressure and the SINAD drops due to lack of signal.

5.3 Comparison of results

The thick microphones have a surface area which is about 3.3 times the area of the thin microphones. Analytical models verified with FEA indicate that the suspension of the thin microphones is about 1.45 times stiffer than that of the thick microphones. Combined, this indicates that the mechanical sensitivity of the thick microphones should be about 4.7 times that of the thin microphones. As the experimental results show a ratio closer to twenty, which is more than four times the theoretical difference, the slot dimensions must affect the sensitivity significantly.

5.4 PAS sensitivity and resolution

Since the main focus of the work presented here has been the design of microphones rather than the complete PAS systems, the microphones have only been characterized using loudspeakers. In [135] it is argued that the sensitivity of a PAS system not only depends on the sensitivity of the microphone, but also on the shape and volume of the reference chamber. The microphone used as reference in the work presented above is of the same design as in [135], in which the sensitivity for a system with a 10 cm absorption path, 1 second integration time and 10 Hz modulation frequency, gave a CO_2 resolution of 40 parts per million (ppm). For a microphone with the same SINAD, a doubling of sensitivity would give a resolution of 20 ppm. Because the measurement setup used here is incapable of producing pressures at 10 Hz, no direct comparison is possible. Comparing the SINAD at higher frequencies for the reference microphone (Figure 4.19) with SINAD for the thin and thick microphones (figures 4.15(b) and 4.17(b), respectively), it is clear that the thin microphone should give a system with a lower resolution than the reference microphone [134, 135] used. The thick microphone should however give an increase in resolution by approximately one order of magnitude compared to that presented in [135]. This strongly indicates that sub-ppm resolution of CO_2 is achievable using these microphones in an optimized PAS system.

5.5 Further work

The two main problems discussed above are the lack of good acoustic input signal at low frequencies and the yield of the dies with thick microphones. The latter can be improved by reducing the thickness of the mass in areas not to be perforated to reduce the mass of the membrane, while the first can be addressed through the use of a pistonphone. The difference in sensitivity between the thin and thick microphones cannot be explained from the mechanical models alone. Therefore further investigations with microphones with different slot lengths are

required to uncover the effects of the slot length. In order to achieve sub ppm resolution, this is to be followed by a design optimization of the front and back chambers of the microphones relative to the reference chamber of the PAS before in-system characterization is performed.

Chapter 6

Concluding summary

In section 1.1 two challenges of MEMS were identified as the main motivation for the work presented in this thesis: Integration with ICs and reducing the cost and complexity of well established technologies to make them more accessible to the market.

The work presented in Part II succeeded to address the second challenge: A new design for microphones for photoacoustic gas sensors has successfully been fabricated in a process currently used for low cost tire pressure sensors and shown to have significantly higher sensitivity than comparable microphones. However, the microphones presented is by no means optimized for mass fabrication and further development is required before they can become true low cost products. However, the designs presented show that it should be within reach to fabricate piezoresistive low cost microphones with the required resolution to enable affordable DCV.

In Part I the issue of reducing cost is also addressed. The combination of reducing the footprint meanwhile using a fabrication process that only makes use of CMOS compatible steps, should in the future enable low cost and high performance filters suitable for direct integration with CMOS circuits.

The common denominator for these two projects, are the constraints to the design of the electromechanical systems from the fabrication processes used. In addition, for both systems, modeling with both analytical as well as numerical tools has been performed. This has been useful, not only to be able to evaluate the performance of the devices prior to fabrication, but also to gain insight to the design parameters governing the various aspects of the performance.

For both system, further modeling of the dynamic behavior can be performed. The model for the resonators and their coupling mechanism should be implemented as an equivalent circuit model and evaluated. Depending on the outcome, the model might need refinement. Further, it should be generalized such that it can be used for an arbitrary number of resonators. Although such devices might currently be out of reach from a fabrication point of view, future technologies might enable such designs. Also, the formulas might be useful for bulk devices stacked sideways.

For the microphones, a dynamic model including gas flow through the perforations should be developed. No model for low frequency performance of microphones has been found during the work presented here, while such a model would be very useful for designing microphones for PAS.

The unsuccessful fabrication of the stacked resonators is unfortunately a proof of what remains one of the main challenges in microtechnology: the details of fabrication still require a costly trial-and-error based development when lateral dimensions are decreased and vertical dimensions are increased.

The incomplete fabrication trials with DSOI wafers should be picked up and completed by someone. DSOI wafers will enable fabrication of multi mass inertia sensors, new RF devices and novel structures to be discovered. While such wafers currently have to be custom made, this is a matter of volume similar to as for any other product in the semiconductor industry.

Bibliography

[1] J. J. Wortman and R. A. Evans, "Young's Modulus, Shear Modulus, and Poisson's Ratio in Silicon and Germanium," *Journal of Applied Physics*, vol. 36, no. 1, pp. 153–156, 1965.

[2] J. Wang, Z. Ren, and C. Nguyen, "1.156-GHz self-aligned vibrating micromechanical disk resonator," *IEEE Transaction on Ultrasonics, Ferroelectrics and Frequency Control*, vol. 51, pp. 1607–1628, 2004.

[3] Z. Hao and F. Ayazi, "Support loss in the radial bulk-mode vibrations of center-supported micromechanical disk resonators," *Sensors and Actuators A: Physical*, vol. 134, pp. 582–593, Mar. 2007.

[4] C. Grinde, C. Lowrie, and P. Ohlckers, "Fabrication of a MEMS triaxial accelerometer using novel post-processing of an MPW process," in *Proceedings of MME 2009*, vol. 1, p. 1, 2009.

[5] F. Ellinger, *Radio Frequency Integrated Circuits and Technologies*, vol. 69. Springer, 2 ed., 2008.

[6] J. P. Wolf, *Foundation Vibration Analysis Using Simple Physical Models*. Prentice Hall, 1994.

[7] J. Wolf and A. Deeks, *Foundation Vibration Analysis: A Strength of Materials Approach*. Elsevier, 2004.

[8] C. Mack, "Seeing double," *Spectrum, IEEE*, vol. 45, pp. 46–51, November 2008.

[9] O. N. Tufte, P. W. Chapman, and D. Long, "Silicon diffused-element piezoresistive diaphragms," *Journal of Applied Physics*, vol. 33, no. 11, pp. 3322–3327, 1962.

[10] H. Nathanson, W. Newell, R. Wickstrom, and J. Davis, J.R., "The resonant gate transistor," *Electron Devices, IEEE Transactions on*, vol. 14, pp. 117–133, Mar 1967.

[11] L. M. Roylance and J. B. Angell, "A batch-fabricated silicon accelerometer," *Electron Devices, IEEE Transactions on*, vol. 26, pp. 1911–1917, 1979.

[12] M. G. el Hak, "The Fluid Mechanics of Microdevices - The Freeman Scholar Lecture," *J. Fluids Eng.*, vol. 121, no. 5, 1999.

[13] D. Erickson and D. Li, "Integrated microfluidic devices," *Analytica Chimica Acta*, vol. 507, pp. 11–26, Apr. 2004.

[14] K. Petersen, "Silicon as a mechanical material," *Proceedings of the IEEE*, vol. 70, no. 5, pp. 420 – 457, 1982.

[15] C. Grinde, P. Ohlckers, M. Mielnik, G. U. Jensen, A. Ferber, and D. Wang, "A clover shaped silicon piezoresistive microphone for miniaturized photoacoustic gas sensors," in *Prodeedings from DTIP 2009*, pp. 256–260, EDA Publishing, 2009. ISBN:978-2-35500-009-6.

[16] A. Sanginario, C. Grinde, and P. Ohlckers, "Characterization of two novel low frequency microphones for photoacustic gas sensors," in *Proceedings of Eurosensors XIII, 2009*, 2009.

[17] C. Grinde, A. Sanginario, P. A. Ohlckers, G. U. Jensen, and M. M. Mielnik, "Two clover-shaped piezoresistive silicon microphones for photoacoustic gas sensors," *Journal of Micromechanics and Microengineering*, vol. 20, no. 4, 2010.

[18] K. H. Nygaard, C. Grinde, and T. A. Fjeldly, "Stacked Coupled-Disk MEMS Resonators for RF Applications," in *Technical Proceedings of the 2008 NSTI Nanotechnology Conference and Trade Show*, vol. 3, pp. 478 – 480, 2008.

[19] C. Grinde, K. Nygaard, J. Due-Hansen, and T. A. Fjeldly, "Lumped modeling of a novel RF MEMS double-disk resonator system," in *Proceedings of DTIP 2009*, pp. 14–18, EDA Publishing, 2009. ISBN: 978-2-3550-0009-6.

[20] C. Grinde and T. Fjeldly, "Frequency separation in vertically stacked disk resonators," *Springer Microsystem Technolgy*, 2010. Submitted for review to Springer Microsystem Technology.

[21] C. Ferreira, P. Ventura, C. Grinde, R. Morais, A. Valente, C. Neves, and M. Reis, "A novel monolithic silicon sensor for measuring acceleration, pressure and temperature on a shock absorber," in *Proceedings of Eurosensors XIII, 2009*, pp. 88–91, 2009.

[22] C. Ferreira, P. Ventura, C. Grinde, R. Morais, A. Valente, C. Neves, and M. Reis, "A self-powered embedded system for shock absorber diagnosis during vehicle motion," in *Proceedings of FISITA 2010*, 2010.

[23] C. Lowrie, C. Grinde, M. Desmulliez, and L. Hoff, "Piezoresistive three-axis accelerometer for monitoring heart wall motions," *Proceedings of DTIP, 2005*, pp. 131–136, 2005. ISBN:2-84813-0357-1.

[24] C. Lowrie, C. Grinde, L. Hoff, M. Desmulliez, O. J. Elle, and E. Fosse, "Design of a three-axis accelerometer for heart motion studies," in *Proc. Of IMAPS Nordic Conference 2005*, 2005.

[25] C. Lowrie, C. Grinde, L. Hoff, M. Desmulliez, and O. J. Elle, "Design of a miniature three-axis accelerometer for the study of heart wall motion," in *Proceedings of Micro Structure Workshop, Vesterås, Sweden, 2006.*, 2006.

[26] P. Ohlckers, L. Petricca, and C. Grinde, "A three axis accelerometer," in *Proceedings of Micromechanics Europe 2010*, 2010. Accepted for pubclication at MME 2010.

[27] C. Grinde, D. Dermarchi, P. Ohlckers, P. Civera, and S. Hansen, "An approach to seminar based MEMS training," in *Proceedings of EWME2008 - European Workshop on Microelectronics Education (Budapest) May 28-30*, EDA publishing, 2008. ISBN: 978-2-35500-007-2.

[28] C. Grinde, D. Demarchi, P. Civera, and P. Ohlckers, "An approach to short-courses in a pan-European training program in microsystem technologies," *European Journal of Engineering Education*, 2010. Submitted for review to European Journal Of Engineering Education.

[29] C. Grinde and E. Westby, "A method for adding static external forcing to invariant manifolds," in *Technical Proceedings of the 2008 NSTI Nanotechnology Conference and Trade Show*, vol. 3, pp. 636 – 639, 2005.

[30] C. Ferreira, P. Ventura, C. Grinde, R. Morais, A. Valente, C. Nevesa, and M. Reis, "Characterization and testing of a shock absorber embedded sensor," in *Proceedings of Eurosensors 2010*, 2010. Accepted for publication at Eurosensors 2010.

[31] P. Shiu, G. K. Knopf, M. Ostojic, and S. Nikumb, "Rapid fabrication of tooling for microfluidic devices via laser micromachining and hot embossing," *Journal of Micromechanics and Microengineering*, vol. 18, no. 2, p. 025012 (8pp), 2008.

[32] M. J. Madou, *Fundamentals of Microfabrication: The Science of Miniaturization*. CRC press, 2 ed., 2002.

[33] P. J. French, "Polysilicon: a versatile material for microsystems," *Sensors and Actuators A: Physical*, vol. 99, no. 1-2, pp. 3 – 12, 2002.

[34] S. A. Campbell, *The Science and Engineering of Microelectronic Fabrication*. Oxford University Press, 2 ed., 2001.

[35] J. Chae, S. Park, and T. Freiheit, "Investigation of micro-cutting operations," *International Journal of Machine Tools and Manufacture*, vol. 46, no. 3-4, pp. 313 – 332, 2006.

[36] M. Murali and S. H. Yeo, "Rapid biocompatible micro device fabrication by micro electro-discharge machining," *Biomedical Microdevices*, vol. 6, pp. 41–45, Mar. 2004.

[37] C. R. A. Chaitanya and K. Takahata, "M3EDM: MEMS-enabled micro-electro-discharge machining," *Journal of Micromechanics and Microengineering*, vol. 18, no. 10, p. 105009 (7pp), 2008.

[38] T. Li and Y. Gianchandani, "A micromachining process for die-scale pattern transfer in ceramics and its application to bulk piezoelectric actuators," *Microelectromechanical Systems, Journal of*, vol. 15, pp. 605–612, June 2006.

[39] W. Meeusen, J. Clijnen, D. Reynaerts, H. Van Brussel, and R. Puers, "Micro-electro-discharge machining as microsensor fabrication technology," *Sensors Journal, IEEE*, vol. 3, pp. 632–639, Oct. 2003.

[40] P.-P. Shiu, G. Knopf, and M. Ostojic, "Fabrication of metallic micromolds by laser and electro-discharge micromachining," *Microsystem Technologies*, vol. 16, pp. 477–485, Mar. 2010.

[41] H. Seidel, L. Csepregi, A. Heuberger, and H. Baumgartel, "Anisotropic etching of crystalline silicon in alkaline solutions," *Journal of The Electrochemical Society*, vol. 137, no. 11, pp. 3626–3632, 1990.

[42] O. Tabata, R. Asahi, H. Funabashi, K. Shimaoka, and S. Sugiyama, "Anisotropic etching of silicon in TMAH solutions," *Sensors and actuators A-Physical*, vol. 34, no. 1, pp. 51 – 57, 1992.

[43] D. Lapadatu and R. Puers, "On the anodic passivation of silicon in aqueous KOH solutions," *Sensors and Actuators A: Physical*, vol. 60, pp. 191–196, 1997.

[44] B. Kloeck, S. D. Collins, N. F. Derooij, and R. L. Smith, "Study of electrochemical etch-stop for high precision thickness control of silicon membranes," *IEEE Transactions on electron devices*, vol. 36, no. 4, pp. 663 – 669, 1989.

[45] D. Lapadatu, G. Kittilsland, M. Nese, S. Nilsen, and H. Jakobsen, "A model for the etch stop location on reversed biased pn junctions," in *Solid State Sensors and Actuators, 1997. TRANSDUCERS '97 Chicago., 1997 International Conference on*, vol. 1, pp. 715–716 vol.1, 1997.

[46] K. Williams and R. Muller, "Etch rates for micromachining processing," *Journal of Microelectromechanical Systems*, vol. 5, no. 4, pp. 256 – 269, 1996.

[47] "TRONICS HARMST MPW service." `http://www.tronics.eu`.

[48] H. V. Jansen, M. J. de Boer, S. Unnikrishnan, M. C. Louwerse, and M. C. Elwenspoek, "Black silicon method X: a review on high speed and selective plasma etching of silicon with profile control: an in-depth comparison between Bosch and cryostat DRIE processes as a roadmap to next generation equipment," *Journal of Micromechanics and Microengineering*, vol. 19, no. 3, p. 033001 (41pp), 2009.

[49] Y.-I. Lee, K.-H. Park, J. Lee, C.-S. Lee, H. Yoo, C.-J. Kim, and Y.-S. Yoon, "Dry release for surface micromachining with hf vapor-phase etching," *Microelectromechanical Systems, Journal of*, vol. 6, pp. 226–233, Sep 1997.

[50] J. H. Lee, W. I. Jang, C. S. Lee, Y. I. Lee, C. A. Choi, J. T. Baek, and H. J. Yoo, "Characterization of anhydrous HF gas-phase etching with CH_3OH for sacrificial oxide removal," *Sensors and Actuators A: Physical*, vol. 64, no. 1, pp. 27 – 32, 1998. Tenth IEEE International Workshop on Micro Electro Mechanical Systems.

[51] A. C. Jones and M. L. Hitchman, eds., *Chemical Vapour Deposition: Precursors, Processes and Applications*. RSC Publishing, 2008.

[52] W. C. Young and R. G. Budynas, *Roarks Formulas for stress and strain.* General engineering series, McGraw-Hill, 7 ed., 2002.

[53] K. Seto, M. Ookuma, S. Yamashita, and A. Nagamatsu, "Method of estimating equivalent mass of multi-degrees-of-freedom system," *The Japan Society of Mechanical Engineers International Journal*, vol. 30, no. 268, pp. 1638–1644, 1987.

[54] R. A. Johnson, *Mechanical filters in electronics*. Wiley Series on Filters, John Wiley & Sons Inc, 1983.

[55] R. D. Cook, D. S. Malkus, M. E. Plesha, and R. J. Witt, *Concepts and applications of finite element analysis*. John Wiley & Sons Inc, 4. ed., 0 2002.

[56] O. C. Zienkiewicz, R. L. Taylor, and J. Z. Zhu, *Finite Element Method - Its Basis and Fundamentals*. Elsevier, 6 ed., 2005.

[57] J.-P. Berenger, "A perfectly matched layer for the absorption of electromagnetic waves," *Journal of Computational Physics*, vol. 114, no. 2, pp. 185 – 200, 1994.

[58] Y.-G. Zhang and J. Ballmann, "Two techniques for the absorption of elastic waves using an artificial transition layer," *Wave Motion*, vol. 25, no. 1, pp. 15 – 33, 1997.

[59] D. S. Bindel and S. Govindjee, "Elastic PMLs for resonator anchor loss simulation," *International Journal for Numerical Methods in Engineering*, no. 64, pp. 789 – 818, 2005.

[60] A. H. Nayfeh, M. I. Younis, and E. M. Abdel-Rahman, "Reduced-order models for MEMS applications," *Nonlinear Dynamics*, no. 1, 2005.

[61] F. A. Firestone, "A new analogy between mechanical and elecctrical systems," *The Journal of the Acoustical Society of America*, vol. 4, no. 3, pp. 249–267, 1933.

[62] "SPICE." `http://bwrc.eecs.berkeley.edu/Classes/icbook/SPICE/`, Jan. 2010.

[63] H. A. C. Tilmans, "Equivalent circuit representation of electromechanical transducers .1. lumped-parameter systems," *Journal Of Micromechanics And Microengineering*, vol. 6, pp. 157–176, Mar. 1996.

[64] H. A. C. Tilmans, "Equivalent circuit representation of electromechanical transducers: II. distributed-parameter systems," *Journal Of Micromechanics And Microengineering*, vol. 7, pp. 285–309, Dec. 1997.

[65] T. Veijola, *Equivalent Circuit Models for Micromechanical Inertial Sensors*. PhD thesis, Helsinki University of Technology, 1999.

[66] G. Cusmai, M. Mazzini, P. Rossi, C. Combi, B. Vigna, and F. Svelto, "A simple lumped electrical model for an RF-MEMS switch considering lossy substrate effects," *Sensors and Actuators A: Physical*, 2005.

[67] F. Bannon, J. Clark, and C.-C. Nguyen, "High-Q HF microelectromechanical filters," *IEEE Journal of Solid-State Circuits*, vol. 35, pp. 1517 – 1517, 2000.

[68] Z. Hao, S. Pourkamali, and F. Ayazi, "VHF single-crystal silicon elliptic bulk-mode capacitive disk resonators-part I: design and modeling," *Journal of Microelectromechanical Systems*, vol. 13, no. 6, pp. 1043 – 1053, 2004.

[69] S.-S. Li, M. Demirci, Y.-W. Lin, Z. Ren, and C.-C. Nguyen, "Bridged micromechanical filters," *Frequency Control Symposium and Exposition, 2004. Proceedings of the 2004 IEEE International*, pp. 280–286, Aug. 2004.

[70] M. Pedersen, W. Olthuis, and P. Bergveld, "High-performance condenser microphone with fully integrated CMOS amplifier and DC-DC voltage converter," *Journal of Microelectromechanical Systems*, vol. 7, pp. 387–394, Dec 1998.

[71] W. J. Wang, R. M. Lin, Q. B. Zou, and X. X. Li, "Modeling and characterization of a silicon condenser microphone," *Journal of Micromechanics and Microengineering*, vol. 14, no. 3, pp. 403–409, 2004.

[72] S. D. Senturia, *Microsystem Design*. Kluwer Academic Publishers, 2001.

[73] E. Jezierski, *Robot Motion and Control*, vol. 335/2006 of *Lecture Notes in Control and Information Sciences*, ch. On Electrical Analogues of Mechanical Systems and their Using in Analysis of Robot Dynamics, pp. 391–404. Springer, 2006.

[74] W.-L. Huang, Z. Ren, Y.-W. Lin, H.-Y. Chen, J. Lahann, and C.-C. Nguyen, "Fully monolithic CMOS nickel micromechanical resonator oscillator," *Micro Electro Mechanical Systems, 2008. MEMS 2008. IEEE 21st International Conference on*, pp. 10–13, Jan. 2008.

[75] J. Weigold, A.-C. Wong, C.-C. Nguyen, and S. Pang, "A merged process for thick single-crystal Si resonators and BiCMOS circuitry," *Microelectromechanical Systems, Journal of*, vol. 8, pp. 221–228, Sep 1999.

[76] E. Brown, "RF-MEMS switches for reconfigurable integrated circuits," *IEEE Transaction on Microwave Theory and Techniques*, vol. 46, pp. 1868–1880, 1998.

[77] R. Borwick, P. Stupar, J. Denatale, R. Anderson, C. Tsai, K. Garrett, and R. Erlandson, "A high Q, large tuning range MEMS capacitor for RF filter systems," *Sensors and Actuators A-Physical*, vol. 103, no. 1-2, pp. 33 – 41, 2003.

[78] I. Zine-El-Abidine and P. Yang, “A tunable mechanical resonator,” *Journal of Micromechanics and Microengineering*, vol. 19, no. 12, p. 125004 (5pp), 2009.

[79] J.-M. Kim, S. Lee, J.-M. Kim, C.-W. Baek, Y. Kwon, and Y.-K. Kim, “A mechanically reliable digital-type single crystalline silicon (SCS) RF MEMS variable capacitor,” *Journal of Micromechanics and Microengineering*, vol. 15, no. 10, pp. 1854–1863, 2005.

[80] J. M. Huang, K. M. Liew, C. H. Wong, S. Rajendran, M. J. Tan, and A. Q. Liu, “Mechanical design and optimization of capacitive micromachined switch,” *Sensors and Actuators A: Physical*, no. 3, 2001.

[81] V. K. Varadan, K. J. Vinoy, and K. A. Jose, *RF MEMS and Their Applications*. John Wiley & Sons, Ltd, 2003.

[82] L. Lin, C.-C. Nguyen, R. Howe, and A. Pisano, “Microelectromechanical filters for signal processing,” in *Proc. An Investigation of Micro Structures, Sensors, Actuators IEEE Machines and Robot Micro Electro Mechanical Systems, MEMS ’92*, pp. 226–231, Feb 1992.

[83] J. R. Clark, W.-T. Hsu, and C. T.-C. Nguyen, “High-Q VHF micromechanical contour-mode disk resonators,” *Electron Devices Meeting, 2000. IEDM Technical Digest. International*, no. 6894419, pp. 493 – 496, 2000.

[84] B. Bircumshaw, G. Liu, H. Takeuchi, T.-J. King, R. Howe, O. O’Reilly, and A. Pisano, “The radial bulk annular resonator: towards a 50 Ω RF MEMS filter,” in *Transducers, Solid-State Sensors, Actuators and Microsystems, 12th International Conference on, 2003*, vol. 1, 2003.

[85] V. Kaajakari, T. Mattila, A. Oja, J. Kiihamaki, and H. Seppa, “Square-extensional mode single-crystal silicon micromechanical resonator for low-phase-noise oscillator applications,” *Electron Device Letters, IEEE*, vol. 25, no. 4, pp. 173 – 175, 2004.

[86] S.-S. Li, Y.-W. Lin, Y. X. Z. Ren, and C. T. Nguyen, “Micromechanical "hollow-disk" ring resonators,” in *Micro Electro Mechanical Systems, 2004. 17th IEEE International Conference on.*, pp. 821 – 824, 2004.

[87] S. Bhave and R. Howe, “Silicon nitride-on-silicon bar resonator using internal electrostatic transduction,” *Solid-State Sensors, Actuators and Microsystems, 2005. Digest of Technical Papers. Transducers ’97 ’05. The 13th International Conference on*, vol. 2, pp. 2139–2142 Vol. 2, June 2005.

[88] S. Pourkamali, G. Ho, and F. Ayazi, “Vertical capacitive SiBARs,” *Micro Electro Mechanical Systems, 2005. MEMS 2005. 18th IEEE International Conference on*, pp. 211–214, Jan.-3 Feb. 2005.

[89] O. Holmgren, K. Kokkonen, T. Veijola, T. Mattila, V. Kaajakari, A. Oja, J. V. Knuuttila, and M. Kaivola, “Analysis of vibration modes in a micromechanical square-plate resonator,” *Journal of Micromechanics and Microengineering*, vol. 19, no. 1, p. 015028 (11pp), 2009.

[90] L.-W. Hung, C.-C. Nguyen, Y. Xie, Y.-W. Lin, S.-S. Li, and Z. Ren, "UHF micromechanical compound-(2,4) mode ring resonators with solid-gap transducers," *Frequency Control Symposium, 2007 Joint with the 21st European Frequency and Time Forum. IEEE International*, pp. 1370–1375, 29 2007-June 1 2007.

[91] J. E.-Y. Lee, Y. Zhu, and A. A. Seshia, "A bulk acoustic mode single-crystal silicon microresonator with a high-quality factor," *Journal of Micromechanics and Microengineering*, vol. 18, no. 6, p. 064001 (6pp), 2008.

[92] L. Khine and M. Palaniapan, "High-Q bulk-mode SOI square resonators with straight-beam anchors," *Journal of Micromechanics and Microengineering*, vol. 19, no. 1, p. 015017 (10pp), 2009.

[93] M. A. Abdelmoneum, M. U. Demirci, and C. T.-C. Nguyen, "Stemless wine-glass-mode disk micromechanical resonators," *Micro Electro Mechanical Systems, 2003. MEMS-03 Kyoto. IEEE The Sixteenth Annual International Conference on*, no. 7743374, pp. 698 – 701, 2003.

[94] C.-C. Nguyen, "Vibrating RF-MEMS technology: Fuel for an integrated micromechanical circuit revolution?," *Solid-State Sensors, Actuators and Microsystems, 2005. Digest of Technical Papers. Transducers '97 '05. The 13th International Conference on*, vol. 1, pp. 243–246 Vol. 1, June 2005.

[95] P. Gammel, G. Fischer, and J. Bouchaud, "RF-MEMS and NEMS technology, devices, and applications," *Bell Labs Technical Journal*, vol. 10, no. 3, pp. 29–59, 2005.

[96] C. T.-C. Nguyen, "MEMS technology for timing and frequency control," *Ultrasonics, Ferroelectrics and Frequency Control, IEEE Transactions on*, vol. 54, pp. 251–270, February 2007.

[97] G. Rebeiz, K. Entesari, I. Reines, S.-J. Park, M. El-Tanani, A. Grichener, and A. Brown, "Tuning in to RF MEMS," *Microwave Magazine, IEEE*, vol. 10, pp. 55–72, Oct. 2009.

[98] S.-S. Li, Y.-W. Lin, Z. Ren, and C.-C. Nguyen, "A micromechanical parallel-class disk-array filter," *Frequency Control Symposium, 2007 Joint with the 21st European Frequency and Time Forum. IEEE International*, pp. 1356–1361, 29 2007-June 1 2007.

[99] A. Nikoozadeh, I. Wygant, D.-S. Lin, O. Oralkan, A. Ergun, D. Stephens, K. Thomenius, A. Dentinger, D. Wildes, G. Akopyan, K. Shivkumar, A. Mahajan, D. Sahn, and B. Khuri-Yakub, "Forward-looking intracardiac ultrasound imaging using a 1-D CMUT array integrated with custom front-end electronics," *Ultrasonics, Ferroelectrics and Frequency Control, IEEE Transactions on*, vol. 55, pp. 2651–2660, December 2008.

[100] J. Wang, J. Butler, T. Feygelson, and C.-C. Nguyen, "1.51-GHz nanocrystalline diamond micromechanical disk resonator with material-mismatched isolating support," *Micro Electro Mechanical Systems, 2004. 17th IEEE International Conference on. (MEMS)*, pp. 641–644, 2004.

[101] H. Guckel, D. W. Burns, H. A. C. Tilmans, D. W. DeRoo, and C. R. Rutigliano, "Mechanical properties of fine grained polysilicon-the repeatability issue," *IEEE Solid-State Sensor and Actuator Workshop, 1988. Technical Digest*, no. 3278355, pp. 96 – 99, 1988.

[102] M. Onoe, "Contour vibrations of isotropic circular plates," *The Journal of the Acoustical Society of America*, vol. 28, no. 6, pp. 1158–1162, 1956.

[103] A. Hernández, C. Pinto, E. Amezua, and H. Fernandes, "Analysis of the components of discretization error in non-linear structural problems," *Finite Elements in Analysis and Design*, vol. 39, no. 9, pp. 835 – 864, 2003.

[104] "Ultrasil website." `http://www.ultrasil.com` Accessed February 15 2010, Feb. 2010.

[105] S. Seok, B. Lee, J. Kim, H. Kim, and K. Chun, "A new compensation method for the footing effect in MEMS fabrication," *Journal of Micromechanics and Microengineering*, 2005.

[106] "Cool Grease (CGR7016)." `http://www.aitechnology.com/`. Accessed February 2010, Feb. 2010.

[107] B. H. Houston, D. M. Photiadis, M. H. Marcus, J. A. Bucaro, X. Liu, and J. F. Vignola, "Thermoelastic loss in microscale oscillators," *Applied Physics Letters*, vol. 80, no. 7, pp. 1300–1302, 2002.

[108] R. Candler, A. Duwel, M. Varghese, S. Chandorkar, M. Hopcroft, W.-T. Park, B. Kim, G. Yama, A. Partridge, M. Lutz, and T. Kenny, "Impact of geometry on thermoelastic dissipation in micromechanical resonant beams," *Journal of Microelectromechanical Systems*, no. 15, 2006.

[109] A. Duwel, R. N. Candler, T. W. Kenny, and M. Varghese, "Engineering MEMS resonators with low thermoelastic damping," *Jornal of Microelectromechanical Systems*, vol. 15, no. 6, pp. 1437 – 1445, 2006.

[110] Y.-H. Cho, B. Kwak, A. Pisano, and R. Howe, "Viscous energy dissipation in laterally oscillating planar microstructures: A theoretical and experimental study," *Micro Electro Mechanical Systems, 1993, MEMS '93, Proceedings An Investigation of Micro Structures, Sensors, Actuators, Machines and Systems. IEEE.*, pp. 93–98, Feb 1993.

[111] W. Ye, X. Wang, W. Hemmert, D. Freeman, and J. White, "Air damping in laterally oscillating microresonators: A numerical and experimental study," *Journal of Microelectromechanical Systems*, vol. 12, no. 5, pp. 557 – 566, 2003.

[112] M. Bao and H. Yang, "Squeeze film air damping in MEMS," *Sensors and Actuators A-Physical*, vol. 136, no. 1, pp. 3–27, 2007.

[113] Z. L. Hao, A. Erbil, and F. Ayazi, "An analytical model for support loss in micromachined beam resonators with in-plane flexural vibrations," *Sensors and Actuators A-Physical*, vol. 109, no. 1-2, pp. 156–164, 2003.

[114] Y. Park and K. Park, "High-fidelity modeling of MEMS resonators - part 1: Anchor loss mechanisms through substrate," *Journal of Microelectromechanical Systems*, vol. 13, no. 2, pp. 238 – 247, 2004.

[115] G. F. Miller and H. Pursey, "The field and radiation impedance of mechanical radiators on the free surface of a semi-infinite isotropic solid," *Proceedings of the Royal Society of London. Series A, Mathematical and Physical Sciences*, vol. 223, no. 1155, pp. 521–541, 1954.

[116] G. Qiang, Z. Wanxie, and W. P. Howson, "A precise method for solving wave propagation problems in layered anisotropic media," *Wave Motion*, vol. 40, no. 3, pp. 191 – 207, 2004.

[117] R. Y. S. Pak and B. B. Guzina, "Seismic soil-structure interaction analysis by direct boundary element methods," *International Journal of Solids and Structures*, vol. 36, no. 31-32, pp. 4743 – 4766, 1999.

[118] S. C. Dutta and R. Roy, "A critical review on idealization and modeling for interaction among soil-foundation-structure system," *Computers & Structures*, vol. 80, no. 20-21, pp. 1579 – 1594, 2002.

[119] D. Bindel, E. Quevy, T. Koyama, S. Govindjee, J. Demmel, and R. Howe, "Anchor loss simulation in resonators," *Micro Electro Mechanical Systems, 2005. MEMS 2005. 18th IEEE International Conference on*, 2005.

[120] T. Koyama, D. S. Bindel, E. P. W. H. Quevy, S. Govindjee, J. W. Demmel, and R. T. Howe, "Simulation tools for damping in high frequency resonators," *Sensors, 2005 IEEE*, p. 4, 2005.

[121] D. Paci, S. Stoffels, and H. A. C. Tilmans, "Simulations of the anchor losses in MEM disk resonators," in *Technical Proceedings of the 2006 NSTI nanotechnology conference and Trade Show*, vol. 3, pp. 558 – 561, 2006.

[122] R. D. Mindlin, "Force at a point in the interior of a semi-infinite solid," *Physics*, vol. 7, no. 5, pp. 195–202, 1936.

[123] H. Pursey, "The motional impedance of simple sources in an isotropic solid," *British Journal of Applied Physics*, vol. 4, no. 1, pp. 12–20, 1953.

[124] W. E. Farrell, "Deformation of the Earth by Surface Loads," *Reviews of Geophysics and Space Physics*, vol. 10, pp. 761–797, Aug. 1972.

[125] J. W. Meek and J. P. Wolf, "Why cone models can represent the elastic half-space," *Earthquake Engineering & Structural Dynamics*, vol. 22, no. 9, pp. 759–771, 1993.

[126] J. P. Wolf, "Spring-dashpot-mass models for foundation vibrations," *Earthquake Engineering & Structural Dynamics*, vol. 26, no. 9, pp. 931–949, 1997.

[127] J. P. Wolf and A. J. Deeks, "Cones to model foundation vibrations: incompressible soil and axi-symmetric embedment of arbitrary shape," *Soil Dynamics and Earthquake Engineering*, vol. 24, no. 12, pp. 963 – 978, 2004.

[128] G. F. Miller and H. Pursey, "On the partition of energy between elastic waves in a semi-infinite solid," *Proceedings of the Royal Society of London. Series A, Mathematical and Physical Sciences*, vol. 233, no. 1192, pp. 55–69, 1955.

[129] "Mathematica Computer Algebra System." `http://www.wolfram.com/`. Accessed February 2010, Feb. 2010.

[130] V. Congradac and F. Kulic, "HVAC system optimization with CO_2 concentration control using genetic algorithms," *Energy and Buildings*, vol. 41, no. 5, pp. 571 – 577, 2009.

[131] S. Emmerich and A. Persily], "Literature review on CO_2 based demand controlled ventilation.," in *American Society of Heating, Refrigerating and Air-Conditioning Engineers, Transactions of the*, vol. 103, 1997.

[132] M. Schell and D. Int-Hout, "Demand Control Ventilation Using CO_2," *ASHRAE Journal*, vol. 43, no. 2, pp. 18 – 24, 2001.

[133] J. R. Sand, "Demand-controlled ventilation using CO_2 sensors," tech. rep., U.S. Department of Energy and Renewable Energy, 2006.

[134] K. Schjolberg-Henriksen, D. Wang, H. Rogne, A. Ferber, A. Vogl, S. Moe, R. Bernstein, D. Lapadatu, K. Sandven, and S. Brida, "High-resolution pressure sensor for photo acoustic gas detection," *Sensors and Actuators A: Physical*, vol. 132, pp. 207–213, Nov. 2006.

[135] K. Schjolberg-Henriksen, O. Schulz, A. Ferber, S. Moe, M. Lloyd, G. Muller, K.-H. Suphan, D. Wang, and R. Bernstein, "Sensitive and selective photoacoustic gas sensor suitable for high-volume manufacturing," *Sensors Journal, IEEE*, vol. 8, pp. 1539–1545, Sept. 2008.

[136] A. Rosencwaig and A. Gersho, "Theory of the photoacoustic effect with solids," *Journal of Applied Physics*, vol. 47, no. 1, pp. 64–69, 1976.

[137] A. C. Tam, "Applications of photoacoustic sensing techniques," *Rev. Mod. Phys.*, vol. 58, pp. 381–431, Apr 1986.

[138] P. Ohlckers, A. Ferber, V. Dmitriev, and G. Kirpilenko, "A photoacoustic gas sensing silicon microsystem," in *Transducers '01: Eurosensors XV, Digest of Tehnical Ppapers, VOLS 1 and 2* (E. Obermeier, ed.), pp. 780–783, Springer-Verlag Berlin, 2001.

[139] P. Ohlckers, T. Skotheim, V. Dmitriev, and G. Kirpilenko, "Advantages and limitations of diamond-like carbon as a MEMS thin-film material," *Technical Proceedings of the 2008 NSTI Nanotechnology Conference and Trade Show*, vol. 1, pp. 63–66, 2008.

[140] D. Hohm and G. Hess, "A subminiature condenser microphone with silicon nitride membrane and silicon back plate," *The Journal of the Acoustical Society of America*, vol. 85, no. 1, pp. 476–480, 1989.

[141] J. Bergqvist and J. Gobet, "Capacitive microphone with a surface micromachined backplate using electroplating technology," *Microelectromechanical Systems, Journal of*, vol. 3, pp. 69–75, Jun 1994.

[142] W. Kronast, B. Müller, W. Siedel, and A. Stoffel, "Single-chip condenser microphone using porous silicon as sacrificial layer for the air gap," *Sensors and Actuators A: Physical*, vol. 87, no. 3, pp. 188 – 193, 2001.

[143] X. Li, R. Lin, H. Kek, J. Miao, and Q. Zou, "Sensitivity-improved silicon condenser microphone with a novel single deeply corrugated diaphragm," *Sensors and Actuators A: Physical*, vol. 92, no. 1-3, pp. 257 – 262, 2001.

[144] S. C. Thompson, J. L. LoPresti, E. M. Ring, H. G. Nepomuceno, J. J. Beard, W. J. Ballad, and E. V. Carlson, "Noise in miniature microphones," *The Journal of the Acoustical Society of America*, vol. 111, no. 2, pp. 861–866, 2002.

[145] S. S. Lee, R. Ried, and R. White, "Piezoelectric cantilever microphone and microspeaker," *Microelectromechanical Systems, Journal of*, vol. 5, pp. 238–242, Dec 1996.

[146] S. C. Ko, Y. C. Kim, S. S. Lee, S. H. Choi, and S. R. Kim, "Micromachined piezoelectric membrane acoustic device," *Sensors and Actuators A: Physical*, vol. 103, no. 1-2, pp. 130 – 134, 2003.

[147] S. Horowitz, T. Nishida, L. Cattafesta, and M. Sheplak, "Development of a micromachined piezoelectric microphone for aeroacoustics applications," *The Journal of the Acoustical Society of America*, vol. 122, no. 6, pp. 3428–3436, 2007.

[148] A. Arora, A. Arora, V. Dwivedi, P. George, K. Sreenivas, and V. Gupta, "Zinc oxide thin film-based MEMS acoustic sensor with tunnel for pressure compensation," *Sensors and Actuators A: Physical*, vol. 141, no. 2, pp. 256 – 261, 2008.

[149] W. S. Lee and S. S. Lee, "Piezoelectric microphone built on circular diaphragm," *Sensors and Actuators A: Physical*, vol. 144, no. 2, pp. 367 – 373, 2008.

[150] J. Xu, M. Dapino, D. Gallego-Perez, and D. Hansford, "Microphone based on polyvinylidene fluoride (PVDF) micro-pillars and patterned electrodes," *Sensors and Actuators A: Physical*, vol. 153, no. 1, pp. 24 – 32, 2009.

[151] D. van den Ende, B. Bos, W. Groen, and L. Dortmans, "Lifetime of piezoceramic multilayer actuators: Interplay of material properties and actuator design," *Journal of Electroceramics*, vol. 22, pp. 163–170, Feb. 2009.

[152] I. Lipscomb, P. Weaver, J. Swingler, and J. McBride, "The effect of relative humidity, temperature and electrical field on leakage currents in piezo-ceramic actuators under dc bias," *Sensors and Actuators A: Physical*, vol. 151, no. 2, pp. 179 – 186, 2009.

[153] P. Sievila, V.-P. Rytkonen, O. Hahtela, N. Chekurov, J. Kauppinen, and I. Tittonen, "Fabrication and characterization of an ultrasensitive acousto-optical cantilever," *Journal of Micromechanics and Microengineering*, vol. 17, no. 5, pp. 852–859, 2007.

[154] S. Firebaugh, K. Jensen, and M. Schmidt, "Miniaturization and integration of photoacoustic detection with a microfabricated chemical reactor system," *Microelectromechanical Systems, Journal of*, vol. 10, pp. 232–237, Jun 2001.

[155] R. Schellin and G. Hess, "A silicon subminiature microphone based on piezoresistive polysilicon strain gauges," *Sensors and Actuators A: Physical*, vol. 32, no. 1-3, pp. 555 – 559, 1992.

[156] P. Melvaas, E. Kälvesten, P. Enoksson, and G. Stemme, "A free-hanging strain-gauge for ultraminiaturized pressure sensors," *Sensors and Actuators A: Physical*, vol. 97-98, pp. 75 – 82, 2002.

[157] C. Pramanik, H. Saha, and U. Gangopadhyay, "Design optimization of a high performance silicon MEMS piezoresistive pressure sensor for biomedical applications," *Journal of Micromechanics and Microengineering*, vol. 16, no. 10, pp. 2060–2066, 2006.

[158] M. Goto, Y. Iguchi, K. Ono, A. Ando, F. Takeshi, S. Matsunaga, Y. Yasuno, K. Tanioka, and T. Tajima, "High-performance condenser microphone with single-crystalline silicon diaphragm and backplate," *IEEE Sensors Journal*, vol. 7, no. 1, pp. 4–10, 2007.

[159] A. Dehé, "Silicon microphone development and application," *Sensors and Actuators A: Physical*, vol. 133, pp. 283–287, Feb. 2007.

[160] B. A. Ganji and B. Y. Majlis, "Design and fabrication of a new MEMS capacitive microphone using a perforated aluminum diaphragm," *Sensors and Actuators A: Physical*, vol. 149, no. 1, pp. 29 – 37, 2009.

[161] Q. Zou, Z. Li, and L. Liu, "Design and fabrication of silicon condenser microphone using corrugated diaphragm technique," *Microelectromechanical Systems, Journal of*, vol. 5, pp. 197–204, Sep 1996.

[162] M. Füldner, A. Dehé, and R. Lerch, "Analytical analysis and finite element simulation of advanced membranes for silicon microphones," *Sensors Journal, IEEE*, vol. 5, no. 5, pp. 857–863, 2005.

[163] C.-H. Chen, H.-C. Kan, P.-H. Yang, and W. Yeng-Tseng, "Modeling of corrugated diaphragms for condenser microphones," in *Proc. International Microsystems, Packaging, Assembly and Circuits Technology IMPACT 2007*, pp. 161–164, 2007.

[164] J. Chen, L. Liu, Z. Li, Z. Tan, Y. Xu, and J. Ma, "On the single-chip condenser miniature microphone using DRIE and backside etching techniques," *Sensors and Actuators A: Physical*, vol. 103, no. 1-2, pp. 42 – 47, 2003.

[165] R. Kressmann, M. Klaiber, and G. Hess, "Silicon condenser microphones with corrugated silicon oxide/nitride electret membranes," *Sensors and Actuators A: Physical*, vol. 100, no. 2-3, pp. 301 – 309, 2002.

[166] H. Bruus, *Theoretical Microfluidics*. No. 06 in Oxford Master Series in Physics, Oxford University Press, 2007.

[167] J. Miao, R. Lin, L. Chen, Q. Zou, S. Y. Lim, and S. H. Seah, "Design considerations in micromachined silicon microphones," *Microelectronics Journal*, vol. 33, no. 1-2, pp. 21 – 28, 2002.

[168] G.-D. J. Su, S. H. Hung, D. Jia, and F. Jiang, "Serpentine spring corner designs for micro-electro-mechanical systems optical switches with large mirror mass," *Optical Review*, vol. 12, pp. 339–344, July 2005.

[169] G. Barillaro, A. Molfese, A. Nannini, and F. Pieri, "Analysis, simulation and relative performances of two kinds of serpentine springs," *Journal of Micromechanics and Microengineering*, vol. 15, no. 4, pp. 736–746, 2005.

[170] D. Lapadatu, "SensoNor MultiMEMS foundry service, Design Handbook 4.2." Available upon request to Sensonor Technologies, March 2009.

[171] C. Lowrie, M. P. Y. Desmulliez, L. Hoff, O. J. Elle, and E. Fosse, "Fabrication of a MEMS accelerometer to detect heart bypass surgery complications," *Sensor Review*, vol. 29, no. 4, pp. 319 – 325, 2009.

[172] MEMSCAP, "MEMSCAP SP82 datasheet." `http://www.memscap.com/dowload/standards/SP_82_Pressure_Sensors_fr6.pdf`, Nov. 2009.

[173] D. Jarvis, "Sound measurements," *Metrologia*, vol. 36, no. 4, pp. 249–255, 1999.

Appendix A

Notation used for crystal vectors and planes

Notation	Description
[ ]	A specific direction (e.g. $[1, 0, -1]$).
⟨ ⟩	A family of equivalent directions (e.g. $\langle 110 \rangle$).
( )	A specific plane (e.g. (113)).
{ }	A family of equivalent planes (e.g. $\{311\}$).

Appendix B

Parameter tables

Table B.1: Disk thicknesses in μm as used for FEA simulations in chapter 2.

	Aspect ratio[-]					
Disk radius [μm]	6	7	8	9	10	11
16	2.67	2.29	2.00	1.78	1.60	1.45
18	3.00	2.57	2.25	2.00	1.80	1.64
20	3.33	2.86	2.50	2.22	2.00	1.82
22	3.67	3.14	2.75	2.44	2.20	2.00
24	4.00	3.43	3.00	2.67	2.40	2.18
26	4.33	3.71	3.25	2.89	2.60	2.36
28	4.67	4.00	3.50	3.11	2.80	2.55

Table B.2: Stem radii as used in FEA simulations in chapter 2. All dimensions in μm

0.02	0.12	0.22	0.32	0.42	0.52	0.62	0.72	0.81	0.91
1.01	1.11	1.21	1.31	1.41	1.51	1.6	1.7	1.8	1.9
2									

Table B.3: κ values used for various disk diameters.

Disk radius [μm]	16	18	20	22	24	26	28
κ	1.99653	1.99683	1.99702	1.99715	1.99725	1.99732	1.99737